Obtaining the spacetime metric from cosmological observations

Hui-Ching Lu

A thesis

presented to the University of Cape Town

for the degree of

Master of Science

in

Applied Mathematics

Supervised by

Charles W. Hellaby

August 3, 2006

Abstract

The Copernican principle asserts homogeneity on very large scales, however, this scale is still not well defined; and in reality homogeneity is assumed. Recent galaxy redshift surveys have brought in a large amount of cosmological data out to redshift 0.3 or more, that is now available for analysis; and their accuracy has been improved dramatically. With future surveys expected to achieve a high degree of completeness out to redshift exceeding 1, and a dramatic increase in the amount of data harvested, it will soon be practical to have a numerical programme for determining the metric of the universe from standard observations. This project is the beginning of a series of developments on such a numerical implementation. It is sensible to start with a simple case – that of spherical symmetry and a dust equation of state. Using observational data from our past light cone, consisting of galaxy redshifts, apparent luminosities, angular diameters and number densities, together with chosen source evolution functions, viz absolute luminosities, true diameters and masses of sources; and applying the algorithm in [43], a set of Lemaître-Tolman-Bondi (LTB) arbitrary functions can be found. This set will specify the LTB model that reproduces the given observations, and hence provides a metric that describes the geometry of the observed universe.

We briefly review the theoretical development of this topic from the fundamental paper by Kristian and Sachs, to the ideal observational cosmology programme by Ellis and Stoeger and others. We also discuss some of the most crucial issues that we are currently facing in the study of observational cosmology, for example, the problem of source evolution and selection effects. We then briefly introduce a few recent galaxy redshift surveys that are available for analysis, or will be available in the near future, and the data that we may use from them. We also discuss how one can obtain the diameter distance, luminosity distance and number density, the observables that are essential to our project. We introduce the LTB metric, the null cone solution and the notation that we use, and thus relate the LTB model to the observables.

The numerical procedure of the actual implementation is described. In order to be sure that our numerical method is able to reproduce the correct metric information from the given observations, we tested it with a few artificial data sets generated from the standard Robertson-Walker expressions. We started with a first order integration method – Euler's method, but we were later convinced that a second order method was needed. Once a second order Runge-Kutta method was used, it reduced the maximum percentage error by at least 20%. After obtaining results from the homogeneous models, we then tested our code with artificial data generated from a few inhomogeneous models – a model with a varying bang time, a model with a varying mass, a model with a varying geometry/energy and a model with strong inhomogeneity. With their percentage error smaller than 0.5% for all but one variable in one case, which had error smaller than 3%, we are quite satisfied with the accuracy obtained from our numerical output. Of course, test runs with the real observational data are still required in order to refine the ability of our computer programme

to produce the correct metric information from observational data, but we leave this for the future development, as there are many refinements needed before such results could be taken seriously.

Acknowledgements

I would like to thank my supervisor Charles Hellaby. It would not be possible for me to complete the work without his patience and guidance. I would like to thank my parents as well. Without their support and understanding, it is not possible for me to do the Master's degree in the area that I've chosen....

Of course supports (and entertainments) from the rest of the cosmology group is acknowledged here. Some thanks should go to some of my friends mentioned (and the not mentioned ones) here for their efforts of entertaining me sometimes – Diane, Ronnie, Bonita and many many many many more.... Special thanks are given to my ex-officemate Oliver Oxtoby; without his help, it's not possible for me to achieve the results I have for a 'very numerical' project. Still, some thanks should go to my current officemate, William Robinson, it would be a very empty office if it was not for his presence from time to time. I suppose some thanks should go to my coffeemate and entertainer, Jannie Leach; without him (and his talkative self), coffee would be just something to keep me awake. Oh! Yes. There is one more person I should thank as well although he does not know that he is helping me from a very different way. I would like to thank Martin Bojowald, for not yet tired of reading all my emails talking about not work related stuff. However, I think I do talk a bit too much in the emails.

I would like to thank University of Cape Town and the National Research Foundation for their financial support.

Contents

List of Abbreviations

FLRW	Friedmann-Lemaître-Robertson-Walker
CMBR	Cosmic Background Radiation
EGS	Ehler-Geren-Sachs
SME	Stoeger-Maartens-Ellis
LTB	Lemaître-Tolman-Bondi
EFEs	Einstein field equations
RW	Robertson-Walker
MHE	Mustapha-Hellaby-Ellis paper [43]
2dF	2 Degree Field
SDSS	Sloan Digital Sky Survey
6dF	6 Degree Field
QSO(s)	Quasi-Stellar Object(s)
DE(s)	Differential Equation(s)

List of Tables

List of Figures

Chapter 1

Introduction

In modern cosmology, many attempts have been made at determining the large-scale structure of the physical universe with constraints provided by cosmological observations and knowledge derived from local physical experiments. However, the most common approach is to work with models that adopt the postulate that the universe is spatially homogeneous on large scales. This universe is best represented by a Friedmann-Lemaître-Robertson-Walker (FLRW) model, hence, using observational data to determine the few free parameters characteristic of such universe models has become the primary objective, and this overall framework has been presented in great detail in many books and papers (see for example [49], [50] and [34]).

Spatial homogeneity is the direct result of the "Cosmological Principle" (see [6] and [59]) or the "Copernican Principle", which is the assumption that we are not privileged observers. If we adopt the Copernican Principle, then it turns out that a single observational quantity - the cosmic background radiation (CMBR) - is potentially sufficient to determine the spacetime geometry. [1] However, there are certain advantages and defects in adopting either one of the two assumptions. Although the Copernican Principle only determines a model which states conditions in the 'observable' parts of the universe, nonetheless, its validity in describing this region of the universe can be proven fully with observations. Even though the Cosmological Principle is able to determine a 'complete' universe model, however, the consequence in adopting it is immense since we cannot verify it fully due to the predictions it makes about parts of the universe that are beyond our observation as pointed out in [17]. With one physical universe that is available for observation, the former seems to be a more reasonable choice. Hence, being able to *prove* the homogeneity of the observable region of the universe rather than assuming it in principle is a long term objective of the current project.

We wish to determine the spacetime geometry as far as possible from astronomical observations with minimal a priori assumptions. The idea of reducing observed cosmological data to a metric was first explicitly discussed by Kristian and Sachs [37]; they examined how this could be done near our present spacetime position by deriving expressions in power series for some astronomical observations near the observer in a general metric, and

[1] The Ehler-Geren-Sachs (EGS) theorem [15] states that, if a family of observers in a spacetime observe the cosmic background radiation to be isotropic, then the spacetime is FLRW. However, the EGS theorem applies to exact isotropy of CMBR, which then implies exact FLRW geometry, given the Copernican principle. With small anisotropies detected in CMBR, one needs an 'almost EGS theorem', which is the Stoeger-Maartens-Ellis (SME) theorem [52], to imply an 'almost FLRW' geometry [40]. Some arguments for radial homogeneity based on the CMBR were considered in [23].

demonstrated the limitations they faced in confirming homogeneity of the universe from observations. However, the problem of the source evolution was barely addressed in their derivations.

In the ideal observational cosmology program by Ellis and Stoeger and others [18, 53, 54, 55, 56, 41, 42, 3, 4, 5] , they took a slightly different approach to Kristian and Sachs as they aimed to determine what could and could not be decidable in cosmology on the basis of ideal astronomical observations, and so considered the limits of verification in cosmology. They worked with observational coordinates since all observational data are given, not on the usual spacelike surface of constant time, but rather on our past null cone, which is centred at our observational position on our worldline. Hence, the observational data can be used with ease in the implementation of any algorithm developed through using the Einstein field equations (EFEs) that are written in observational coordinates. In this programme, they first showed that if we take a cosmographic view of data, which is analysis of the observational data without the use of the EFEs, we cannot determine all the major features of the spacetime structure on our past light cone fully from observations alone. Even with the assumption that our spacetime is spherically symmetric, together with isotropic observations, we are still unable to prove that the universe is homogeneous.

They then turned to cosmology, and developed a framework which examined how assuming and using the EFEs as the dynamical theory for the large scale development of spacetime enables ideal observations to determine the spacetime geometry both on and off our past null cone. In this context, they solved the exact spherically symmetric problem using the fluid-ray tetrad formulation of the EFEs and gave a scheme for constructing solutions directly from the observational data. They also dealt with the spherically symmetric perturbation problem and established a specific practical criterion for the validity of the perturbation treatment for 'almost-FLRW' observational cosmologies.

They extended this work by solving the first-order general perturbation problem in observational coordinates for the complete astronomical data set on our past light cone without any symmetries assumed. Furthermore, they provided an integration scheme for the exact spherically symmetric EFEs in observational coordinates, using cosmological data that are given as functions of redshift, for example observer area distance and galaxy number counts, to find the spacetime metric directly from them. Later on, this framework was successfully extended to the perturbed FLRW spherically symmetric case. Despite what they have achieved in this program, they still encountered a very basic problem: the effect of source evolution (the evolution of galaxies both in number and luminosity in this case). Although they acknowledged this problem, they assumed that the source evolution is known. In order to implement any approach in this program, one will require a model of how the population and luminosities of the different types of galaxies evolve with redshift.

The study of galaxy evolution is now a very active field and it covers a wide variety of topics, for example, the rate of formation of stars of different masses in each galaxy type, the rate of galaxy mergers, the effect of galaxy mergers and encounters on star formation, how central bulges and bars form, how the masses, luminosities, morphology and star formation rates of galaxies are affected by the environment where they reside, etc. For some papers on the study of galaxy evolution see [22, 30, 2, 10] and the references therein. These issues are very difficult to address, so usually one makes the assumption that the universe is described by the standard FLRW geometry and presents the observational results in terms of this class of models, as pointed out in [23]. In the ideal observational cosmology program, we require knowledge of the source evolution in order to implement any approach. The current study of source evolution depends on knowing that the cosmological model is homogeneous.

We are unable to determine the homogeneity of the universe from standard observations without knowing the source evolution. Therefore, other approaches or contributions are needed in order to solve this predicament that we are facing at the moment in the field of relativistic cosmology.

A new general proposal that might help us in reconciling this situation was outlined in [47]; and it is for testing non-standard cosmological models (non-FLRW models) by means of observational relations for cosmological point sources in some specific waveband, but for any cosmological metric. Galaxy redshift surveys can provide the data which would be used in this context. This way, one can determine how good the standard models are by comparing the differences in the fitting of exact FLRW, almost-FLRW and non-FLRW models. The first of a series of papers following this outline was published in 2003 [48]. In this paper, they aimed at connecting the theory of relativistic cosmology number counts with the astronomical data, in practice, and also the theory behind the galaxy luminosity function. As an example to demonstrate how this approach can be used in practice, they checked the consistency for the luminosity function parameters determined from the original data from Canadian Network for Observational Cosmology field galaxy survey 2 (CNOC2) [2] [60] with the Einstein-de Sitter model, which they assumed, for intermediate redshift, and found the general consistency, but with some deviation at higher redshift.

It is also worth pointing out another very important issue in the study of source evolution specifically, which is how one can distinguish between the effects of the source evolution, cosmic inhomogeneity, and cosmic evolution. It was shown in Mustapha et al. [43] [3] that, using standard cosmological observations, i.e. luminosity versus redshift, area distance versus redshift and number count versus redshift, one cannot separate the effects of the above mentioned three things. However, a method of testing and separating the three effects using the multicolour large scale observations was proposed in [26]. In that paper, they showed that if one compares the luminosity versus redshift in more than one colour and more than one source type, constraints can be placed on source evolution theories even if we have unknown inhomogeneity. And this can potentially provide us with a test that is complementary to the current methods.

One needs to consider issues that are crucial to real observations as well; one of these, for instance, is the selection effects. With any real observation, there is a certain limitation on the ability of the equipment used. As the observation approaches this limit, the quality and accuracy of the observed data will degenerate considerably since the apparent surface brightness and size of an image in any survey are the essential components for identifying an object. This means that as the observations probe deeper into space, only the brighter objects will be seen; the dimmer ones will not be detected, and hence, source counts become more and more incomplete with increasing redshift. Therefore, it is difficult to determine the correct redshift space density, which affects any results obtained in the cosmological study using these data. What has been done in general regarding to this problem is to set a cut off point for observation, for example, for the 2 degree field observation it is at a blue magnitude limit $b_J = 19.5$. In selecting this limit, one needs to make sure that all the measurements within the cut off have a satisfactory level of accuracy and quality. This problem has been addressed by many due to its importance in relating the real observational problems to the theoretical studies in cosmology, see for example [19, 58].

The issue of image merging and hiding is also of great concern when it comes to real

[2] A 1.5 square degree survey of approximately 6200 field galaxies with $0.1 < z < 0.7$. For papers on the data analysis of this survey, see for example [51, 9].

[3] From here on, we will refer to this paper as MHE.

observation. Even if the observed objects are well within the limit of the equipment used, when two of the observed objects are too close to each other on the sky, it is possible that the two images may merge as one. Or when there is one galaxy that is much brighter than the nearby galaxies, it becomes difficult to separate the images of the dimmer galaxies from the brighter one, and tell exactly how many objects we observe, since images of the galaxies that are less luminous will definitely be "overshadowed" by the brighter ones. This particularly affects the completeness in the number counts we obtain from observation. Therefore, the determination of the galaxy number counts will depend on using the luminosity function to give an estimation on how many galaxies are not observed, when one needs to use the data in any cosmological study. But still, there would be difficulties if there were unseen matter not correlated with visible matter. However, luminous matter is believed to trace dark matter quite well, for example, one can trace the dark matter in galaxy haloes by comparing the flat rotation curve obtained from the spiral galaxy with the contribution from the luminous matter.

The luminosity function gives the number of galaxies per unit luminosity interval per unit volume. It is one of the fundamental quantities in observational cosmology, and it gives a statistical estimation of the galaxy population. Issues like how it varies for different types of galaxy, its dependence on the environment, and so on have been studied by many. Therefore, it gives some indication of the evolution of galaxies also. While each of these issues mentioned above is very important, at this initial stage our focus is on developing a basic numerical procedure, and the incorporation of these effects in our data handling is a matter for the future.

Deducing the geometry of the universe from standard observations has only recently become a more realistic idea since we are now getting very extensive cosmological data sets from galaxy redshift surveys, for example, 6dF and Sloan; and the accuracy of the data has been improved dramatically. We should soon be able to determine the metric of the observed universe from standard observations and quantify homogeneity, and thus check the Copernican assumption with these data numerically. Up to now, the work has been entirely theoretical, and the proposed methods have never been implemented. The questions of choosing appropriate numerical methods and connecting the numerics with real observational data have not been addressed. Hence, this is indeed a long term project and what we focus on in this thesis is just the tip of the iceberg.

The main focus of the work for my Masters is to implement an algorithm from MHE. This work proved the theorem that given any (reasonable) observations, for example, the redshift number density, diameter distance and luminosity distance of sources, and any (reasonable) source evolution functions, for example, the mass, absolute luminosity, and true diameter of sources; a Lemaître-Tolman-Bondi (LTB) model that fits them can be found. What's more, they gave detailed differential equations (DEs), with the conditions for existence of their solutions, and also an algorithm on how one can solve each integration step numerically. Following this algorithm, a set of LTB functions can be found to specify the LTB model that reproduces the given observations and evolution functions. We acknowledge the fact that the LTB model assumes spherically symmetry (see chapter 3 for details of the LTB model) which means that there is a preferred worldline, however this is justifiable for the purpose of this thesis. First of all, since we are trying to prove or disprove the homogeneity of the universe, we need to work with a model which allows for inhomogeneity and has a homogeneous and isotropic limit. In fact, the LTB model is the simplest inhomogeneous model one can get, therefore, using the LTB model is our first step towards a more 'general' inhomogeneous model. Second of all, all the observational data we can use are on the

observer's null cone (our null cone to be exact). This means that, there is a preferred worldline (our worldline), with us being in the centre of our observations. Hence, it is also easier to verify the isotropy around us, whereas radial homogeneity is very hard to demonstrate unambiguously.

Chapter 2

Observables and galaxy redshift surveys

In this chapter, we first introduce a few recent galaxy redshift surveys. Some of them have completed their observation recently, and others will be completed in the near future. Then we give a brief introduction on the observable quantities and the evolution functions that are essential for the long-term aim of this project. Although this gives context to the present work, survey data is not yet extensive enough to give much reliable metric information, and the numerics must still be developed further.

2.1 Recent galaxy redshift surveys

We give brief summaries to three recent galaxy redshift surveys that are currently or in the near future will be available to us. Of course, there are more galaxy surveys available, for example, The European Southern Observatory Very Large Telescope (ESO-VLT) Visible Imaging Multi-Object Spectrograph (VIRMOS) project [62], Deep Extragalactic Evolutionary Probe phase 2 (DEEP2) [61], etc. However, we are unable to go through each and every single one of them here, but this does not mean that they are less important to us than those listed below.

2.1.1 2 Degree Field (2dF)

The 2 Degree Field galaxy redshift survey [63] began in 1997 and was completed in 2002, and was a joint UK-Australian survey of redshifts. It used the Anglo-Australian Telescope's 2-degree Field facility, which could observe 400 objects simultaneously using the multiple-fibre spectrograph over a 2-degree diameter field of view. The source catalogue used was a revised and extended version of the APM (Automatic Plate Measuring) galaxy catalogue created from the photographic plates of the UK Schmidt Telescope Southern Sky Survey. It carried out a large redshift survey of 221,000 galaxies down to an extinction corrected magnitude limit of $b_J < 19.5$ and reached out to a redshift $z \approx 0.3$ that made a 3D map of the Southern Sky. For more detailed reviews of the data analysis see [46, 11].

The 2dF quasi-stellar object (QSO) redshift survey based on the colour-selected objects with $18.25 < b_J < 20.85$ selected from APM scans of UK Schmidt Telescope photographic plates also completed in 2002, and measured 23338 QSO redshifts.

2.1.2 Sloan digital sky survey (SDSS)

The Sloan Digital Sky Survey (SDSS) [64], is a joint US-Japan-Germany project, which will systematically map one-quarter of the entire sky with a large cap in the Northern sky and 3 slices into the South. It produces a detailed image of the observed sky, and determines the positions and absolute brightnesses of more than 100 million celestial objects. When completed, it will provide detailed optical images, and a 3-dimensional map of about a million galaxies and quasars. The 2.5-meter telescope used has a pair of spectrographs fed by optical fibers that can measure spectra of more than 600 galaxies and quasars in a single observation.

The SDSS began formal operations in 2000 and completed its first phase of operations, SDSS-I, in June, 2005. Over the course of five years, SDSS-I imaged more than 8,000 square degrees of the sky in five bandpasses, detecting nearly 200 million celestial objects, and it measured spectra of more than 675,000 galaxies, 90,000 quasars, and 185,000 stars. More information on their latest data release, data release 4, are described in [1].

2.1.3 6 Degree Field (6dF)

A brief summary of the 6dF [65] galaxy survey is give here. The 6dF is a survey of redshifts and peculiar velocities of galaxies selected primarily in the near infrared from the Two Micron All Sky Survey (2MASS) [66] catalogue reaching out to about $z \sim 0.15$. With both the 2dF and SDSS surveys being optically selected, the galaxies that they targeted are dominated by younger, bluer stars, and so are more indicative of the star formation rate in the galaxies. As for 6dF, their near-infrared selection criterion is more sensitive to the peak of the galaxy spectral energy distributions, which is in general, dominated by the old stars that make up most of the stellar mass in the galaxies. Hence, they provide the best estimate of the stellar mass within the galaxies. For further details on 6dF and its samples, observational techniques and the data releases see also [31, 32].

The associated 6 degree field (6dF) QSO, based on the same input catalogue as 2dF, selected 1564 brighter sources with the limits $16 < b_J < 18.25$ for observation. For a report on both of the 2dF and 6dF QSO surveys see [13].

2.1.4 Data format

All the data that we need are provided from the galaxy redshift surveys. However, in order to illustrate how we can obtain the real data or how we distinguish the ones we need so as to extract them from all the data provided by the surveys; we use the information on the final data release from the 2dF galaxy redshift survey provided in [12] as an example here. Still, we only give a brief outline here since extracting and deducing the real data is not in the scope of this thesis.

There are three main components in the 2dF database:

• A set of FITS (Flexible Image Transport System) files – there is one FITS file for each object in the source catalogue. Each FITS file contains all the information on the object from the source catalogue, spectroscopic observations and subsequent analysis.

• A mSQL (Mini Structured Query Language) database – it contains all the parameters for each object. It allows very specific searching of the database and the retrieval of the specified spectra or images.

• A WWW interface – it provides a variety of modes for querying through using the mSQL database and returning the outcome of such a query.

However, in order to obtain any data from the database using the above mentioned approaches, one needs to understand the keywords used in representing the type of information assigned to them. Table 2.1 gives some of the keywords and their descriptions used in the 2dF database. One can use the keywords to extract any information from the database via mSQL, for example, one can send a query to list the information on name, ra, dec, BJSEL, quality, z for a selected object with the 2dF assigned name='TGS469Z164'.

Table 2.1: Example of the keywords and their descriptions of the best observational data given in the 2dF spectroscopic catalogues. This table is reproduced from [12].

Keyword	Format	Description
serial	I6	Database serial number (=SEQNUM)
spectra	I1	Number of spectra obtained
name	A10	2dFGRS name (=NAME)
UKST	A3	UKST plate (=IFIELD)
ra	A11	R.A. (B1950)
dec	A11	Dec. (B1950)
ra2000	A11	R.A. (J2000)
dec2000	A11	Dec. (J2000)
BJG	F6.3	Final b_j magnitude without extinction correction
BJSEL	F6.3	Final b_j magnitude with extinction correction
BJG_OLD	F6.3	Original b_j magnitude without extinction correction
BJSELOLD	F6.3	Original b_j magnitude with extinction correction
GALEXT	F5.3	Galactic extinction value
SB_BJ	F6.3	SuperCosmos b_j magnitude without extinction correction
SR_R	F6.3	SuperCosmos R magnitude without extinction correction
z	F9.6	Best redshift (observed)
z_helio	F9.6	Best redshift (heliocentric)
obsrun	A5	Observation run of best spectrum
quality	I1	Redshift quality parameter for best spectrum (quality=1-5; reliable redshift have quality >= 3)
abemma	I1	Redshift type (abs=1, emi=2, man=3)
Z_ABS	F9.6	Cross-correlation redshift from best spectrum
KBESTR	I1	Cross-correlation template from best spectrum
R_CRCOR	F5.3	Cross-correlation R value from best spectrum
Z_EMI	F9.6	Emission redshift from best spectrum
NMBEST	I2	Number of emission lines for Z_EMI from best spectrum
SNR	F6.2	Median S/N per pixel from best spectrum
ETA_TYPE	F10.6	Eta spectral type parameter from best spectrum (-99.9 if none)

From Table 2.1, let us look at the data that we may need for the purpose of this project in the future and point out the keywords used to represent them in the database. From the table, all the information above the line for the keyword BJSEL are not needed. However, there are four different keywords representing four different types of magnitudes in the database. Of course, we are not going to work with completely raw data for our project in the future, therefore, we have to put our faith in all the corrections that are made to the data by the observation team. And here, by extinction correction, they mean that the data

are with corrections for isophote, field-effects and plate-matching, then calibrated to total magnitudes with saturation correction, and then the extinction corrected as explained in one of the tables in [12]. The need for extinction correction is obvious since with the observed objects positioned closer to the plane of our galaxy, there is more dust or gas to affect the accuracy of the data, and hence corrections for these effects are necessary. Therefore, keyword BJSEL may represent the magnitudes we can use for the apparent luminosity.

The keyword z_helio represents the best heliocentric corrected redshift and this may be the redshift that we need for our project since with heliocentric correction, it removes the effects of the relative circular motion of the Earth around the Sun. As for the redshift quality (see the line for the keyword quality), we may need to take this into consideration and throw away those ones with quality < 3 (see Table 2.1). Of course, information contained in the keywords abemma, Z_ABS, Z_EMI and ETA_TYPE [1] may also help us in deciding on the quality of the data, and therefore a decision can be made regarding which ones we use for our project and which ones we should leave out. Once we move on to non-spherically-symmetric models, the angular position, ra2000 and dec2000 will be important.

We have looked at some galaxy redshift surveys that may provide us with the data for our project in the future and the format of the data that we may obtain. Let us look at some observable quantities in the next section.

2.2 Basic observable quantities

If we consider galaxies as our sources, then the primary observable quantities are their redshift, z, apparent luminosity, l, angular diameter [2], δ, and their number density, n, in redshift space. The associated source properties, which are expected to evolve with time, are the absolute luminosity, L, true diameter, D, and the average mass, ζ.

Below we introduce how, in theory, one can relate these quantities to the null cone properties of a metric, via the luminosity distance, and the diameter distance. For simplicity, we here assume a single source type, i.e. an "average" galaxy. For a generalisation to many source types see [26].

Redshift space number density

Figure 2.1 is an illustration of the number density in redshift space. For any spherically symmetric model used, functions are expressed in terms of the coordinate radius r. Suppose that the observer performs an observation of an area in the sky that has N galaxies between r and $r + dr$, and each galaxy has average mass ζ. If the proper volume of space on the constant time slice (at time t as shown in the figure) is d^3V, then the density is

$$\rho = \frac{\zeta N}{d^3 V} \ . \tag{2.1}$$

However, what the observer actually observes on his past null cone is not a spatial volume, but a null surface volume, hence we need the redshift interval dz that corresponds to the coordinate interval dr on the observer's past null cone. The number of galaxies observed must be the same, i.e. N galaxies observed between z and $z + dz$. The volume in redshift

[1] This is a 2dF defined parameter, it is based on a "Principle Components Analysis", and designed to be robust to instrumental uncertainties and represents the absorption/emission strength of a galaxy.

[2] In literature, this is sometimes also known as the observer area distance [16] or the corrected luminosity distance [37].

space that corresponds to the proper volume d^3V is denoted as $d^3\nu$. Therefore, the redshift space number density n is

$$n = \frac{N}{d^3\nu} \ . \tag{2.2}$$

If we substitute (2.1) into (2.2) in order to cancel N, we then get

$$n = \frac{\rho d^3V}{\zeta d^3\nu} \ . \tag{2.3}$$

Hence, equation (2.3) gives us a relation between masses of sources ζ, proper density ρ and the redshift space density n, and this will prove to be useful for us later on when we try to relate the observables to the LTB model.

Figure 2.1: Illustration of the number of galaxies counted within an interval dr and its corresponding redshift interval dz on the observer's past null cone.

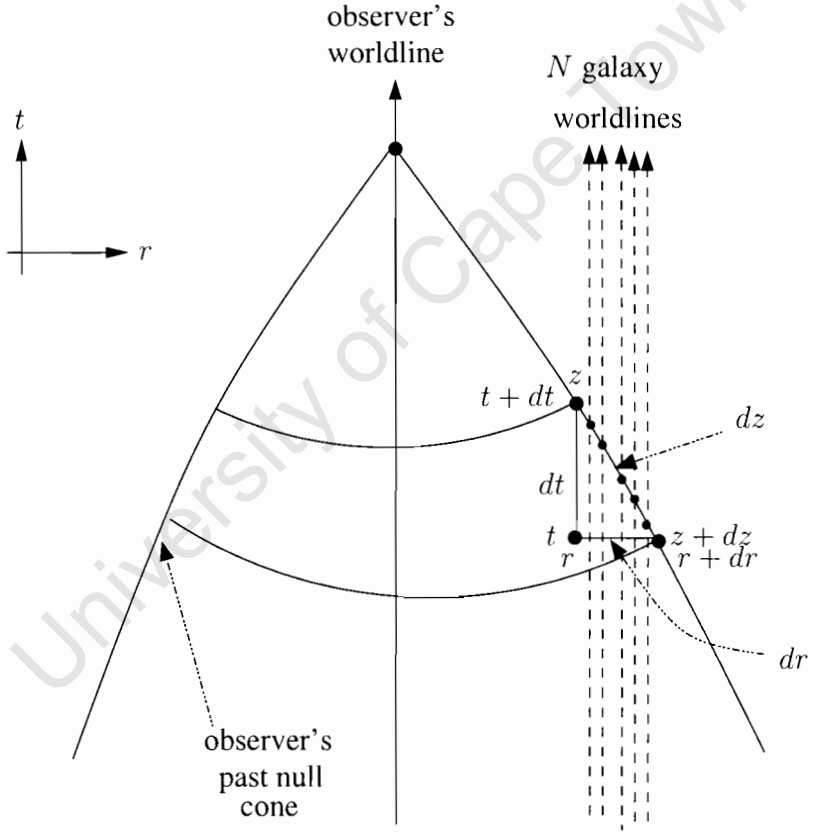

Diameter distance and luminosity distance

Let us consider flat space first, and assume that we know the true diameter of a galaxy is D and its absolute luminosity is L. Then it is possible to get the angular diameter distance d_D from its measured angular diameter δ:

$$d_D = \frac{D}{\delta} \ , \tag{2.4}$$

Figure 2.2: Illustration of the diameter distance between the observer and the galaxy in flat space.

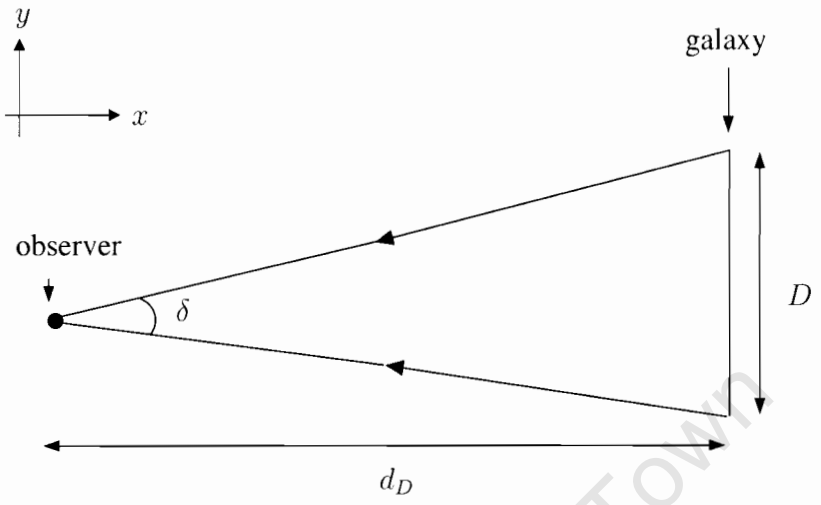

for any $d_D \gg D$. This defines the angular diameter distance d_D. Similarly, if we know the true area A of the galaxy and the solid angle at the observer is φ, we then have

$$d_D^2 = \frac{A}{\varphi} \;\Rightarrow\; \varphi = \frac{A}{d_D^2} \;, \tag{2.5}$$

and this is also recognised as the angular diameter distance or the area distance.

If the galaxy emits light of total power B J/s that is travelling radially outwards, with the observer's telescope area being A_t, at a distance d away, collecting a flux or luminosity of l $J/s/m^2$, then the received power is just lA_t. Hence, we have

$$lA_t = B\frac{A_t}{4\pi d^2} \;\Rightarrow\; l = \frac{B}{4\pi d^2} \;, \tag{2.6}$$

where $A_t/4\pi d^2$ can be thought of as the fraction of the emitted light intercepted by the solid angle ω at the telescope, i.e. $\omega/4\pi$, with $\omega = A_t/d^2$. Similarly, the absolute luminosity is the flux one would have collected if the source were at $d_{al} = 10$ parsecs away from the observer:

$$L = \frac{B}{4\pi d_{al}} \;. \tag{2.7}$$

Hence, the luminosity distance d_L is simply

$$d_L = \sqrt{\frac{L}{l}}\; d_{al} \;, \tag{2.8}$$

for $\omega \ll 4\pi$. In flat space, the luminosity distance d_L and the angular diameter distance d_D (or the area distance) are the same, since there is no relative motion between the observer and the galaxy, which affects the observed frequency of the emitted light rays, the area of the source and arrival rates of the photons. However, this is not the case if we consider curved spacetime.

For the central observer observing any astronomical object on his past null cone, the angular diameter distance and the luminosity distance are *defined* with the same equations

Figure 2.3: Illustration of the luminosity distance between the observer and the galaxy in flat space.

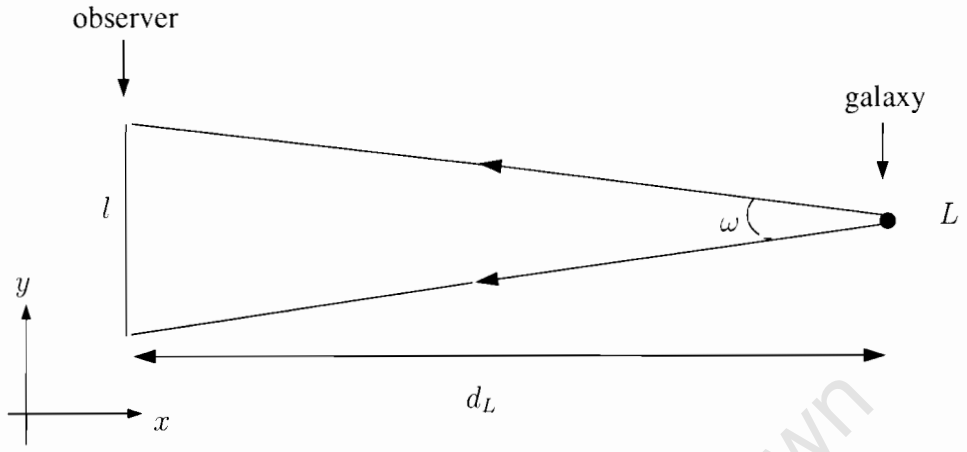

(2.4) and (2.8) as in flat space. Figure 2.4 is the illustration of the diameter distance between the observer and the galaxy on the observer's past null cone. At time t_{em}, if we know the true diameter D of a galaxy, together with the measurement of δ, then the angular diameter distance d_D is determinable from applying equation (2.4). Conversely, it is also possible to determine D from d_D using the same equation. Note that δ is a spatial angle between two directions in space on a constant time slice, hence, it is independent of time, i.e. since the light rays are radial δ does not change with time. Therefore, observing at time t_{ob} if the true diameter D of a galaxy at t_{em} is constant, one can still determine d_D using δ. However, it will become problematic using this approach if D evolves with time, as $D(z)$ must be determined.

Figure 2.5 is the illustration of the luminosity distance between the observer and the galaxy on the galaxy's future null cone. If the galaxy emits photons in all directions (one can think of this as a spherical wavefront) of frequency ν_{em} and hence power B_{em} at time t_{em}, then the frequency of this spherical wavefront gets redshifted when it is observed at the time t_{ob} with power B_{ob}. However, a telescope of area A_t, subtending solid angle ω at the source (at time t_{ob}), can only collect a fraction $\omega/4\pi$ of the power in the wavefront at time t_{ob}. Thus, the apparent luminosity is

$$l = \frac{\omega B_{ob}}{4\pi A_t} \ ,$$

and the absolute luminosity is

$$L = \frac{B_{em}}{4\pi d_{al}^{\ 2}} \ ,$$

We define the luminosity distance in curved spacetime, as in flat space, using equation (2.8). If we simplify the expression and we have

$$d_L = \sqrt{\frac{L}{l}}\ d_{al} = \sqrt{\frac{B_{em}}{B_{ob}}\ \frac{A_t}{\omega}} \ . \tag{2.9}$$

In flat space, we can see that the angular diameter distance and the luminosity distance are equivalent between an observer and the galaxy, since there is no relative motion, and

hence no redshift between the two. In curved spacetime, however, the relation between d_D and d_L is not so simple. The reciprocity theorem

$$d_L = (1+z)^2 \, d_D$$

was first discovered by Etherington in 1933 [21], and proved generally in Ellis [16].

One thing worth pointing out is that this theorem was proved using general null geodesics without any metric being specified, and without assuming the source or observer to be comoving, hence it is valid for any cosmological model. After introducing all the observables that we need for the purpose of this project, we will next introduce the background model – the Lemaître-Tolman-Bondi (LTB) model – in the next chapter.

Figure 2.4: Illustration of the diameter distance between the observer and the galaxy on the observer's past null cone.

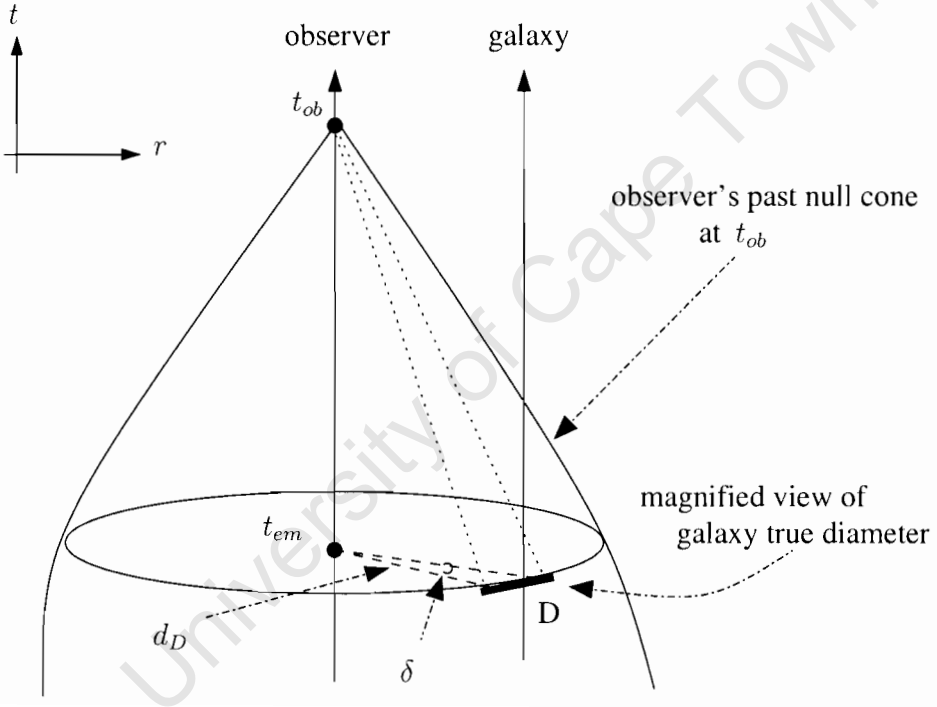

Figure 2.5: Illustration of the luminosity distance between the observer and the galaxy on the galaxy's future null cone.

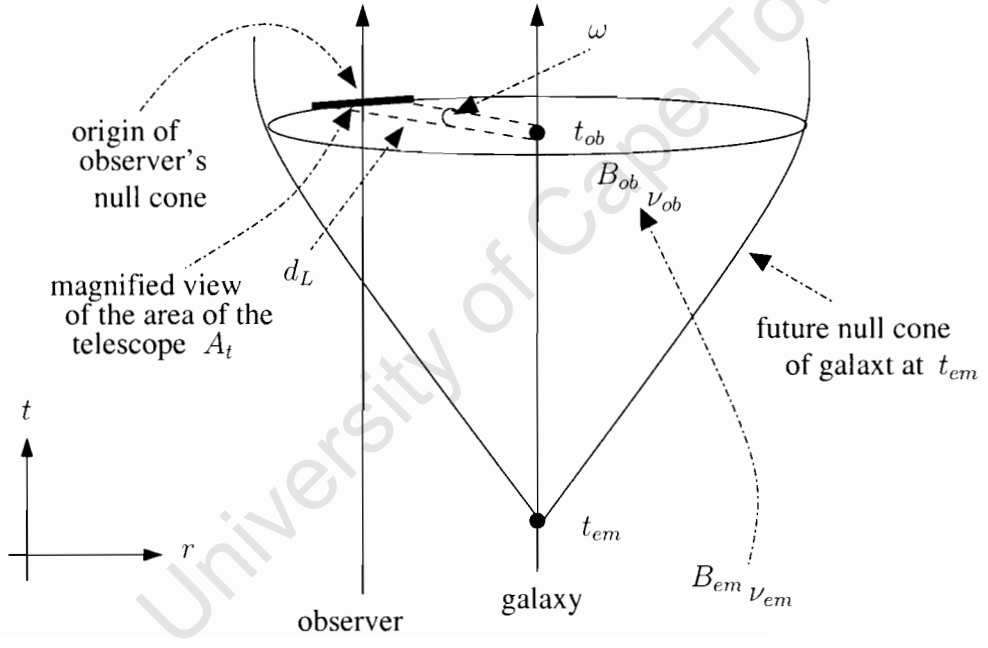

Chapter 3

The Lemaître-Tolman-Bondi Model

The simplest inhomogeneous models are those that are spherically symmetric. The Lemaître-Tolman-Bondi (LTB) model was first found by Lemaître [39], but Datt independently discovered a form of this model in 1938 [14] which is an inhomogeneous generalisation of the Kantowski-Sachs solutions [33]. Tolman mentioned Lemaître's paper in a study of the stability of FLRW models, but solved the field equations himself [57]. The paper by Bondi [7] gives a discussion of geometrical and physical properties of the LTB model. He solved the field equations completely and also gave the components of the Riemann curvature tensor together with the Kretschmann scalar. Since then, this model has been independently rediscovered many times. More details in the development and discoveries of the LTB models can be found in [35]. We here work in geometric units, and since we seek a simple model, we set the cosmological constant Λ to be zero.

3.1 The Lemaître-Tolman-Bondi Model

The general spherically symmetric metric for an irrotational dust matter source in synchronous comoving coordinates is the Lemaître-Tolman-Bondi [39, 57, 7] metric

$$ds^2 = -dt^2 + \frac{[R'(t,r)]^2}{1+2E(r)}\, dr^2 + R^2(t,r)d\Omega^2 \ , \tag{3.1}$$

where $R'(t,r) = \partial R(t,r)/\partial r$, and $d\Omega^2 = d\theta^2 + \sin^2\theta d\phi^2$ is the 2-spheres. The function $R = R(t,r)$ is the areal radius, since the proper area of a sphere of coordinate radius r on a time slice of constant t is $4\pi R^2$. The function $E = E(r) \geq -1/2$ is an arbitrary function of the LTB model, representing the local geometry.

Solving the EFEs gives us a generalised Friedmann equation for $R(t,r)$,

$$\dot{R}^2(t,r) = \frac{2M(r)}{R(t,r)} + 2E(r) \ , \tag{3.2}$$

and an expression for the density

$$4\pi\rho(t,r) = \frac{M^{'}(r)}{R^2(t,r)R^{'}(t,r)} \ , \tag{3.3}$$

where $M(r)$ is another arbitrary function of the LTB model that gives the gravitational mass within comoving radius r. Here $E(r)$ also plays a dynamical role, it determines the local energy per unit mass of the dust particles. Equation (3.2) can be solved in terms of a parameter $\eta = \eta(t, r)$, and a third arbitrary function $t_B(r)$:

$$R = \frac{M}{2E}\,(\cosh\eta - 1)\ , \qquad \sinh\eta - \eta = \frac{(2E)^{3/2}(t - t_B)}{M}\ ; \qquad E > 0\ , \tag{3.4}$$

$$R = M\left(\frac{1}{2}\,\eta^2\right)\ , \qquad \frac{1}{6}\,\eta^3 = \frac{(t - t_B)}{M}\ ; \qquad E = 0. \tag{3.5}$$

$$R = \frac{M}{(-2E)}\,(1 - \cos\eta)\ , \qquad \eta - \sin\eta = \frac{(-2E)^{3/2}(t - t_B)}{M}\ ; \qquad E < 0\ , \tag{3.6}$$

for hyperbolic, parabolic and elliptic solutions respectively [1]. Even if a non-zero cosmological constant had been retained, equation (3.2) can still be solved in terms of Weierstrass elliptic functions as has been discussed in [39, 45]. The third arbitrary function $t_B = t_B(r)$ is the local time at which $R = 0$, i.e. the local time of the big bang, so we have a non-simultaneous bang surface (this assumes we take $t > t_B$ above). The time reverse of the above equations are also possible solutions, in which case t_B is the time of the big crunch, and the hyperbolic and parabolic cases are collapsing models. Specification of the three arbitrary functions - $M(r)$, $E(r)$ and $t_B(r)$ - fully determines the model. They constitute a radial coordinate choice, and two physical relationships. If we differentiate (3.4) to get $\dot{R}$ and R' in terms of η and eliminate η from R' we get

$$R' = \left(\frac{M'}{M} - \frac{E'}{E}\right)R - \left\{t_B' - \left(\frac{3E'}{2E} - \frac{M'}{M}\right)(t - t_B)\right\}\dot{R}\ . \tag{3.7}$$

We can also get the same equation from (3.6), and starting from (3.5) we get (3.7) with $E'/E = 0$.

One thing worth mentioning is that there is a difference between the arbitrary function $M(r)$ we have here, and the sum of the masses of the particles that formed the gravitating body. The former is the mass that generates the gravitational field (hence called the gravitational mass). If we integrate (3.3) at constant time, then we get an expression for $M(r)$:

$$M = 4\pi\int_0^r \rho R^2 R'\,dr\ . \tag{3.8}$$

The total rest mass of the matter is found by integrating the density with respect to the volume element on a constant time surface. We use $\overline{M}$ to denote it:

$$\overline{M} = 4\pi\int_0^r \rho\,\frac{R^2 R'}{\sqrt{1 + 2E}}\,dr\ . \tag{3.9}$$

The difference between M and $\overline{M}$ depends on the sign of E, which is the energy. When $E > 0$ or $E = 0$ or $E < 0$ over the whole integral, M would be larger than or equal to or smaller than $\overline{M}$, as pointed out in [7].

[1] However, near the origin, it is the sign of RE/M that determines the type of solution.

3.1.1 The Friedmann-Lemaître-Robertson-Walker case

In the homogeneous FLRW case, we have $\rho = \rho(t)$ only. If η is to be independent of r at all times in (3.4) and (3.6), this implies that one needs to have the bang time t_B constant and E proportional to $M^{2/3}$, since the three arbitrary functions are functions of r only:

$$t_B = \text{constant} \ , \qquad E^{3/2}/M = \text{constant} \ . \tag{3.10}$$

These two equations define the FLRW case invariantly. For an FLRW universe, $R(t,r) = a(t)b(r)$ gives the FLRW scale factor, $a(t)$. When we exercise our freedom in choosing the radial coordinate to be $b(r) = r$, we then have $R'(t,r) = a(t)$. Together with the choice that $2E(r) = -kr^2$, the resulting RW metric looks like

$$ds^2 = -dt^2 + a^2(t)\left[\frac{dr^2}{1-kr^2} + r^2\left(d\theta^2 + \sin^2\theta d\phi^2\right)\right] \ , \tag{3.11}$$

where k is an arbitrary constant such that $k = +1$, $k = 0$ and $k = -1$ give us positively curved, flat and negatively curved spatial sections respectively. Another common choice is to have $2E(r) = -\sin^2 r$ and $2E(r) = -\sinh^2 r$ for the $k = +1$ and $k = -1$ cases respectively.

If we integrate equation (3.8), we then get

$$M = \frac{4\pi}{3}\rho R^3$$

as expected for the FLRW cases.

3.1.2 Behaviour near the origin

An origin occurs at $r = r_0$ if we have $R(t, r_0) = 0$ for any t. Without loss of generality, we will assume $r_0 = 0$ throughout this thesis since what we are really interested in is the behaviour of the three arbitrary functions near the origin of the spherical coordinates because they are functions of r only.

If one looks at equation (3.4) or (3.6), in the case when we have $r = 0$ and $R(\eta(t,0),0) = 0$ for every $0 < \eta < 2\pi$, it is essential to have

$$\frac{M}{2E} \to 0 \text{ as } r \to 0 \ . \tag{3.12}$$

In other words, this means that $2RE/M$ also has to be finite here. Of course, if we require the term $t - t_B$ remain finite when $r \to 0$, then we must also have

$$\frac{2E^{3/2}}{M} = \text{finite as } r \to 0 \ . \tag{3.13}$$

And the evolution equation (3.2) tells us that if we have $\dot{R}(t,0) = 0$ at all times, i.e. our origin remains an origin at all times, this requires that

$$E \to 0 \text{ and } \frac{M}{R} \to 0 \text{ as } r \to 0 \ . \tag{3.14}$$

Using the conditions (3.14) and (3.13) in conjunction with the fact that $2RE/M$ remains finite near the origin, we can then deduce that $M \propto E^{3/2}$ to the lowest order in r and also $E \sim R^2$ and $M \sim R^3$ on a constant time slice. From these conditions, one can easily see that the LTB model assumes FLRW form near the origin. However, this is not surprising at all since the LTB model is based on the spherical symmetry assumption.

3.1.3 The near-Parabolic case

One may have noticed from the three evolution equations (3.4)-(3.6) that the parabolic evolution is actually the $E \to 0$ limit of the other two evolutions, which is obtained by noting that $\eta/\sqrt{E}$ remains finite. Here, we use $f = 2E$ for all E. One can see that as we are approaching this borderline case, the evolution equations (3.4)-(3.6) are not well-behaved numerically. Also, in reality, it is very difficult, if not impossible, to obtain an exactly parabolic case numerically. Hence, a series expansion is needed in order to have reasonable numerical results for the near-Parabolic case.

Most of the series expansions for the near-Parabolic case can be found in [27]. However, here we will give a detailed derivation following the approach in [27], but for obtaining the series expansion for $\tau = t - t_B$ only since this is the only one that is essential to us. Let us first introduce two new variables $x \equiv f/M^{2/3}$, and $a \equiv R/M^{1/3}$. The parabolic limit now occurs when $x \to 0$, while R and τ remain finite. This requires

$$\eta \to 0 \text{ and } \frac{\eta}{\sqrt{x}} \to e \tag{3.15}$$

so that the new evolution parameter e remains finite for finite τ. Taylor series expansion expressions of τ and a for the hyperbolic case using equation (3.4) are just

$$\tau \approx \frac{e^3}{6} + \frac{xe^5}{120} + \frac{x^2e^7}{5040} + \frac{x^3e^9}{362880} + \cdots \tag{3.16}$$

$$a \approx \frac{e^2}{2} + \frac{xe^4}{24} + \frac{x^2e^6}{720} + \frac{x^3e^8}{40320} + \cdots \tag{3.17}$$

If we invert the series for a by writing e in series expansion form:

$$e \approx e_0 + e_1x + e_2x^2 + e_3x^3 + \cdots , \tag{3.18}$$

then substituting into (3.17), and solving for the coefficients e_i, we get

$$e \approx \sqrt{2a}\left(1 - \frac{1}{12}\,ax + \frac{3}{160}\,a^2x^2 - \frac{5}{896}\,a^3x^3 + \frac{35}{18432}\,a^4x^4 + \cdots\right) , \tag{3.19}$$

which we substitute into (3.16), and write it in terms of $\hat{R}$, M and f, giving

$$\tau \approx \sqrt{\frac{2R^3}{M}}\left(\frac{1}{3} - \frac{1}{20}\,\frac{Rf}{M} + \frac{3}{224}\,\frac{R^2f^2}{M^2} - \frac{5}{1152}\,\frac{R^3f^3}{M^3} + \frac{35}{22528}\,\frac{R^4f^4}{M^4} + \cdots\right) . \tag{3.20}$$

Equation (3.20) is the τ series expansion expression for the near-parabolic case. One can do the derivation using the elliptic evolution equations similarly.

3.1.4 Shell crossings

A shell crossing happens when an inner spherical shell of particles moves faster than an outer shell and eventually overtakes it. In fact, Bondi was aware of the possible existence of shell crossings, and excluded the possible occurrence of this type of singularity in his 1947 paper [7].

In the LTB model, the shell crossing singularities are different from the big bang or big crunch singularities. One of the distinctions between the two is that the former has only one metric component g_{rr} going to zero, i.e. $R' = 0$ and $R \neq 0$, with the singular surfaces being timelike, while the latter has the angular metric components $g_{\theta\theta}$ and $g_{\phi\phi}$ going to zero, with the singular surfaces being spacelike. Also, the frequency shift of light coming from a shell crossing is finitely red or blue, and if $R' \to 0$ where $M' > 0$, then the density ρ diverges. However, if $M' = 0$ where $R' \neq 0$, then this is just vacuum, and one doesn't normally consider $M' < 0$ where $R' > 0$. In contrast the bang surface has an infinite redshift except along a radial direction, which displays an infinite blueshift, and on the big bang surface or big crunch surface the density diverges [28, 38].

Although shell crossings are not considered as dangerous as the big bang or big crunch singularities, nevertheless, the assumptions that the matter can be represented by comoving coordinates and a single-particle four-velocity at each point in the LTB model do break down here. Hence, in all the cases we use for generating the fake data in order to test the ability of our numerical method in reproducing the correct results, we avoid the existence of shell crossings. The necessary and sufficient conditions obtained in [29] for no shell crossings in LTB models are given in the table below.

Table 3.1: Conditions for No Shell Crossings

$E \geq 0$	$E < 0$
$R' > 0$	
$t'_B \leq 0$ $E' \geq 0$ $M' \geq 0$ but no more than two equalities at once	$t'_B \leq 0$ $t'_B \geq \frac{-\pi M}{(-2E)^{3/2}} \left(\frac{M'}{M} - \frac{3E'}{2E} \right)$ $M' \geq 0$ but not both $M' = 0$ and $E' = 0$ at once
$R' = 0$	
$t'_B = 0$ $E' = 0$ $M' = 0$	$t'_B = 0$ $E' = 0$ $M' = 0$
$R' < 0$	
$t'_B \geq 0$ $E' \leq 0$ $M' \leq 0$ but no more than two equalities at once	$t'_B \geq 0$ $t'_B \leq \frac{-\pi M}{(-2E)^{3/2}} \left(\frac{M'}{M} - \frac{3E'}{2E} \right)$ $M' \leq 0$ but not both $M' = 0$ and $E' = 0$ at once

3.2 The observer's past null cone

The notation and null cone solution used here were first developed in [44]. However, they chose to work with the parabolic LTB model, and hence, their gauge choice which locates the null cone of the observer at one instant of time is simple. This gauge choice was later on generalised to all spatial sections, i.e. for all values of E, see MHE [43]. In this paper, they gave a complete outline of the observer's null cone in the LTB model, and how one can relate the LTB model to observables using this more general gauge choice. Therefore, in this and the next section, we follow the general outline given in MHE.

On the one hand specification of the three arbitrary functions is what determines the LTB model, and on the other $d_D(z)$ and $n(z)$ are what is given on the observer's past null cone. Therefore, we first need to locate the null cone, and then relate the LTB arbitrary functions to the given data.

Since human observations of the sky are essentially a single event on cosmological scales, we only need to be able to locate a single null cone; no general solution is needed. On radial null geodesics, we have $ds^2 = 0 = d\theta^2 = d\phi^2$. From (3.1), if the past null cone of the observation event $(t = t_0, r = 0)$ [2] is given by $t = \hat{t}(r)$, then $\hat{t}(r)$ satisfies

$$d\hat{t} = -\frac{R'[\hat{t}(r), r]}{\sqrt{1+2E}}\, dr = -\frac{\widehat{R'}}{\sqrt{1+2E}}\, dr \ . \tag{3.21}$$

We will denote a quantity evaluated on the observer's null cone, $t = \hat{t}(r)$, by a $\widehat{\ }$; for example $R[\hat{t}(r), r] \equiv \widehat{R}$, and we note that it is a function of r only instead of r, t. If we choose coordinate r in such a way that on the past null cone of (t_0, r), we have

$$\frac{R'[\hat{t}(r), r]}{\sqrt{1+2E}} = \frac{\widehat{R'}}{\sqrt{1+2E}} = 1 \ , \tag{3.22}$$

then the incoming radial null geodesics are given by

$$\hat{t}(r) = t_0 - r \ . \tag{3.23}$$

As noted, this only good for a single null cone.

With our coordinate choice (3.22), the density (3.3), and the Friedmann equation (3.2) on the past null cone then become

$$4\pi\hat{\rho}\hat{R}^2 = \frac{M'}{\sqrt{1+2E}} \ , \tag{3.24}$$

$$\dot{\widehat{R}} = \pm\sqrt{\frac{2M}{\hat{R}} + 2E(r)} \ . \tag{3.25}$$

Although we do not strictly know the sign of $\dot{\widehat{R}}$, it is fairly safe to assume that it is positive on our past null cone on the large scales that we are considering. From now on our $\dot{\widehat{R}}$ takes the form

$$\dot{\widehat{R}} = \sqrt{\frac{2M}{\hat{R}} + 2E(r)} \ . \tag{3.26}$$

The gauge equation is found from the total derivative of R on the null cone,

$$\frac{d\hat{R}}{dr} = \widehat{R'} + \dot{\widehat{R}}\frac{d\hat{t}}{dr} \ , \tag{3.27}$$

and this, together with (3.22), (3.23) and (3.25), leads to

$$\frac{d\hat{R}}{dr} - \sqrt{1+2E} = -\dot{\widehat{R}} = -\sqrt{\frac{2M}{\hat{R}} + 2E(r)} \ . \tag{3.28}$$

[2] When we work with the real observational data, this point is referred to as here and now. Hence, t_0 is the current age of the universe.

We can then obtain an expression for $1+2E(r)$ by squaring both sides and rearranging it,

$$1+2E=\left\{\frac{1}{2}\left[\left(\frac{d\hat{R}}{dr}\right)^2+1\right]-\frac{M}{\hat{R}}\right\}^2\Bigg/\left(\frac{d\hat{R}}{dr}\right)^2 \ . \tag{3.29}$$

As one can see, this expression tells us for which regions the spatial sections are hyperbolic $1+2E>1$, parabolic $1+2E=1$ or elliptic $1+2E<1$, based on data obtained from the null cone. We substitute (3.29) into (3.24) and rearrange it into the form

$$\frac{dM}{dr}+\left(\frac{4\pi\hat{\rho}\hat{R}}{\frac{d\hat{R}}{dr}}\right)M=\left(\frac{2\pi\hat{\rho}\hat{R}^2}{\frac{d\hat{R}}{dr}}\right)\left[\left(\frac{d\hat{R}}{dr}\right)^2+1\right] \ . \tag{3.30}$$

By evaluating (3.4), (3.5) and (3.6) on the null cone we then have

$$\hat{R}=\tfrac{M}{\mathcal{E}}\ \hat{\phi}_0 \ , \quad \hat{\xi}=\tfrac{\mathcal{E}^{3/2}\tau}{M(r)} \ , \tag{3.31}$$

where

$$\mathcal{E}(r)=\begin{cases}2E(r),\\ 1,\\ -2E(r),\end{cases} \quad \hat{\phi}_0=\begin{cases}\cosh\hat{\eta}-1,\\ \frac{1}{2}\hat{\eta}^2,\\ 1-\cos\hat{\eta},\end{cases} \quad \hat{\xi}=\begin{cases}\sinh\hat{\eta}-\hat{\eta},\\ \frac{1}{6}\hat{\eta}^3,\\ \hat{\eta}-\sin\hat{\eta},\end{cases} \quad \text{when} \begin{cases}E>0\\ E=0\\ E<0\end{cases} \tag{3.32}$$

and the proper time from the bang surface to the past null cone along the particle worldlines is described by

$$\tau(r)\equiv\hat{t}(r)-t_B(r)=t_0-r-t_B \ . \tag{3.33}$$

By rearranging the two expressions in equation (3.31) into

$$\hat{\phi}_0=\frac{\varepsilon\hat{R}}{M} \ , \tag{3.34}$$

and

$$\tau=\frac{M}{\varepsilon^{3/2}}\ \hat{\xi} \ , \tag{3.35}$$

using (3.29), (3.30) and (3.32), we can then solve for $\hat{\eta}$ and $\tau(r)$; and hence $t_B(r)$ from (3.33).

3.2.1 Redshift formula

Since the cosmological observations are given in terms of redshift rather than the unobservable coordinate r, we need to express all the relevant quantities in terms of redshift z. In order to do this, the redshift formula is developed here, and we will use this information in the next section for relating observables to the LTB model.

In the geometrical optics limit, we consider two light rays emitted from a given worldline (say, by a galaxy on its worldline) at r_{em} with time interval $\delta t_{em}=t^+(r_{em})-t^-(r_{em})$, where $t^+(r_{em})$ denotes the second emission time and $t^-(r_{em})$ denotes the first emission time. The rays are observed on the central worldline (the observer's worldline) with time interval $\delta t_{ob}=t^+(0)-t^-(0)$, where $t^-(0)$ denotes the time when the first emission is observed and $t^+(0)$ denotes the time when the second emission is observed.

Figure 3.1: Graphical demonstration of the calculation of the redshift between the observer and the galaxy.

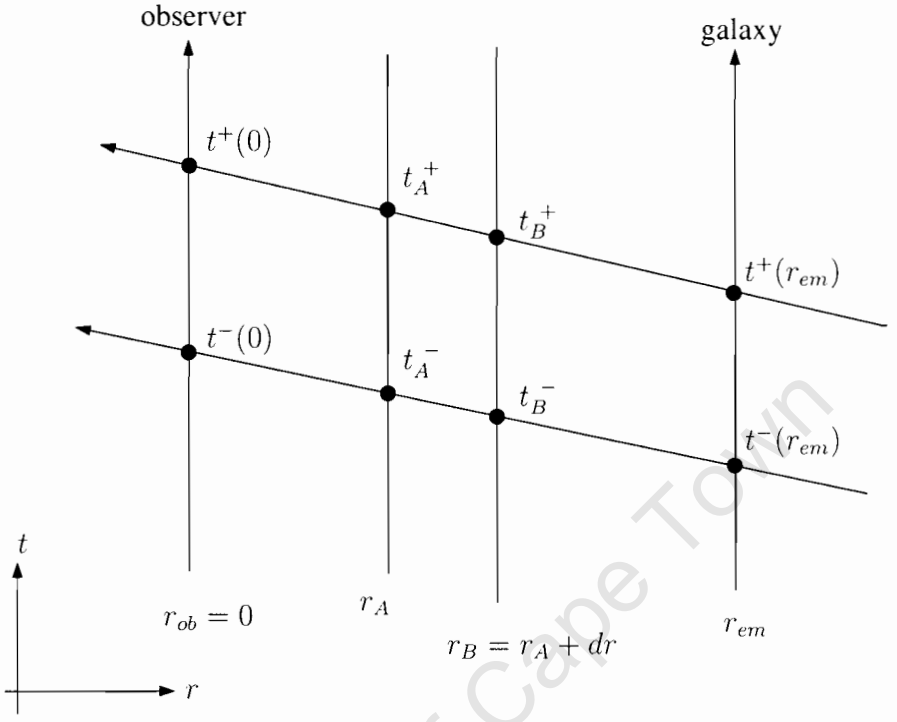

The equation for the redshift z is formulated as

$$1+z=\frac{\delta t_{ob}}{\delta t_{em}}\ . \tag{3.36}$$

The incoming radial null geodesics are given by

$$dt=-\frac{R'(t,r)}{\sqrt{1+2E}}\ dr\ .$$

For the two successive light rays, - and +, passing through two nearby comoving worldlines r_A and $r_B = r_A + dr$ at times t_A^-, t_B^-, t_A^+ and t_B^+; the difference between $\delta t_A = t_A^+ - t_A^-$ and $\delta t_B = t_B^+ - t_B^-$ is just

$$d(\delta t)=\delta t_B-\delta t_A=dt^+-dt^-=\frac{[-R'(t^+,r)+R'(t^-,r)]}{\sqrt{1+2E}}\ dr=-\frac{\frac{\partial}{\partial t}[R'(t,r)]\delta t}{\sqrt{1+2E}}\ dr\ . \tag{3.37}$$

where $dt^+ = dt_B^+ - dt_A^+$ and $dt^- = dt_B^- - dt_A^-$. Consequently

$$d\ln\delta t=-\frac{\frac{\partial}{\partial t}[R'(t,r)]}{\sqrt{1+2E}}\ dr\ , \tag{3.38}$$

which means that integrating along the light ray and applying this to the log of (3.36), the redshift is given by

$$\ln(1+z)=\int_0^{r_{em}}\frac{\dot{R}'(t,r)}{\sqrt{1+2E}}\ dr \tag{3.39}$$

for the central observer at $r = 0$, receiving signals from an emitter at $r = r_{em}$.

We need to find the redshift z explicitly in terms of r, $\hat{R}$ and $\hat{\rho}$, which we will later relate to observables. We differentiate (3.2) with respect to r obtaining

$$\frac{\dot{R}\,'}{\sqrt{1+2E}} = \frac{1}{\dot{R}}\left(\frac{M'}{R\sqrt{1+2E}} - \frac{MR'}{R^2\sqrt{1+2E}} + \frac{E'}{\sqrt{1+2E}}\right) , \tag{3.40}$$

and when evaluated on the observer's past null cone, we find

$$\frac{\widehat{\dot{R}'}}{\sqrt{1+2E}} = \frac{1}{\widehat{\dot{R}}}\left[\frac{M'}{\hat{R}\sqrt{1+2E}} - \frac{M}{\hat{R}^2} + \left(\sqrt{1+2E}\,\right)'\right] . \tag{3.41}$$

From (3.29), we can get the derivative of $\sqrt{1+2E}$

$$\left(\sqrt{1+2E}\,\right)' = \frac{d^2\hat{R}}{dr^2} - M'\Bigg/\left(\hat{R}\,\frac{d\hat{R}}{dr}\right) + \frac{M}{\hat{R}^2} - \sqrt{1+2E}\,\frac{d^2\hat{R}}{dr^2}\Bigg/\frac{d\hat{R}}{dr} . \tag{3.42}$$

If we use (3.24) to eliminate M', together with (3.42), equation (3.41) then becomes

$$\frac{\widehat{\dot{R}'}}{\sqrt{1+2E}} = \frac{1}{\widehat{\dot{R}}}\left(4\pi\hat{\rho}\hat{R} - 4\pi\hat{\rho}\hat{R}\sqrt{1+2E}\Bigg/\frac{d\hat{R}}{dr} + \frac{d^2\hat{R}}{dr^2} - \frac{d^2\hat{R}}{dr^2}\sqrt{1+2E}\Bigg/\frac{d\hat{R}}{dr}\right) ;$$

and using equation (3.28), it can be simplified to

$$\frac{\widehat{\dot{R}'}}{\sqrt{1+2E}} = -\left(\frac{d^2\hat{R}}{dr^2} + 4\pi\hat{\rho}\hat{R}\right)\Bigg/\frac{d\hat{R}}{dr} . \tag{3.43}$$

From (3.39), it now follows that

$$\frac{d}{dr}[\ln(1+z)] = -\left(\frac{d^2\hat{R}}{dr^2} + 4\pi\hat{\rho}\hat{R}\right)\Bigg/\frac{d\hat{R}}{dr} \tag{3.44}$$

with $z(0) = 0$. So theoretically we now have the redshift in terms of coordinate radius r from $\hat{R}(r)$ and $\hat{\rho}(r)$ directly, which is

$$\ln(1+z) = -\int_0^r \left(\frac{d^2\hat{R}}{dr^2} + 4\pi\hat{\rho}\hat{R}\right)\Bigg/\frac{d\hat{R}}{dr}\; dr . \tag{3.45}$$

3.2.2 Origin conditions

As previously mentioned, at the origin of spherical coordinates, $r = 0$, we have $R(t,0) = 0$ and $\dot{R}(t,0) = 0$ for all t. Hence, on the observer's past null cone equations (3.27) and (3.28) then become

$$\left.\frac{d\hat{R}}{dr}\right|_{r=0} = \widehat{R'} = \sqrt{1+2E} = 1 , \tag{3.46}$$

and thus $\hat{R} \approx r$ to lowest order near $r = 0$. From (3.24) we then find that

$$M' \approx 4\pi\hat{\rho}_0 r^2 , \quad M \approx \frac{4}{3}\,\pi\hat{\rho}_0 r^3 ; \tag{3.47}$$

and from (3.29) using a Taylor series for $\hat{R}$, and working to second order in r, we get

$$E \approx \left[\frac{1}{2} \left(\frac{d^2\hat{R}}{dr^2} \right)_0^2 - \frac{4}{3}\, \pi \hat{\rho}_0 \right] r^2 \ , \tag{3.48}$$

where $d^2\hat{R}/dr^2$ is finite when $r = 0$ and note that $W \approx 1 + 2E$. And equation (3.48) [3] satisfies what we have deduced earlier that $M \propto E^{3/2}$.

Also, if we differentiate both sides of equation (3.45) with respect to r, and substitute (3.46) into it, after rearranging the expression, we then get the origin condition for dz/dr (and hence z)

$$\frac{dz}{dr} \approx \left. \frac{d^2\hat{R}}{dz^2} \right|_0 \ . \tag{3.49}$$

3.3 Relating observables to the LTB model

For simplicity, we suppose there is only one type of cosmic source and we only consider bolometric luminosities as in MHE. It is assumed that the luminosity and the number density of each source can evolve with time; with the former written as an absolute bolometric luminosity L, and the latter as a mass per source, m. Isotropy about the Earth is assumed, and we also assume that the universe is described by zero-pressure matter - 'dust', and galaxies or perhaps clusters of galaxies are taken as the particles of this dust.

The two source evolution functions might naturally be expressed as functions of local proper time since the big bang, $L(\tau)$ and $m(\tau)$. However, one cannot be sure of the age of the objects at redshift z because the bang time is uncertain in a LTB model and also because the location of the null cone is uncertain. The proper time from bang to null cone will be a function of redshift, $\tau(z)$, and the projections of the evolution functions on the null cone are written as $\hat{L}$ and $\hat{m}$. Of course, $\tau(z)$ is unknown until we have solved for the LTB model that fits the data. For the sake of simplicity, we will take $\hat{L}$ and $\hat{m}$ to be given as function of z, and we use l for the apparent luminosity and n for the number count observations. In practice, many observational studies of evolution express their results in terms of z.

The area distance or equivalently the diameter distance is the true linear extent of the source over the measured angular size as mentioned in chapter two. This is by definition the same as the areal radius in the LTB model R, which multiplies the angular displacements to give proper distance tangentially. The projection onto the observer's null cone gives the observable quantity $\hat{R} = d_D$. The luminosity distance is measurable if we know the true absolute luminosity of the source at the time of emission $\hat{L}$. If the observed apparent luminosity is $l(z)$, then from the reciprocity theorem [16] we have [4]

$$\hat{R}(z) = \frac{1}{(1+z)^2} \sqrt{\frac{\hat{L}}{l}} \ . \tag{3.50}$$

Let the observed number density of sources in redshift space be $n(z)$ per steradian per unit redshift interval, hence the number observed in a given redshift interval and solid angle,

[3] Note that equation (22) given in MHE is incorrect. Their expression does not allow all three cases of E.
[4] Note that equation (31) given in MHE is incorrect.

$d\Omega$, is

$$n\ d\Omega\ dz\ , \tag{3.51}$$

and over the whole sky is

$$4\pi n\ dz\ . \tag{3.52}$$

Thus the total rest mass between z and $z+dz$ is

$$4\pi \hat{m} n\ dz\ , \tag{3.53}$$

where $\hat{m}(z) = m[\tau(z)]$ is the mass per source. Given the local proper density on the null cone $\hat{\rho}$, the total rest mass between r and $r+dr$ evaluated on the null cone is

$$\hat{\rho}\widehat{d^3V} = \hat{\rho}\ \frac{4\pi \hat{R}^2 \widehat{R'}}{\sqrt{1+2E}}\ dr\ , \tag{3.54}$$

where $\widehat{d^3V}$ is the proper volume on a constant time slice. Hence, from (3.53),(3.54) and (3.22), we get [5]

$$\hat{R}^2 \hat{\rho} = \hat{m} n \frac{dz}{dr}\ . \tag{3.55}$$

A graphical illustration relating the observed redshift space number density n to the proper density $\hat{\rho}$ can be found in chapter two, see figure 2.1.

We then transform (3.44) to be in terms of redshift z instead of coordinate r by first writing it as

$$\frac{d\hat{R}}{dr}\ \frac{dz}{dr} + \frac{d^2\hat{R}}{dr^2}\ (1+z) + 4\pi\hat{\rho}\hat{R}(1+z) = 0\ ,$$

and then applying

$$\frac{d\hat{R}}{dz}\ \frac{dz}{dr} = \frac{d\hat{R}}{dr}\ ,\quad \frac{d^2\hat{R}}{dr^2} = \frac{d\hat{R}}{dz}\ \frac{d^2z}{dr^2} + \frac{d^2\hat{R}}{dz^2}\ \left(\frac{dz}{dr}\right)^2\ ,$$

to get

$$\frac{d\hat{R}}{dz}\ \frac{d^2z}{dr^2}\ (1+z) + \left[\frac{d^2\hat{R}}{dz^2}\ (1+z) + \frac{d\hat{R}}{dz}\right]\left(\frac{dz}{dr}\right)^2 = -4\pi\hat{\rho}\hat{R}(1+z)\ . \tag{3.56}$$

Integrating with respect to r, and using (3.55) gives

$$\int_0^{\bar{r}} \frac{d}{d\bar{r}}\left[\frac{dz}{d\bar{r}}\ \frac{d\hat{R}}{dz}\ (1+z)\right]\ d\bar{r} = -\int_0^z 4\pi\hat{\rho}(\bar{z})\hat{R}(\bar{z})(1+\bar{z})\frac{dr}{d\bar{z}}\ d\bar{z}\ , \tag{3.57}$$

then

$$\frac{dz}{dr}\ \frac{d\hat{R}}{dz}\ (1+z) - 1 = -4\pi\int_0^z \frac{\hat{m}(\bar{z})n(\bar{z})}{\hat{R}(\bar{z})}\ (1+\bar{z})\ d\bar{z}\ , \tag{3.58}$$

where we have used the origin conditions $[(dz/dr)(d\hat{R}/dz)]_0 = [d\hat{R}/dr]_0 = 1$, and $z(0) = 0$. It follows that

$$\frac{dz}{dr} = \left[\frac{d\hat{R}}{dz}\ (1+z)\right]^{-1}\left[1 - 4\pi\int_0^z \frac{\hat{m}(\bar{z})n(\bar{z})}{\hat{R}(\bar{z})}\ (1+\bar{z})\ d\bar{z}\right]\ . \tag{3.59}$$

[5] We can get the origin limit for $\hat{m}n$ from equation (3.55), which is $\hat{m}n \approx \frac{r^2\hat{\rho}_0}{\frac{d^2\hat{R}}{dz^2}|_0}$.

As pointed out in MHE, the equation above differs from the equation (32) in [54], by a factor of $(1+z)$ due to the usage of different coordinate systems. We have to solve the null Raychaudhuri equation (3.56) to get $r(z)$ and thus $z(r)$. Equation (3.59) is a first integral of (3.56) and we integrate it one more time in order to obtain $r(z)$, the boundary conditions at the origin $r=0$ being

$$\frac{dz}{dr}(0) = \frac{dz}{d\hat{R}}(0)\frac{d\hat{R}}{dr}(0) = 1 \Big/ \frac{d\hat{R}}{dz}(0) \ , \tag{3.60}$$

and also

$$z(0) = 0 \Leftrightarrow r(z=0) = 0 \ ,$$

so that

$$r(z) = \int_0^z \left[\frac{d\hat{R}}{dz}(1+z)\right]\left[1 - 4\int_0^{\bar{z}} \frac{\hat{m}(\bar{z})n(\bar{z})}{\hat{R}(\bar{z})}(1+\bar{z})\,d\bar{z}\right]^{-1} d\tilde{z} \ . \tag{3.61}$$

3.3.1 Apparent horizons and the null cone

In the early universe, the universe is expanding so rapidly that the light rays that are headed towards us are actually getting further away. One can consider the set of photons that are all the same time away from the observation event on the central worldline to be an incoming wavefront, i.e. the wavefront is the intersection of the past null cone with a constant time surface. As the universe slows down, there comes a moment when the area of such a wavefront is stationary, and $R(t,r)$ has reached its maximum value. The locus of such points for all incoming wavefronts is the apparent horizon. Hence, for the LTB model, the maximum of the areal radius (or diameter distance) down the null cone is where the null cone crosses the apparent horizon. Since we have a maximum in $\hat{R}$ on our observer's past null cone, we locate this point by the calculation below.

Along the radial null geodesics, we recall the equation

$$\frac{d\hat{R}}{dr} = \widehat{R'} + \dot{\hat{R}}\frac{d\hat{t}}{dr}$$

from (3.27). Since the apparent horizon is the hypersurface in spacetime where $\hat{R}$ is momentarily at constant, by putting $d\hat{R}/dr = 0$ into (3.27) and using (3.22), (3.23) and (3.26), we then get

$$\sqrt{\frac{2M}{\hat{R}} + 2E} = \sqrt{1+2E} \ , \tag{3.62}$$

and hence

$$\hat{R} = 2M \ . \tag{3.63}$$

We will see that this locus presents us with a particular difficulty in our numerical reduction of null cone data.

Of course, in the case when the cosmological constant is not set to be zero, and if we are considering both the future and the past horizon; the calculation and the analysis will be more complicated. For more discussions on the details of the apparent horizons in LTB model, see [24, 36].

Chapter 4

Numerical Procedure

4.1 Algorithm

Our theoretical algorithm is adapted from MHE [43]. They showed that for any isotropic observations $l(z)$ and $n(z)$ with any given source evolution functions $\hat{L}(z)$ and $\hat{m}(z)$, a set of LTB functions can be found to make the LTB observational relations fit the observations. We develop a set of computer programmes that generates the values for the functions mentioned following the order in the steps below:

To obtain the LTB mass, energy and Bang time functions (M, E and t_B respectively) from observational data and source evolution, we would proceed as follows:

(i) take the discrete observed data for $l(z,\theta,\phi)$ and $n(z,\theta,\phi)$, average it over all angles to obtain $l(z)$ and $n(z)$. We may wish first to correct the data for known distortions and selection effects due to proper motions, absorption, shot noise, image distortions, etc.;

(ii) choose evolution functions $\hat{L}(z)$ and $\hat{m}(z)$ based on whatever observations and theoretical arguments may be mustered;

(iii) determine $\hat{R}(z)$ from $\hat{L}(z)$ and $l(z)$ using (3.50), this is then our first input data function and we have $4\pi\hat{m}n$ as our second input data function;

(iv) obtain the differential equations (DEs) d^2r/dz^2 and dM/dz [1] discretise them in a form suitable for numerical integrations, and then use the data z, $\hat{R}$ and $4\pi\hat{m}n$ to solve for $r(z)$ with $M(z)$ and $E(z)$ follow directly;

(v) solve for $\hat{\eta}$ from (3.34) and (3.32);

(vi) solve for $\tau(r)$ from (3.35) and (3.32) - $L(\tau)$ and $m(\tau)$ could now be found;

(vii) determine $t_B(r)$ from (3.33).

Note that this algorithm is slightly different from the one given in MHE, but within the same spirit. In the original algorithm from MHE, it was suggested that instead of the discretisation of the DEs, we would actually fit the discrete data to some smooth analytic functions, such as polynomials. However, this requires one to perform some kind of statistical fitting to the discrete data (a simple example is the least squares fit), all of which is extra processing. Even if one has done so successfully, it is still required to discretise all the smooth data functions in order to be able to integrate them numerically, since the numerical integration is in fact a discrete procedure. Therefore, with all the observational data being discrete, and the necessity of integrating them numerically; the most natural thing to do here is to collect them into redshift bins and discretise the DEs that we have. The procedure for the binning of the data and discretisation of the DEs are described in

[1] They will be introduced in the next section.

section 4.4. We shall see that the DEs are singular where $\hat{R}$ is maximum, and thus a series expansion about that point is required to avoid numerical divergence.

Let us now look at figure 4.1. Approach I is what we would have followed if we were working with the real observational data. However, in this thesis, we have not reached the stage of working with the real data, hence, approach II is the actual numerical algorithm that we take for developing the computer programmes. At the end of the algorithm, we need to plot the three arbitrary functions M, E and t_B in order to have a better sense of what type of LTB model we get out of the data. In the step where it says "Integration routines" in figure 4.1, it can actually be subdivided into four steps which are given below:

$*$ Deduce the origin parameters and output for the first 3 data points, i.e. at $z = 0$, $z = 1/2\delta z$ and $z = 3/2\delta z$, see later sections for more details.

$*$ Use numerical DE solvers, both Euler integration and also a second order Runge-Kutta method, for solving the DEs up to just before we reach the maximum in $\hat{R}$.

$*$ Determine the point where we switch to the series expansion in order to carry our numerics through the maximum in $\hat{R}$ and evaluate a matching value for the numerical integration and series expansion, and calculate the series expansion of r, ϕ, M and E through the maximum in $\hat{R}$.

$*$ Evaluate another matching value for switching back from the series expansion to numerical integration, and continue to solve the DEs numerically up to $z = 3$.

Detailed numerical procedures for these steps above are discussed in later sections.

Figure 4.1: A simple outline of the algorithm used in developing the numerical procedure.

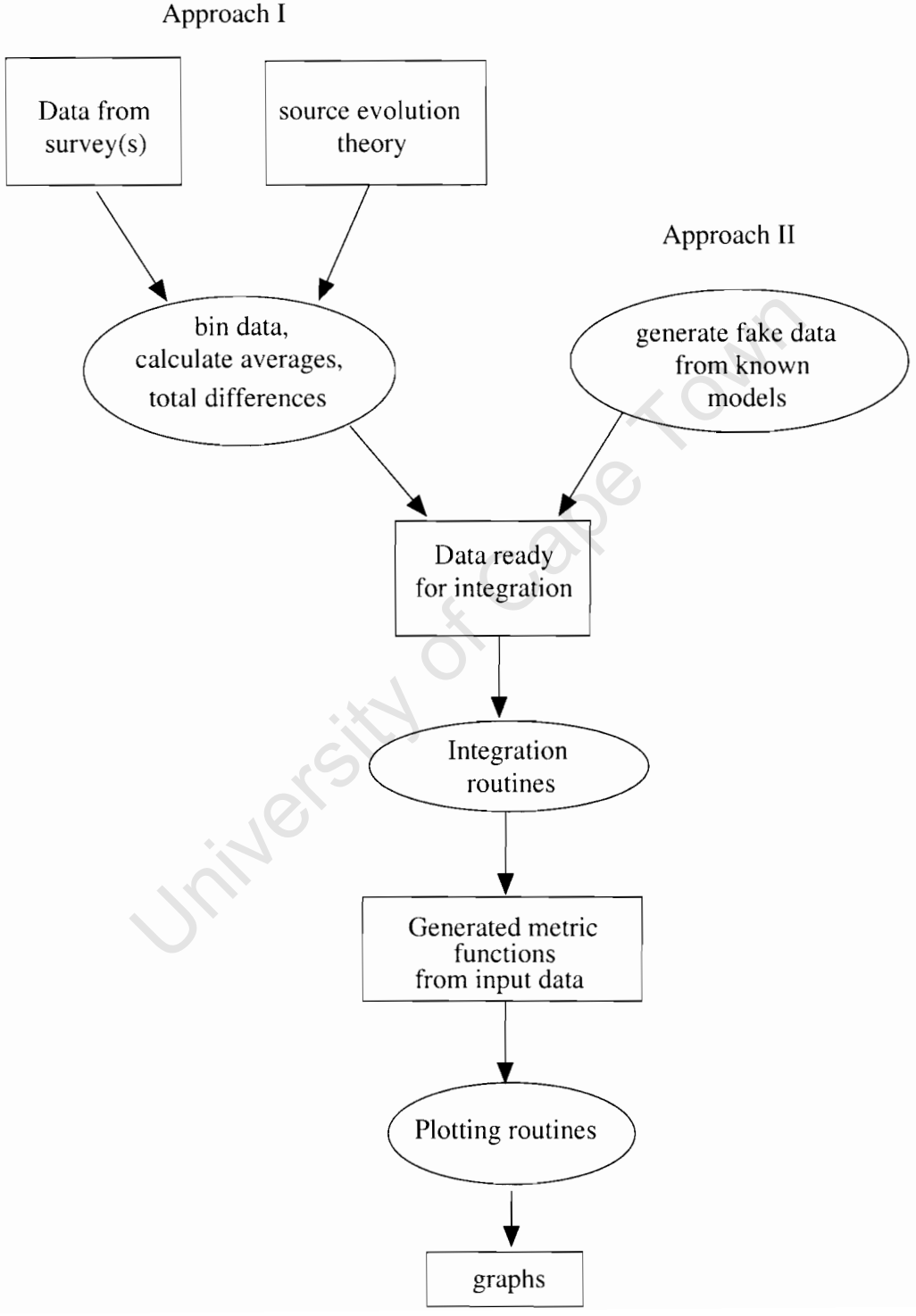

4.2 The differential equations

Most of the equations developed in chapter 3 are given as differential equations, and also it would be numerically easier to integrate the DEs than evaluate integrals. Therefore, we need to have a set of DEs, derived from the results in chapter 3, that will generate the values of r, M, E and hence t_B from the observations. The LTB model that we get from the observations is thus deduced.

Although equation (3.30) gives us a DE for M, however, it is expressed in terms of the unobservable r. If we substitute (3.55) into (3.30) and rewrite it as dM/dz instead of dM/dr, we then get

$$\frac{dM}{dz} = -\left(\frac{4\pi\hat{m}n}{\hat{R}}\,\frac{dr}{dz}\,\frac{dz}{d\hat{R}}\right)M + \left(2\pi\hat{m}n\,\frac{dr}{dz}\,\frac{dz}{d\hat{R}}\right)\left[\left(\frac{d\hat{R}}{dz}\right)^2\left(\frac{dz}{dr}\right)^2 + 1\right] . \tag{4.1}$$

As for $E(z)$, we have an expression for $1 + 2E(r)$ from (3.29). If we transform it into a function of z, and take square root of both sides, we then have

$$\sqrt{1+2E(z)} = \left\{\frac{1}{2}\left[\left(\frac{d\hat{R}}{dz}\right)^2\left(\frac{dz}{dr}\right)^2 + 1\right] - \frac{M(z)}{\hat{R}(z)}\right\} \Bigg/ \left[\frac{d\hat{R}}{dz}\,\frac{dz}{dr}\right] . \tag{4.2}$$

We have the term dr/dz in equations (4.1) and (4.2), so before we can simplify them further, we need to have an expression for dr/dz in differential form.

We want to generate values for r as a function of z. Even though equation (3.61) is expressed in terms of observables, it is in the form of an integral instead of a DE. So we differentiate both sides (with respect to z) once and take the inverse, and we rewrite it with the second integral on one side; this gives us

$$\frac{d\hat{R}}{dz}\,(1+z)\,\frac{dz}{dr} - 1 = -4\pi\int_0^z \frac{\hat{m}(\overline{z})n(\overline{z})}{\hat{R}(\overline{z})}\,(1+\overline{z})\,d\overline{z} .$$

If we differentiate both sides of the above equation with respect to z again, and multiply by dz/dr; rewriting it so that all terms involving $\hat{R}$ (and hence $d\hat{R}/dz$ and $d^2\hat{R}/dz^2$) are on one side of the equation. We then have a second order DE:

$$\frac{d^2z}{dr^2} = -\left[\frac{d\hat{R}}{dz}\,(1+z)\right]^{-1}\left\{\left[\frac{d^2\hat{R}}{dz^2}\,(1+z) + \frac{d\hat{R}}{dz}\right]\left(\frac{dz}{dr}\right) + \frac{4\pi\hat{m}(z)n(z)}{\hat{R}(z)}\,(1+z)\right\}\left(\frac{dz}{dr}\right) . \tag{4.3}$$

We use

$$\frac{dr}{dz} = 1 \Big/ \frac{dz}{dr}$$

and

$$\frac{d^2r}{dz^2} = \frac{dr}{dz}\,\frac{d}{dr}\left(1 \Big/ \frac{dz}{dr}\right) = -\left(\frac{dr}{dz}\right)^3\frac{d^2z}{dr^2} ;$$

together with equation (4.3) to get

$$\frac{d^2r}{dz^2} = \left[\frac{d\hat{R}}{dz}\,(1+z)\right]^{-1}\left\{\left[\frac{d^2\hat{R}}{dz^2}\,(1+z)+\frac{d\hat{R}}{dz}\right]\left(\frac{dz}{dr}\right) + \frac{4\pi\hat{m}n}{\hat{R}}\,(1+z)\right\}\left(\frac{dr}{dz}\right)^2 , \tag{4.4}$$

which is a second order DE for $r(z)$. Since we want to solve all our DEs (and hence get the values for our functions r, M and E) in parallel, we need to introduce a new variable such that we can rewrite (4.4) as two first order differential equations.

We introduce a new variable $\phi = \phi(z)$, defined by

$$\frac{dr}{dz} = \phi , \tag{4.5}$$

and equation (4.4) then becomes

$$\frac{d\phi}{dz} = \left\{\frac{1}{1+z} + \frac{\frac{d^2\hat{R}}{dz^2} + \frac{4\pi\hat{m}n\phi}{\hat{R}}}{\frac{d\hat{R}}{dz}}\right\}\phi . \tag{4.6}$$

If we substitute the inverse of (4.5) into (4.2) and (4.1) and rearrange them, we then have

$$\frac{dM}{dz} = 4\pi\hat{m}n\sqrt{1+2E} , \tag{4.7}$$

where another new variable $W = W(z)$ is defined by

$$W \equiv \sqrt{1+2E} = \frac{\frac{d\hat{R}}{dz}}{2\phi} + \frac{\left(1-\frac{2M}{\hat{R}}\right)\phi}{2\frac{d\hat{R}}{dz}} . \tag{4.8}$$

Hence, equations (4.5), (4.6) and (4.7) with (4.8) give us a set of coupled first order DEs that we use in order to generate the values for $r(z)$, $M(z)$ and $W(z)$ (or $E(z)$) from the observational data. Note that from equation (4.6), if we know the values for $\hat{R}$ and $4\pi\hat{m}n$, we can then solve for ϕ independently without knowing the values of r, M and W; while solving for r, M and W depends on knowing ϕ. This feature between ϕ and other variables will become constructive to us later on.

After solving these DEs, we have values for two out of the three LTB arbitrary functions. In order to generate values for the third one, t_B, we need to generate values for $\hat{\eta}$ and τ first. We know the values of $\hat{R}$, r, M and W, so using equations (3.32) and (3.34), we can generate values of $\hat{\eta}$ for the hyperbolic and elliptic cases. From these $\hat{\eta}$ values and equations (3.32) and (3.35), we can then get values of τ. However, we do have a borderline case – the near-parabolic case, as pointed out in the previous chapter. Equation (3.20) is then used for obtaining the values of τ from $\hat{R}$, M and E. Now we have generated τ values for all possible cases, we can then generate our third arbitrary function t_B from (3.33).

Before we go on any further, however, there are a few things worth considering first – our DEs (4.5)-(4.8) become singular when we reach the maximum in the areal radius (diameter distance) $\hat{R}$, i.e. $d\hat{R}/dz = 0$. From equation (3.63) in the previous chapter, we know that at the maximum of $\hat{R}$, we have $\hat{R} = 2M$. If one looks at the DE in equations

(4.7) and (4.8), it actually contain zero over zero at this point, and any numerical method will break down here. Further, rewriting (4.6) as

$$\frac{d^2\hat{R}}{dz^2} + \frac{4\pi\hat{m}n}{\hat{R}}\,\phi = \frac{d\hat{R}}{dz}\left(\frac{1}{\phi}\,\frac{d\phi}{dz} - \frac{1}{1+z}\right)$$

shows $d^2\hat{R}/dz^2 = 4\pi\hat{m}n/\hat{R}$ where $d\hat{R}/dz = 0$. There is no problematic behaviour of ϕ here, as can be verified in the FLRW case. Hence, in order to carry our numerics through this point, we need to perform a series expansion near the maximum in $\hat{R}$ for $\hat{R}(z)$, $\hat{m}n(z)$, $\phi(z)$, $M(z)$ and $W(z)$. This problem is dealt with in the next section; and we use $\hat{R}_{max}$ to denote the maximum in $\hat{R}$, and its corresponding z value is called z_m.

Let us also look at how the DEs behave near the origin, i.e. $z = 0$. Since r and z have a linear relation, from the origin conditions discussed in the previous chapter, we know that near the origin, $\hat{R} \sim z$, $4\pi\hat{m}n \sim z^2$, $d\hat{R}/dz =$ finite, $d^2\hat{R}/dz^2 =$ finite and $M \sim z^3$. Also we know that $dz/dr(0) = 1/(d\hat{R}/dz(0))$, so $\phi =$ finite. Hence, our DEs are well behaved near the origin. Since a well-behaved LTB origin is RW-like, we find the origin limits are $r(0) = 0$, $\phi(0) = d\hat{R}/dz(0) = 1/H_0$, $M(0) = 0$, $E(0) = 0$, $\hat{R}(0) = 0$ and $d^2\hat{R}/dz^2(0) = -(3+q_0)/H_0$.

4.3 Series Expansion near $\hat{R}_{max}$

What we need to do now is a series expansion near $\hat{R}_{max}$ for all our functions. Let us say that $\hat{R}_{max}$ occurs at z_m (as mentioned in the previous section), $\hat{m}n(z_m) = (\hat{m}n)_0$, and we define $dz = z - z_m$. So the series expansions for $\hat{m}n(z)$, $\hat{R}(z)$, $\phi(z)$, $M(z)$ and $W(z)$ have the form

$$\hat{m}n(z) = (\hat{m}n)_0 + (\hat{m}n)_1 dz + (\hat{m}n)_2 dz^2 + (\hat{m}n)_3 dz^3 + \cdots\,, \tag{4.9}$$

$$\hat{R}(z) = \hat{R}_{max} + R_2 dz^2 + R_3 dz^3 + R_4 dz^4 + R_5 dz^5 + \cdots\,, \tag{4.10}$$

$$\phi(z) = \phi_0 + \phi_1 dz + \phi_2 dz^2 + \phi_3 dz^3 + \cdots\,, \tag{4.11}$$

$$M(z) = M_0 + M_1 dz + M_2 dz^2 + M_3 dz^3 + \cdots\,, \tag{4.12}$$

and

$$W(z) = W_0 + W_1 dz + W_2 dz^2 + \cdots\,. \tag{4.13}$$

Hence,

$$\frac{d\hat{R}}{dz} = 2R_2 dz + 3R_3 dz^2 + 4R_4 dz^3 + 5R_5 dz^4 + \cdots\,. \tag{4.14}$$

and

$$\frac{d^2\hat{R}}{dz^2} = 2R_2 + 6R_3 dz + 12R_4 dz^2 + 20R_5 dz^3 + \cdots\,. \tag{4.15}$$

From the $\hat{R}$ and $\hat{m}n$ data, we can easily determine the values of $\hat{R}_{max}$, $(\hat{m}n)_0$ and z_m, and thus the remaining $\hat{R}(z)$ and $\hat{m}n(z)$ coefficients can be evaluated by simply performing a least squares fit using the data values near $\hat{R}_{max}$ and the z values near z_m. In order to obtain the expressions for the coefficients in the $\phi(z)$, $M(z)$ and $W(z)$ series, we need to substitute (4.9)-(4.13) into our DEs (4.5)-(4.8). The resulting expressions are given below

$$M_0 = \frac{\hat{R}_{max}}{2}\,, \tag{4.16}$$

$$M_1 = M_1\,, \tag{4.17}$$

$$M_2 = \left(\frac{1}{1+z_m} + \frac{(\hat{m}n)_1}{(\hat{m}n)_0} \right) \frac{M_1}{2} - \frac{R_2}{2} - \frac{8\pi^2 (\hat{m}n)_0^{\,2}}{\hat{R}_{max}} \ , \tag{4.18}$$

$$M_3 = \left(-\frac{R_2}{3\hat{R}_{max}} + \frac{(\hat{m}n)_2}{3(\hat{m}n)_0} + \frac{(\hat{m}n)_1}{3(\hat{m}n)_0\,(1+z_m)} \right) M_1 - \frac{1}{4} \left(\frac{R_2}{1+z_m} + \frac{(\hat{m}n)_1 R_2}{(\hat{m}n)_0} + R_3 \right) - \frac{8\pi^2 (\hat{m}n)_0 (\hat{m}n)_1}{\hat{R}_{max}} \ ; \tag{4.19}$$

$$\phi_0 = \frac{-\hat{R}_{max} R_2}{2\pi (\hat{m}n)_0} \ , \tag{4.20}$$

$$\phi_1 = \left(\frac{(\hat{m}n)_1 R_2}{(\hat{m}n)_0} - \frac{R_2}{1+z_m} - 3R_3 \right) \frac{\hat{R}_{max}}{4\pi (\hat{m}n)_0} \ , \tag{4.21}$$

$$\phi_2 = \left(\frac{3(\hat{m}n)_1 R_3}{2(\hat{m}n)_0} - \frac{(\hat{m}n)_1^{\,2} R_2}{2(\hat{m}n)_0^{\,2}} - 4R_4 + \frac{2(\hat{m}n)_2 R_2}{3(\hat{m}n)_0} - \frac{2R_2^{\,2}}{3\hat{R}_{max}} - \frac{3R_3}{2\,(1+z_m)} + \frac{2(\hat{m}n)_1 R_2}{3(\hat{m}n)_0\,(1+z_m)} + \frac{R_2}{2\,(1+z_m)^2} \right) \frac{\hat{R}_{max}}{4\pi (\hat{m}n)_0} \ , \tag{4.22}$$

$$\phi_3 = \left(-\frac{3(\hat{m}n)_1^{\,2} R_3}{4(\hat{m}n)_0^{\,2}} + \frac{(\hat{m}n)_1 R_3}{(\hat{m}n)_0\,(1+z_m)} + \frac{(\hat{m}n)_2 R_3}{(\hat{m}n)_0} - \frac{3R_2 R_3}{2\hat{R}_{max}} - \frac{R_2}{4\,(1+z_m)^3} - 5R_5 - \frac{(\hat{m}n)_1 R_2}{4(\hat{m}n)_0\,(1+z_m)^2} - \frac{5(\hat{m}n)_0^{\,2} R_2}{12(\hat{m}n)_0^{\,2}\,(1+z_m)} + \frac{(\hat{m}n)_2 R_2}{2(\hat{m}n)_0\,(1+z_m)} - \frac{R_2^{\,2}}{2\hat{R}_{max}\,(1+z_m)} - \frac{2R_4}{1+z_m} + \frac{(\hat{m}n)_1^{\,3} R_2}{4(\hat{m}n)_0^{\,3}} - \frac{2(\hat{m}n)_1 (\hat{m}n)_2 R_2}{3(\hat{m}n)_0^{\,2}} + \frac{(\hat{m}n)_1 R_2^{\,2}}{6\hat{R}_{max}(\hat{m}n)_0} + \frac{2(\hat{m}n)_1 R_4}{(\hat{m}n)_0} + \frac{3R_3}{4\,(1+z_m)^2} + \frac{(\hat{m}n)_3 R_2}{2(\hat{m}n)_0} \right) \frac{\hat{R}_{max}}{4\pi (\hat{m}n)_0} \ ; \tag{4.23}$$

and

$$W_0 = \frac{M_1}{4\pi (\hat{m}n)_0} \ , \tag{4.24}$$

$$W_1 = \frac{M_1}{4\pi (\hat{m}n)_0\,(1+z_m)} - \frac{R_2}{4\pi (\hat{m}n)_0} - \frac{4\pi (\hat{m}n)_0}{\hat{R}_{max}} \ , \tag{4.25}$$

$$W_2 = -\frac{R_2 M_1}{4\pi (\hat{m}n)_0 \hat{R}_{max}} - \frac{3R_3}{16\pi (\hat{m}n)_0} + \frac{(\hat{m}n)_1 R_2}{16\pi (\hat{m}n)_0^{\,2}} - \frac{3R_2}{16\pi (\hat{m}n)_0\,(1+z_m)} - \frac{2\pi (\hat{m}n)_1}{\hat{R}_{max}} \ . \tag{4.26}$$

From (4.20)-(4.23) we can see that all $\phi(z)$ coefficients are determinable once we know the values of z_m and all coefficients of $\hat{R}$ and $4\pi\hat{m}n$. Using (4.5), the series expansion for r is simply

$$r(z) = r_0 + \phi_0 dz + \frac{\phi_1}{2}\, dz^2 + \frac{\phi_2}{3}\, dz^3 + \frac{\phi_3}{4}\, dz^4 + \cdots \ , \tag{4.27}$$

where $r_0 = r(z_m)$ is the integration constant. Currently, we do not have a value for r_0, however, we will be able to solve for r_0 once we find out where we connect the series expansion to the numerical integration, since at the connecting point, the value of any function for both methods should be the same. Also note that M_0 is obtained directly from $\hat{R}_{max}$ without any further information. The only problem we are facing now is that if we look at expressions (4.18), (4.19) and (4.24)-(4.26), they all depend linearly on M_1.

Unfortunately, no information about M_1 can be obtained when we carry out the series expansion as one can see from (4.17). Despite this, it is still possible to obtain a value for M_1 by substituting a known value , say M_a at z_a, where z_a is some distance away from z_m, into (4.12). A graphical illustration of this approach is shown in Figure 4.2:

Figure 4.2: Illustration for solving for M_1 using a known value of M_a at z_a.

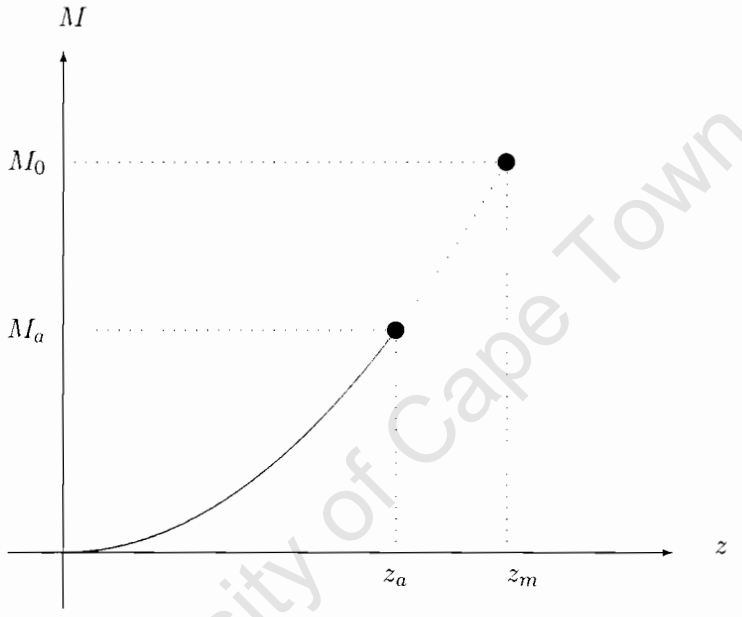

However, this means that we are trying to match the M value of the series expansion and the result of the numerical integration at this point. There is actually another way of solving for a value for M_1. Instead of matching M at z_a, we match W at z_a. Since all W coefficients (4.24)-(4.26) have a linear dependence on M_1, which is the only unknown here, we can easily solve for M_1. With two possible ways of connecting the series expansion part to the numerical integration part, we will have to decide which function to match at z_a in order to generate series expansion values for M and W. Later on we will experiment with which matching to use.

4.4 Discretisation of the differential equations and data near the origin

In section 4.1, we explained why we decided to discretise the DEs instead of fitting the data to some smooth function and then discretising it in order to perform the numerical integration. In this section, we talk about the actual numerical process for the discretisation of the DEs and the integration method that we use.

If we let the bin size be δz, and we average over all the data values within each bin, for example the $\hat{R}$ values within a given z bin as shown in Figure 4.3, then the average $\hat{R}$ values that we use are located in the middle of each bin. Thus we have the first value of $\hat{R}$

at $z = \delta z/2$. We can then get the discretised versions of $d\hat{R}/dz$ and $d^2\hat{R}/dz^2$ from the first and second differences of $\hat{R}$ where we have

$$\Delta\hat{R}_i = \frac{\hat{R}_{i+1} - \hat{R}_i}{\delta z}$$

and

$$\Delta^2\hat{R}_j = \frac{\Delta\hat{R}_{j+1} - \Delta\hat{R}_j}{\delta z}$$

for any positive integer i and j as represented in the figure. It takes two δz bins to get $\Delta\hat{R}_1$ (the first value of the first difference) at $z = \delta z$ and all the values are located at $z = k\delta z$ for any positive integer k. However, it takes three δz bins to get $\Delta^2\hat{R}_1$ (the first value of second difference and hence the first value of $d^2\hat{R}/dz^2$) at $z = 3\delta z/2$, therefore, all the values are located in the middle of each bin. Since we want to have a complete set of data at each z value, we take the average of the two neighbouring $\Delta\hat{R}_i$ data points to get all our data at the half δz locations (in the middle of each bin). In doing so, we will not have data values at the origin or at $z = \delta z/2$, since the first complete data set is at $z = 3/2\delta z$. But we know that LTB is RW like near the origin due to the fact that it assumes spherical symmetry. For that reason, the series expansions of the RW expressions are used for finding the RW parameters that fit the data values at the origin and at $z = \delta z/2$, i.e. we determine the central values of H_0 (Hubble constant) and q_0 (deceleration parameter) from the data near $z = 0$.

Figure 4.3: Illustration of the discretisation of DEs.

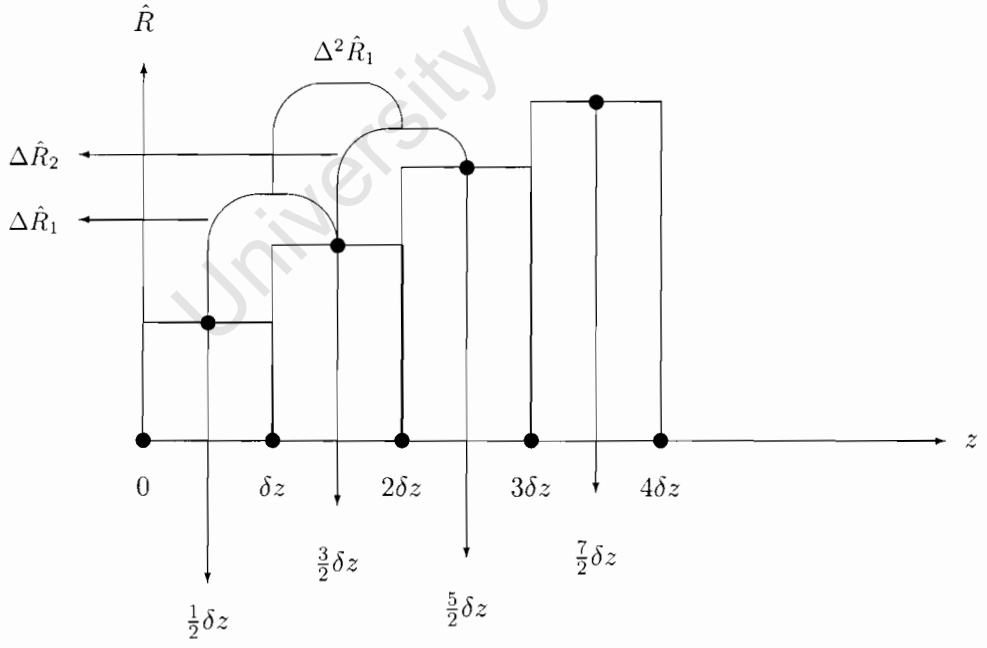

So we take the standard RW expressions for $\hat{R}(z)$ and $4\pi\hat{m}n(z)$:

$$\hat{R}(z) = \frac{q_0 z + (1 - q_0)\left(1 - \sqrt{2q_0 z + 1}\ \right)}{H_0 {q_0}^2 (1 + z)^2}\ , \tag{4.28}$$

$$4\pi\hat{m}n(z) = \frac{3}{H_0{q_0}^3} \frac{\left[q_0 z + (1-q_0)\left(1-\sqrt{2q_0z+1}\ \right)\right]^2}{(1+z)^3\sqrt{2q_0z+1}}\ ; \tag{4.29}$$

and we do series expansions of them near the origin:

$$\hat{R} \approx \frac{1}{H_0}\ z - \frac{(3+q_0)}{2H_0}\ z^2 + \frac{4+q_0+{q_0}^2}{2H_0}\ z^3 + \cdots\ , \tag{4.30}$$

and

$$4\pi\hat{m}n \approx \frac{3q_0}{H_0}\ z^2 - \frac{6q_0(1+q_0)}{H_0}\ z^3 + \frac{3q_0(15{q_0}^2+14q_0+13)}{4H_0}\ z^4 + \cdots\ . \tag{4.31}$$

We test the accuracy of the generated H_0 and q_0 values using $z = 3/2dz$, and $\hat{R}$ and $4\pi\hat{m}n$ values at this same z since this is where we have the first complete set of data according to available observational data and the way we discretise our DEs, and therefore, find the combination with the best consistent accuracy for different q_0 values. There are four different combinations of number of terms used from the series expansion expressions: with both of q_0 and H_0 to the lowest order in their series expansion expressions, both going up to order two, both to the two lowest order terms, and both up to order three. We find that the third case – both to the two lowest order terms – gives us the best accuracy out of these four different combinations. We also find that in general, both equations (4.30) and (4.31) with same number of terms gives us better accuracy. We can then get expressions for H_0 and q_0 near the origin in terms of z, $\hat{R}$ and $4\pi\hat{m}n$ only. The results for the 3rd case are

$$q_0 = -\frac{\sqrt{4\pi\hat{m}n^2 + 144\hat{R}^2\ z^2 + \hat{R}^2\ (-144z+36) + 4\pi\hat{m}n\hat{R}\ (120z-84)}}{24z\hat{R}}$$

$$+\frac{4\pi\hat{m}n + \hat{R}\ (12z+6)}{24z\hat{R}}\ , \tag{4.32}$$

and

$$H_0 = -\frac{3q_0z^2(-1+2q_0z+2z)}{4\pi\hat{m}n}\ . \tag{4.33}$$

Now we have a way of determining the origin values for H_0 and q_0 from the data. If we want to generate values for r, ϕ, M and W at $z = 1/2dz$ and the origin numerically from the RW expressions given in Appendix B, then one can perform series expansions of them too, since the values of z are small. They are:

$$M_{RW} \approx \frac{q_0}{H_0}z^3 - \frac{3q_0(1+q_0)}{2H_0}z^4 + \frac{3q_0(3+2q_0+3{q_0}^2)}{4H_0}z^5$$

$$-\frac{q_0(28{q_0}^3+12{q_0}^2+15q_0+25)}{8H_0}z^6 + \cdots\ ; \tag{4.34}$$

$$\phi_{RW} \approx \frac{1}{H_0} - \frac{2+q_0}{H_0}z + \frac{3{q_0}^2+4q_0+6}{2H_0}z^2 - \frac{5{q_0}^3+6{q_0}^2+6q_0+8}{2H_0}z^3 + \cdots\ ; \tag{4.35}$$

$$2E_{RW} \approx (1-2q_0)z^2 - q_0(1-2q_0)z^3 + \frac{1}{4}(1-2q_0)(5{q_0}^2-2q_0+1)z^4$$

$$-\frac{1}{4}(1-2q_0)(7{q_0}^3-4{q_0}^2+1)z^5 + \cdots\ ; \tag{4.36}$$

$$r_{RW} \approx \frac{1}{H_0}z - \frac{2+q_0}{2H_0}z^2 + \frac{3{q_0}^2+4q_0+6}{6H_0}z^3 - \frac{5{q_0}^3+6{q_0}^2+6q_0+8}{8H_0}z^4 + \cdots ; \quad (4.37)$$

and these expressions are valid for any q_0. For $q_0 < 1/2$ and $q_0 > 1/2$, the τ series expansions for the RW equations take the form:

$$\tau_{RW} \approx \frac{\sqrt{1-2q_0} + q_0 \ln\left(\frac{1-\sqrt{1-2q_0}}{1+\sqrt{1-2q_0}}\right)}{H_0(1-2q_0)^{3/2}} - \frac{1}{H_0}z + \frac{2+q_0}{2H_0}z^2$$
$$- \frac{3{q_0}^2+4q_0+6}{6H_0}z^3 + \frac{5{q_0}^3+6{q_0}^3+6q_0+8}{8H_0}z^4 + \cdots , \quad (4.38)$$

$$\tau_{RW} \approx \frac{\sin^{-1}(\frac{q_0-1}{q_0})q_0 + \frac{\pi}{2}\ q_0 - \sqrt{2q_0-1}}{H_0(2q_0-1)^{3/2}} - \frac{1}{H_0}z + \frac{2+q_0}{2H_0}z^2 - \frac{3{q_0}^2+4q_0+6}{6H_0}z^3$$
$$+ \frac{5{q_0}^3+6{q_0}^2+6q_0+8}{8H_0}z^4 + \cdots , \quad (4.39)$$

respectively. Of course, the error for these series expansions has to be small, say for example 10^{-9}; we then need M_{RW} up to order 5, ϕ_{RW} up to order 2, $2E_{RW}$ up to order 4, r_{RW} up to order 3 and τ_{RW} up to order 3.

So far we have introduced how the DEs are discretised, and also shown how to obtain the data near the origin using series expansions of the RW expressions. For the main numerical integration, our approach was to start with a simple integration method, and move to a more sophisticated one if necessary. Therefore, initially an Euler method was used, which is only a first order integration method. However, persistent discrepancies later convinced us that a 2nd order Runge-Kutta method was necessary. Still, changing over to another integration method does not affect all the procedures we have gone through and the decisions that we have made. Naturally, with a higher order integration method the accuracy of our computer programmes [2] was improved and the comparisons between results obtained using an Euler's method and a 2nd order Runge-Kutta method will be shown later. Of course, one can still go for higher order Runge-Kutta method for the numerical integration, however, we will leave this for future development since we are not convinced that this is necessary, given the inevitable observational uncertainties.

4.5 Numerical comparison in the region before $\hat{R}_{max}$

We now test the numerical procedure, and evaluate the relative merits of the Euler and Runge-Kutta methods. To do this we need fake "observational data", for which we know the correct metric. We generated such fake data for various FLRW models using expressions (B.1) and (B.2) for $\hat{R}$ and $4\pi\hat{m}n$ given in the appendix. In order to avoid confusion, we call the H_0 and q_0 used for generating fake data q_{0d} and H_{0d}; and the ones our numerical procedure extracts from the data q_0 and H_0 from here on. We pick $q_{0d} = 0.45$ and $H_{0d} = 0.72$ [3] for the testing (see the next chapter for testing with a few different q_{0d} values used). Figures 4.4 and 4.5 are plots of $\hat{R}(z)$ and $4\pi\hat{m}n(z)$ against z where $z \in [0, 3]$. For the particular q_{0d} and H_{0d} values that we have chosen, $z_m \approx 1.295$; however, we will only do the testing till somewhere before z_m, say till $z = 1.2$.

[2] Matlab is the computer language that we use for our numerical work.

[3] We use the Geometric units throughout this thesis, see Appendix A for the correspondence between different unit systems.

As one can see from Figures 4.6 - 4.9, the curves we plotted from our numerics using the Euler method are already in quite good agreement with the ones from the RW relations in Appendix B with the exception that there is approximately 0.002 % difference between the two W curves toward the end. This is not too surprising though, as it is apparent from the DEs that W will be the least well-determined function. We are still able to further improve the accuracy of W by making the step size (and hence, also the bin size) smaller, see Figure 4.10. However, this is probably not necessary since, firstly, we cannot be sure whether the improvement is due to the better fake data generated with smaller bin size or due to the effect of less numerical error as we make the step size smaller. Secondly, we have no idea what the optimum bin size is, because up to now, no observational data have been used. With the real data, statistical fluctuations will increase if the bin size we use turns out to be too small. Thirdly, it won't be a difficult task if we decide to change the bin size later on when it's necessary. Hence, we are quite satisfied with the agreement between the curves for all functions r, ϕ, M and W (hence $2E$). Besides the above reasons, if one looks at Figure 4.11, the accuracy of the numerical output is better than in Figure 4.9, and this is not achieved by having a smaller bin size, but by using the second order Runge-Kutta method for the numerical integration. Therefore, we are certain that a smaller bin size is not required at this stage. Next, we can then deal with the problem of finding the connection points between the integration part and series expansion part.

Figure 4.4: Example of the fake data function $\hat{R}(z)$ generated with $H_{0d} = 0.72$, $q_{0d} = 0.45$ and $\delta z = 0.001$.

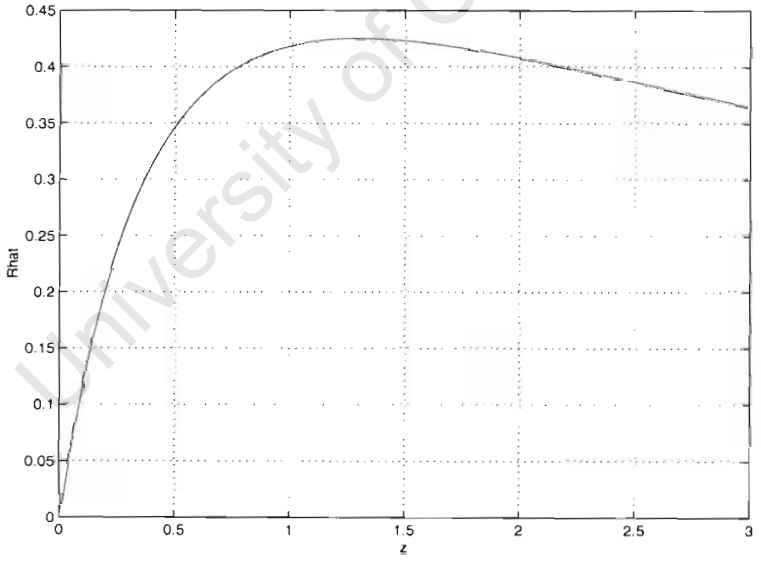

Figure 4.5: Example of the fake data function $4\pi\hat{m}n(z)$ generated with $H_{0d} = 0.72$, $q_{0d} = 0.45$ and $\delta z = 0.001$.

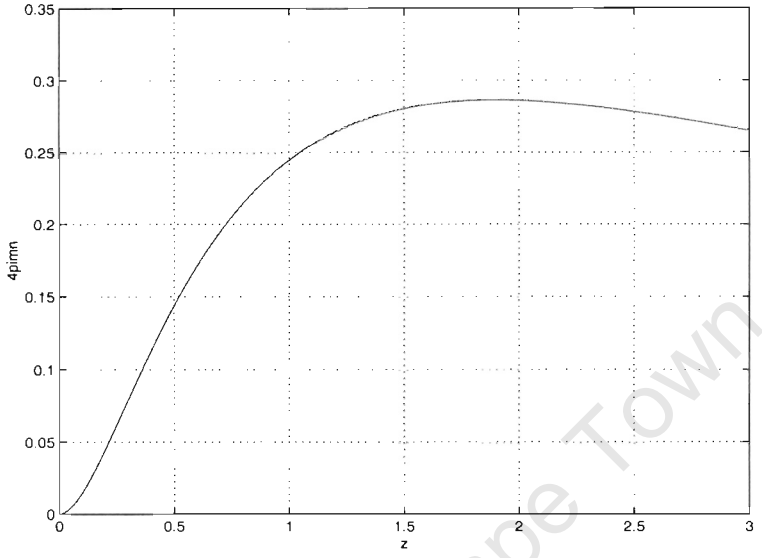

Figure 4.6: Results of r vs. z with $H_0 \approx 0.71999$, $q_0 \approx 0.450003$ and $\delta z = 0.001$ before reaching z_m. The correct RW curve is represented by solid grey and the dotted curve is our numerical output using the Euler method for numerical integration.

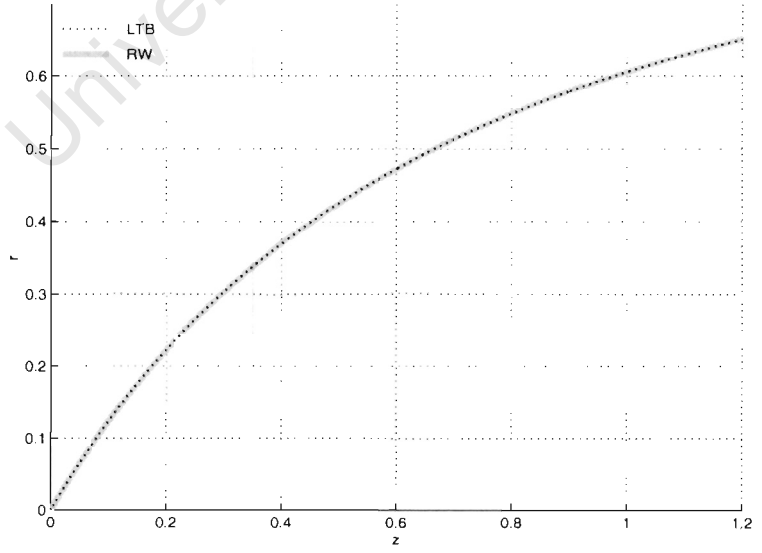

Figure 4.7: Results of ϕ vs. z with $H_0 \approx 0.71999$, $q_0 \approx 0.450003$ and $\delta z = 0.001$ before reaching z_m. The solid grey curve represents the correct RW values and the dotted curve is our numerical output using Euler method for numerical integration.

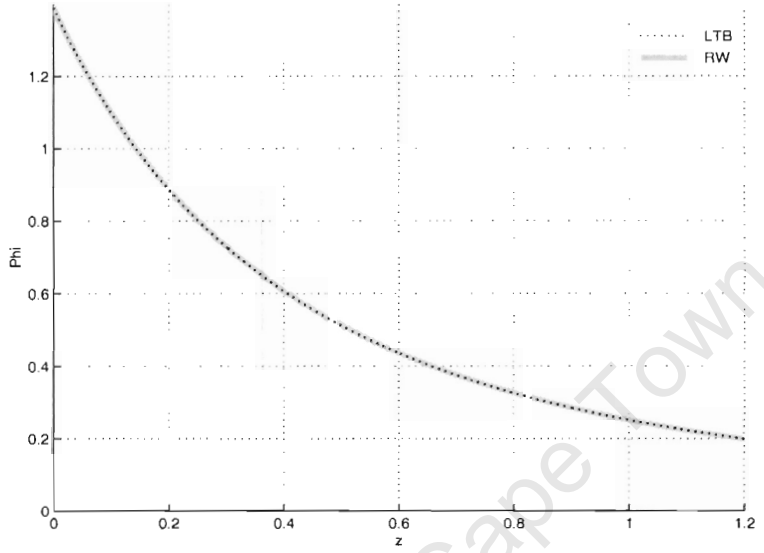

Figure 4.8: Results of M vs. z with $H_0 \approx 0.71999$, $q_0 \approx 0.450003$ and $\delta z = 0.001$ before reaching z_m. The solid grey curve is plotted from the correct RW expression and the dotted curve is our numerical output using Euler method for numerical integration.

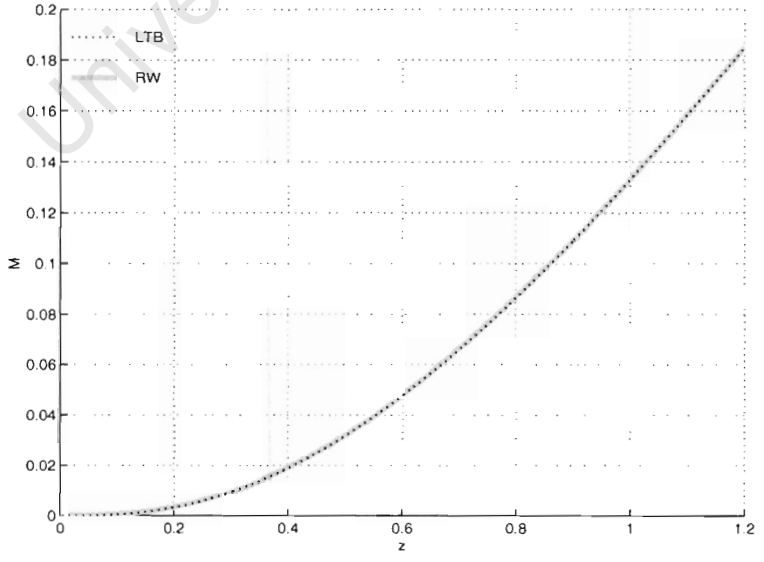

Figure 4.9: Results of W vs. z with $H_0 \approx 0.71999$, $q_0 \approx 0.450003$ and $\delta z = 0.001$ before reaching z_m. The solid grey curve is the correct RW expression and the dotted one is our numerical output using Euler method for numerical integration.

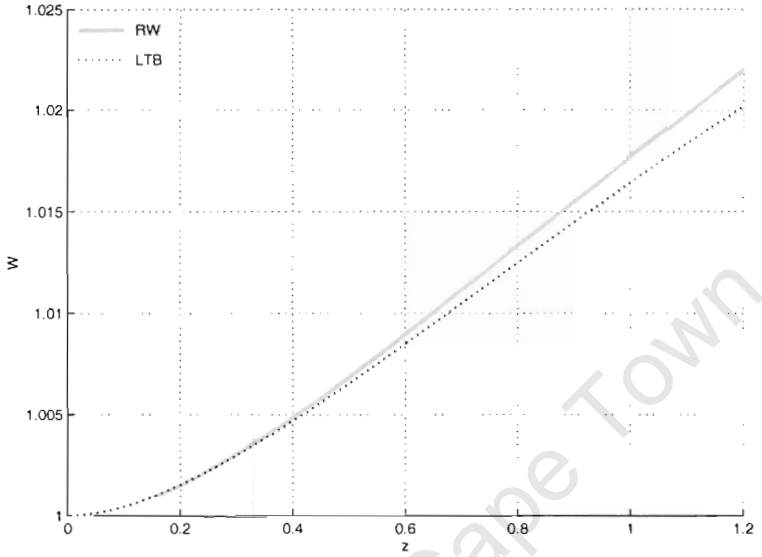

Figure 4.10: Results of W vs. z with $H_0 \approx 0.71999$, $q_0 \approx 0.450003$ and $\delta z = 0.0001$ before reaching z_m. The solid grey curve is plotted from the correct RW expression and the dotted curve is our numerical output using Euler method for numerical integration.

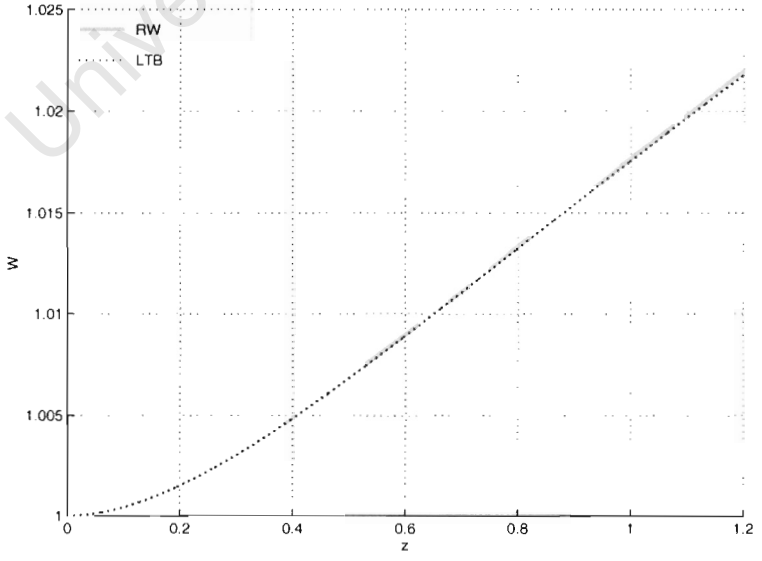

Figure 4.11: Results of W vs. z with $H_0 \approx 0.71999$, $q_0 \approx 0.450003$ and $\delta z = 0.001$ before reaching z_m. The solid grey curve is the correct RW expression and the dotted curve is our numerical output using Runge-Kutta method for numerical integration.

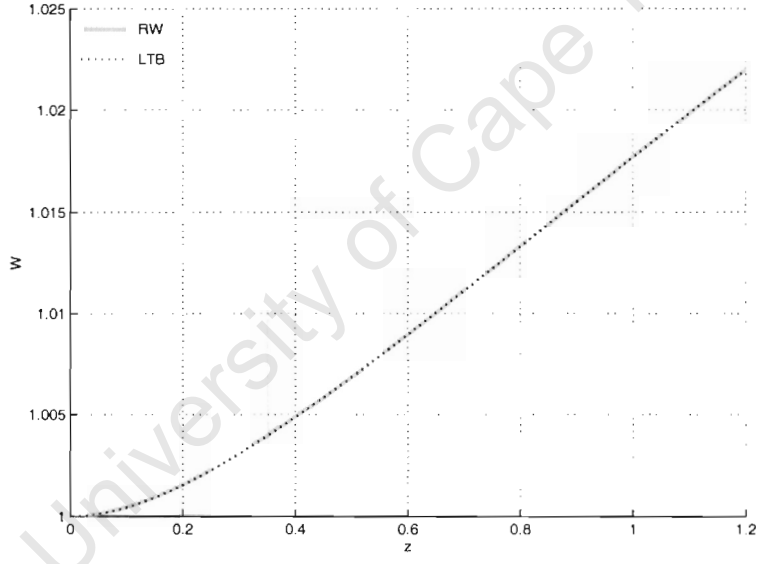

4.6 Connection between the Numerical integration and series expansion

Although we have a numerical method that can get us close to $\hat{R}_{max}$, and series expansions for all our functions that are able to carry our numerics through the maximum in $\hat{R}$, we still need to find the connecting point, z_a, between the numerical integration and the series expansion (see Figure 4.2). Also, there are still a few issues left unsolved from the previous sections. Firstly, we still don't know where z_a is in order to generate a value for M_1 using z_a and M_a. Secondly, should matching of M or of W be used at z_a in order to evaluate M_1? Thirdly, a value for r_0 can't be generated until we have made a decision on where to connect the series expansion to the integration part. Since each of the above mentioned problems can be sorted out very easily once we have found z_a, it is then essential to look at this primary problem first.

As mentioned before, all the coefficients for $\phi(z)$ can be determined from z_m and the coefficients of $\hat{R}(z)$ and $\hat{m}n(z)$ given in (4.9) and (4.10). A set of ϕ series expansion values can be generated from substituting a set of $dz = z - z_m$ values into (4.11); using Euler integration of the ϕ DE (4.6), we can generate another set of ϕ values for an overlapping z interval. We use the $\hat{R}$ and $\hat{m}n$ values of 361 redshift bins on either side of z_m (this is a redshift interval of 0.361), and perform a least squares fit with these data to obtain all the coefficients for $\hat{R}$ and $\hat{m}n$, and hence, obtain all coefficients for ϕ. When plotted on the same graph, we see there is good agreement between the numerical and series values, over a range of z values, and we notice there is one intersection point between the two curves before z_m as one can see from Figures 4.14 and 4.15. The former is the zoom in of Figure 4.12, with the ϕ series going up to 2nd order; and the latter is the zoom in graph of Figure 4.13, with the ϕ series going up to order 3. The intersection points here are of great importance since they are where we have matching values between series expansion and Euler integration for ϕ, and they can potentially become the connecting points for the Euler integration and series expansion.

The improvement of the overall matching going from a 2nd to a 3rd order series is clearly noticeable if one compares Figure 4.13 with Figure 4.12. Given the likely observational and numerical error, an order higher than what we have here seems unnecessary. If necessary at a later stage, we will go for higher order series expansions. One more thing we should mention is that when we perform the least squares fit with data near $\hat{R}_{max}$, we also tried to improve our series expansion of ϕ and M curves by using different number of bins of $\hat{R}$ and $\hat{m}n$ values for evaluating the coefficients. However, this turned out to make very little difference because, as we can see from Figure 4.4, $\hat{R}(z)$ is fairly flat near $\hat{R}_{max}$ and $\hat{m}n$ is increasing steadily around z_m (see Figure 4.5). We used 361 bins since it covers about 12 percent of the total redshift interval that we are considering here.

We have mentioned before that the ϕ DE is independent of r, M and W. This means that we can use ϕ to decide on the intersection point z_a since this is where the ϕ value from the numerical integration part and from the series expansion coincide. Having decided on this, however, there is still one practical concern, which is that all our data points are plotted at discrete positions, and there may be more than one intersection point between the numerical and series curves for ϕ. Therefore, we have programmed our code in such a way that it will only pick the intersection point which is before and also closest to z_m.

Now we know where z_a is, one can get M_1 from z_a and M_a if we substitute them into

equation (4.12)

$$M_a = M_0 + M_1(z_a - z_m) + M_2(z_a - z_m)^2 + M_3(z_a - z_m)^3 + \cdots \ . \tag{4.40}$$

where M_2 and M_3 are given by (4.18) and (4.19). Similarly, if we are matching the W values

$$W_a = W_0 + W_1(z_a - z_m) + W_2(z_a - z_m)^2 + \cdots \ , \tag{4.41}$$

where W_1 and W_2 are given by (4.25) and (4.26). Having decided on the order of the series expansions of our functions, M_1 can easily be calculated. Therefore, if we match M then

$$\begin{aligned} M_1 = \Bigg\{ & \frac{M_a - M_0}{z_a - z_m} + \frac{8\pi^2(\hat{m}n)_0{}^2}{\hat{R}_{max}} (z_a - z_m) + \frac{R_2}{2} (z_a - z_m) \\ & + \left(\frac{R_2}{1 + z_m} + \frac{(\hat{m}n)_1 R_2}{(\hat{m}n)_0} + R_3 \right) \frac{(z_a - z_m)^2}{4} \\ & + \frac{8\pi^2(\hat{m}n)_0(\hat{m}n)_1}{\hat{R}_{max}} (z_a - z_m)^2 \Bigg\} \Bigg/ \Bigg\{ 1 + \left(\frac{1}{1 + z_m} + \frac{(\hat{m}n)_1}{(\hat{m}n)_0} \right) \frac{z_a - z_m}{2} \\ & + \left(\frac{(\hat{m}n)_2}{3(\hat{m}n)_0} + \frac{(\hat{m}n)_1}{3(\hat{m}n)_0(1 + z_m)} - \frac{R_2}{3\hat{R}_{max}} \right) (z_a - z_m)^2 \Bigg\} \ . \end{aligned} \tag{4.42}$$

Alternatively, if W is used for the matching, we have

$$\begin{aligned} M_1 = \Bigg\{ & W_a + \frac{R_2}{4\pi(\hat{m}n)_0} (z_a - z_m) + \frac{4\pi(\hat{m}n)_0}{\hat{R}_{max}} (z_a - z_m) + \frac{3R_3}{16\pi(\hat{m}n)_0} (z_a - z_m)^2 \\ & - \frac{(\hat{m}n)_1 R_2}{16\pi(\hat{m}n)_0{}^2} (z_a - z_m)^2 + \frac{3R_2}{16\pi(\hat{m}n)_0(1 + z_m)} (z_a - z_m)^2 \\ & + \frac{2\pi(\hat{m}n)_1}{\hat{R}_{max}} (z_a - z_m)^2 \Bigg\} \Bigg/ \Bigg\{ \frac{1}{4\pi(\hat{m}n)_0} + \frac{z_a - z_m}{4\pi(\hat{m}n)_0(1 + z_m)} - \frac{R_2(z_a - z_m)^2}{4\pi(\hat{m}n)_0\hat{R}_{max}} \Bigg\} \ . \end{aligned} \tag{4.43}$$

All our functions should connect the integration part and series expansion part at z_a; and from z_a, we can generate the corresponding r_a and M_a easily. Using (4.42) or (4.43), a value for M_1 can easily be determined, however, we use (4.42) first and will make suitable adjustments later on when needed. Since we also know r_a and z_a, and all ϕ coefficients can be evaluated without difficulty, a value for r_0 can be solved from (4.27).

The purpose for doing a series expansion is to extend our numerics through $\hat{R}_{max}$. Of course, once this is achieved, we need to switch back to numerical integration again. It is sensible if we connect at z_J where $z_m - z_a = z_J - z_m$. Since we need an initial value for r, ϕ and M in order to start the second part of the numerical integration, we use their series expansion values at z_J and this means that we are matching their values at this point.

From the particular q_{0d} and H_{0d} we chose for generating fake data of Figures 4.4 and 4.5, and using Euler method for numerical integration, the two connecting points happen to be at $z_a = 0.9195$ and $z_J = 1.6675$. After we have the complete set of values from all three parts for r, ϕ, M and W, we plot them as well as the correct curves generated from the RW relations on the same axes for comparison, as shown in Figures 4.16-4.19. The r, ϕ and M curves show good agreement between the correct RW curves and the curves from our numerical output, but, the W curve has jumps at the two connecting points. We have

anticipated this situation in the previous section already. So next we try matching W at both connecting points to see if it gives better results.

If we look at Figure 4.20, the two M curves are similarly well-matched as in Figure 4.18. However, in Figure 4.21, although we are rid of the two jumps in the numerical W curve, we also reduce the accuracy of our W series expansion. Since the series expansion is what we use in order to extend our numerics through $\hat{R}_{max}$, we would like it to have a better accuracy. A key fact is that, at z_m we actually know the value of M from (4.16) if we know $\hat{R}_{max}$. In order to maximise the accuracy of our series expansion and minimise the jumps that appear in our W graph, we decided to match M at the first connecting point, and match W at the second one.

We can see from Figure 4.22 that this approach does not leave any visible alteration in the M curve if compared with Figure 4.18. As shown in Figure 4.23, we now have the jump in W at the first connecting point and better accuracy for our series expansion, but the second jump is no longer there. Although we might still improve the accuracy for W further by using a smaller step size, as discussed before, it's not practical. One more thing worth mentioning here is that we may need to shorten the z interval for the series expansion, since with inhomogeneous data, fluctuations will be present, so if the interval is too wide compared with the fluctuations, the accuracy for our series expansion will be lower. However, this problem will only be dealt with when it has shown a significant effect on the numerics.

In Figures 4.22 and 4.23, although the accuracy for generated numerical outputs is quite good even for the W function, only the Euler integration was used. Once we change to the second order Runge-Kutta as our numerical integration method, we can actually improve the accuracy for the numerical output of our W curve further. The comparisons between the correct RW curves and the numerical outputs for M and W can be found in Figures 4.24 and 4.25 with M used for the first connecting point and W used for the second as decided from the Euler method. Note that there isn't much difference between the Euler and Runge-Kutta results for M if one compares Figure 4.24 to Figure 4.22, however, the W curves are in better agreement with each other in the Runge-Kutta case if one compares Figure 4.25 with Figure 4.23. Although we initially used Euler integration for all the decisions we made about the numerical to series matching, the same reasonings apply to the Runge-Kutta method also. Given that no matter which integration method we use, one still faces the same problem of degenerate DEs as we approach the point $\hat{R}_{max}$, a series expansion is definitely needed in order to carry the numerics through this point.

4.7 Time calculations

After completing the integration of r, ϕ, M and E we now need to determine τ and thence t_B, and check if they are in good agreement with the correct RW expressions. At each discrete position, we are required to determine, numerically, which type of evolution we have: hyperbolic, elliptic and near-parabolic. As one might have noticed from equation (3.20), the near parabolic expansion is in powers of $\hat{R}f/M$, and this factor can be evaluated at each discrete position since we know the values for $\hat{R}$, E and M. Of course, the error for this approximation of the series expansion for τ has to be small, say about 10^{-7}; if we take (3.20) up to order 3, this will then give us $\frac{\hat{R}f}{M} \approx 0.1$. Hence, if $\frac{\hat{R}f}{M} > 0.1$, we have a hyperbolic case; if $0 < \frac{\hat{R}f}{M} < 0.1$, we then have a hyperbolic near-parabolic case. Similarly, if $\frac{\hat{R}f}{M} < -0.1$, we have an elliptic case; if $0 > \frac{\hat{R}f}{M} > -0.1$, we then have an

elliptic near-parabolic case. Since $f = 2E$ for all values of E, we will then combine the two near-parabolic cases into one. Hence, besides the hyperbolic and elliptic cases, we have $-0.1 < \frac{\hat{R}f}{M} < 0.1$ for the third case · · the near-parabolic case.

Since the accuracy of the numerical output generated from the second order Runge-Kutta method and the Euler method is more or less the same for the τ and t_B graphs if one compares with the correct RW ones, we only show the ones that used the Runge-Kutta method, as can be found in Figures 4.26 and 4.27. There are three curves in the t_B graph, the thick grey curve is plotted from the correct RW expression, the dotted black curve is plotted from our numerics and the solid black curve represents the current age of the universe according to the model we have chosen.

We are quite satisfied with the accuracy and the ability of our numerical method in reproducing this particular homogeneous data. In the next chapter, we look at a few other RW cases to see if we can still get a similar accuracy level to that obtained above; then we test our code with some inhomogeneous models in chapter 6.

Figure 4.12: ϕ vs. z with $H_0 \approx 0.71999$, $q_0 \approx 0.450003$ and $\delta z = 0.001$. The solid curve represents values from the series expansion (up to order 2) and the dotted curve represents values from Euler integration.

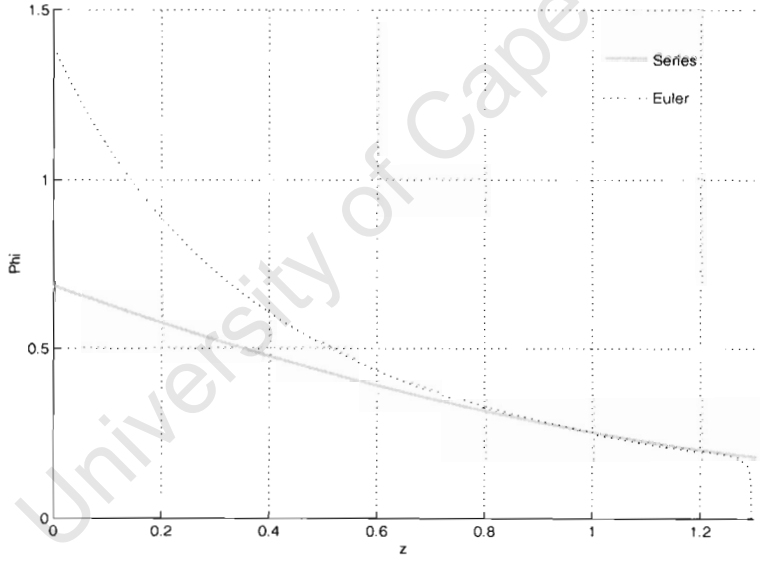

Figure 4.13: ϕ vs. z with $H_0 \approx 0.71999$, $q_0 \approx 0.450003$ and $\delta z = 0.001$.The solid curve represents values from the series expansion (up to order 3) and the dotted curve represents values from Euler integration.

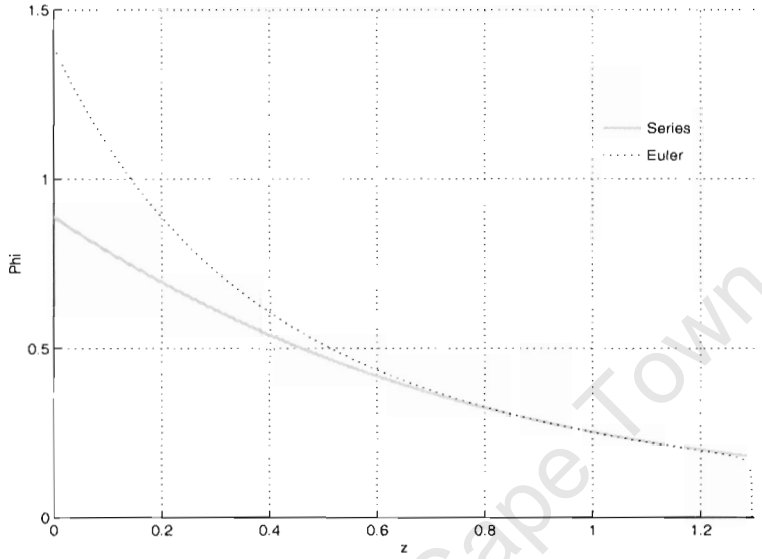

Figure 4.14: This is the zoom in of Figure 4.12. The solid curve represents values from the series expansion (up to order 2) and the dotted curve represents values from Euler integration.

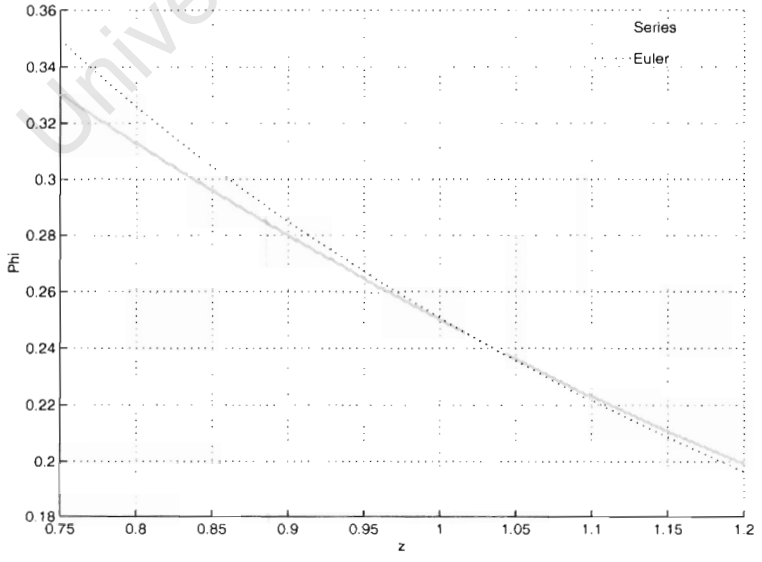

Figure 4.15: This is the zoom in of Figure 4.13. The solid curve represents values from the series expansion (up to order 3) and the dotted curve represents values from Euler integration.

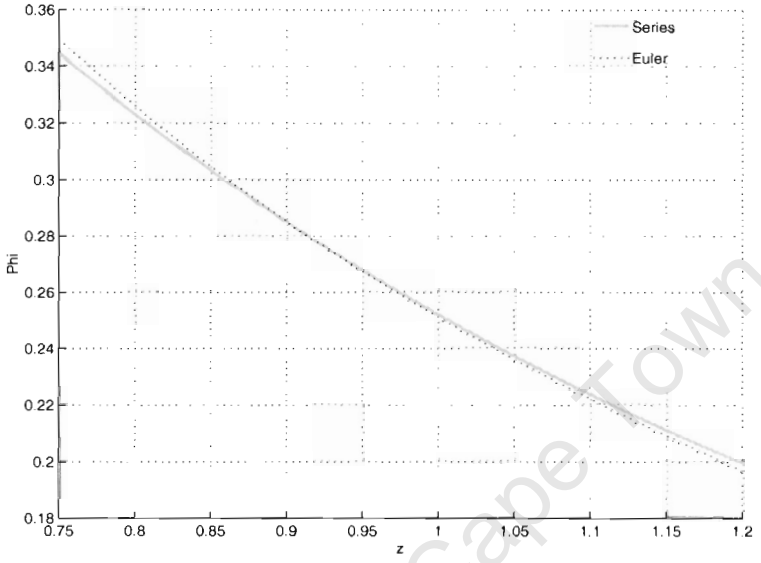

Figure 4.16: Results of r vs. z with $H_0 \approx 0.71999$, $q_0 \approx 0.450003$ and $\delta z = 0.001$. The grey curve is the correct RW expression and the dotted curve is our numerical output using Euler method for numerical integration.

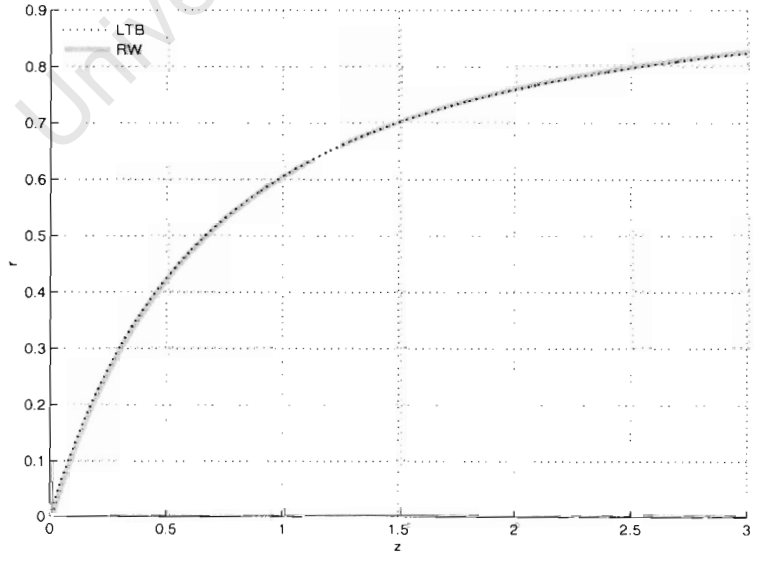

Figure 4.17: Results of ϕ vs. z with $H_0 \approx 0.71999$, $q_0 \approx 0.450003$ and $\delta z = 0.001$. The grey curve is the correct RW expression and the dotted curve is our numerical output using Euler method for numerical integration.

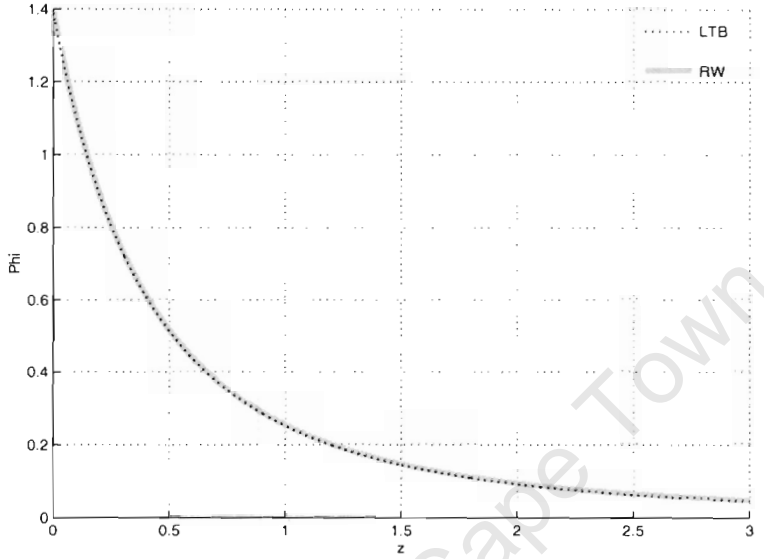

Figure 4.18: Results of M vs. z with $H_0 \approx 0.71999$, $q_0 \approx 0.450003$ and $\delta z = 0.001$, after matching M values at both of our connecting points. The grey curve is the correct RW expression and the dotted black one is our numerical output using Euler method for numerical integration.

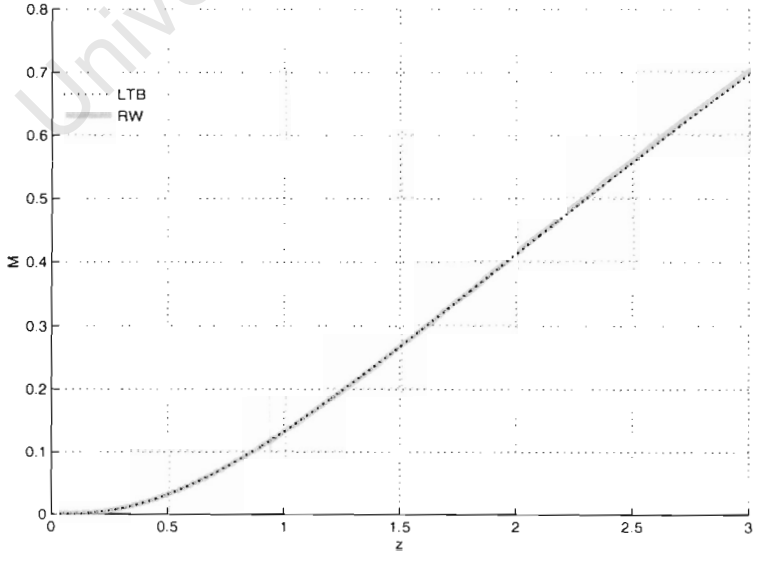

Figure 4.19: Results of W vs. z with $H_0 \approx 0.71999$, $q_0 \approx 0.450003$ and $\delta z = 0.001$, after matching M values at both of our connecting points. The solid curve is the correct RW expression and the dotted curve is our numerical output using Euler method for numerical integration.

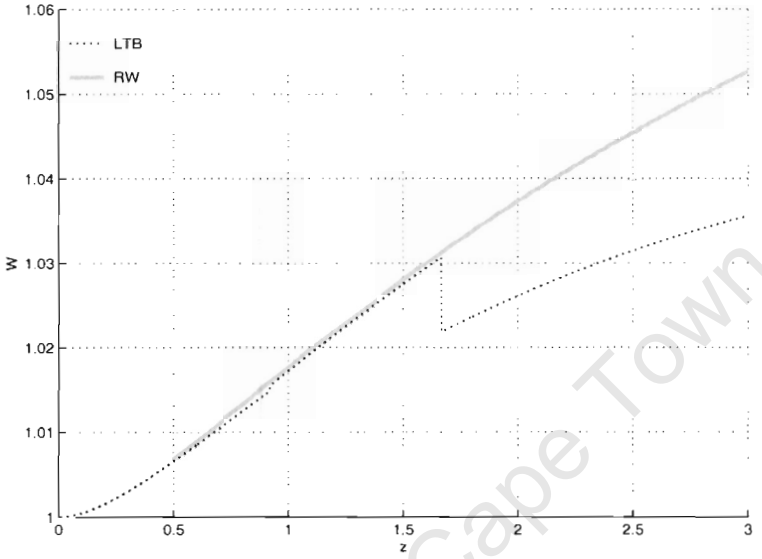

Figure 4.20: Results of M vs. z with $H_0 \approx 0.71999$, $q_0 \approx 0.450003$ and $\delta z = 0.001$, after matching W values at both of our connecting points. The solid curve is the correct RW expression and the dotted black one is our numerical output using Euler method for numerical integration.

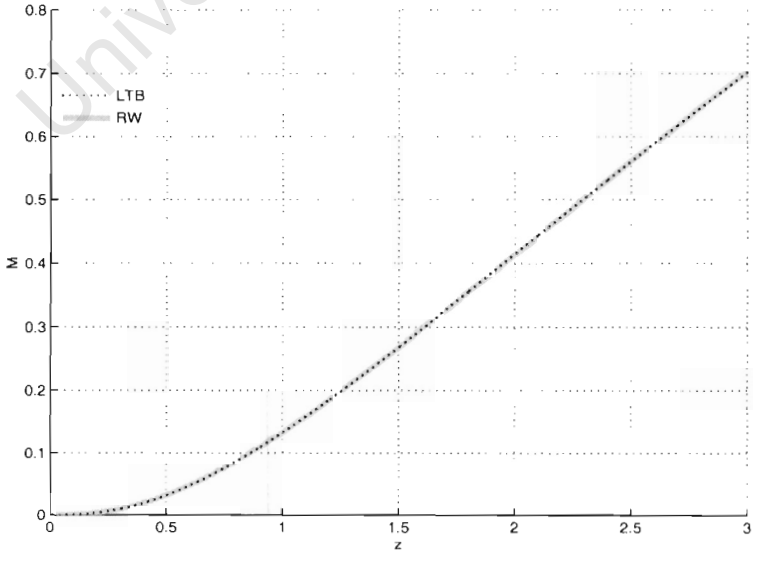

Figure 4.21: Results of W vs. z with $H_0 \approx 0.71999$, $q_0 \approx 0.450003$ and $\delta z = 0.001$, after matching W values at both of our connection points. The solid grey curve is the correct RW expression and the dotted one is our numerical output using Euler method for numerical integration.

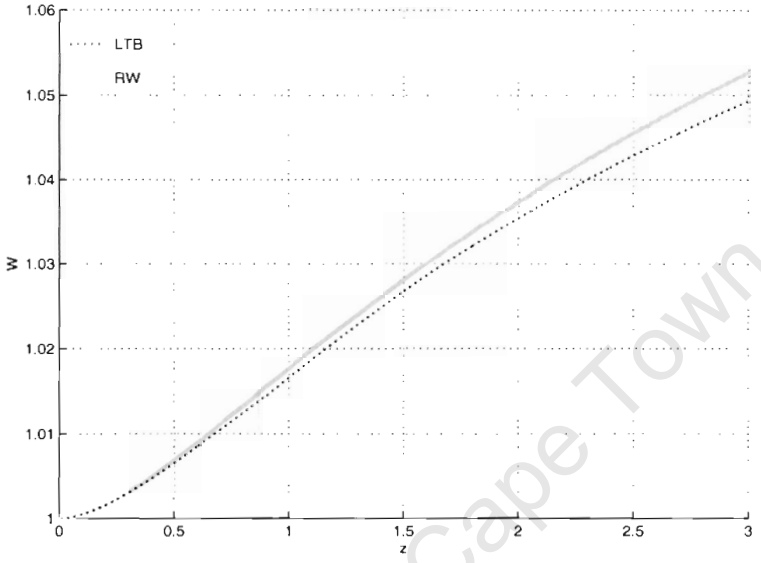

Figure 4.22: Results of M vs. z with $H_0 \approx 0.71999$, $q_0 \approx 0.450003$ and $\delta z = 0.001$, after matching M value at the first connection point and W value at the second connection point. The grey curve is the correct RW expression and the dotted black one is our numerical output using Euler method for numerical integration.

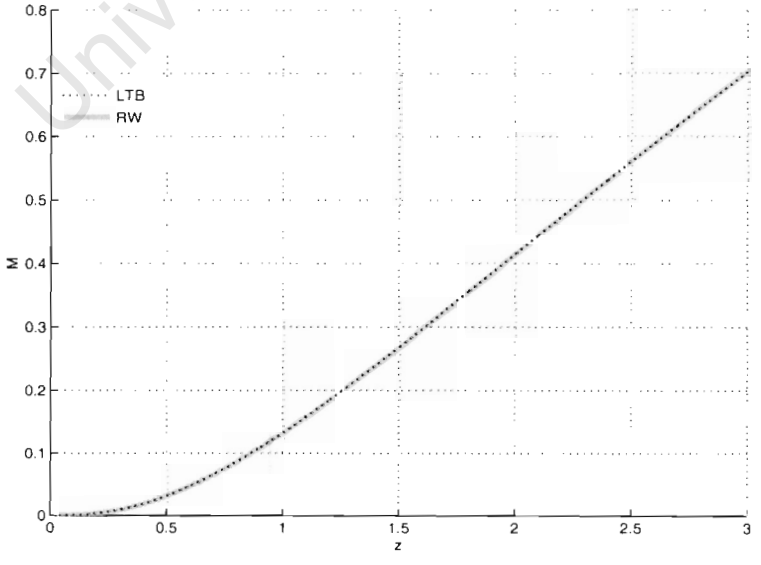

Figure 4.23: Results of W vs. z with $H_0 \approx 0.71999$, $q_0 \approx 0.450003$ and $\delta z = 0.001$, after matching M value at the first connection point and W value at the second connection point. The solid grey curve is the correct RW expression and the dotted grey is our numerical output using Euler method for numerical integration.

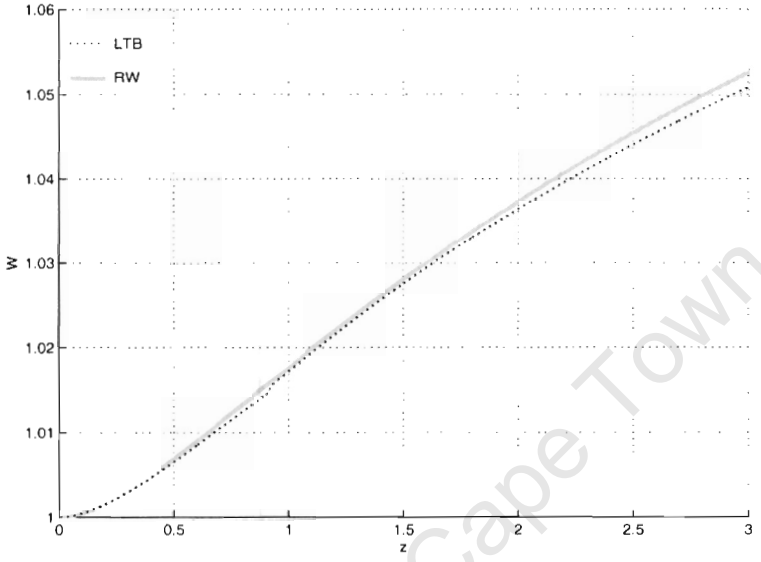

Figure 4.24: Results of M vs. z with $H_0 \approx 0.71999$, $q_0 \approx 0.450003$ and $\delta z = 0.001$, after matching M value at the first connection point and W value at the second connection point. The grey curve is the correct RW expression and the dotted black one is our numerical output using Runge-Kutta as the integration method.

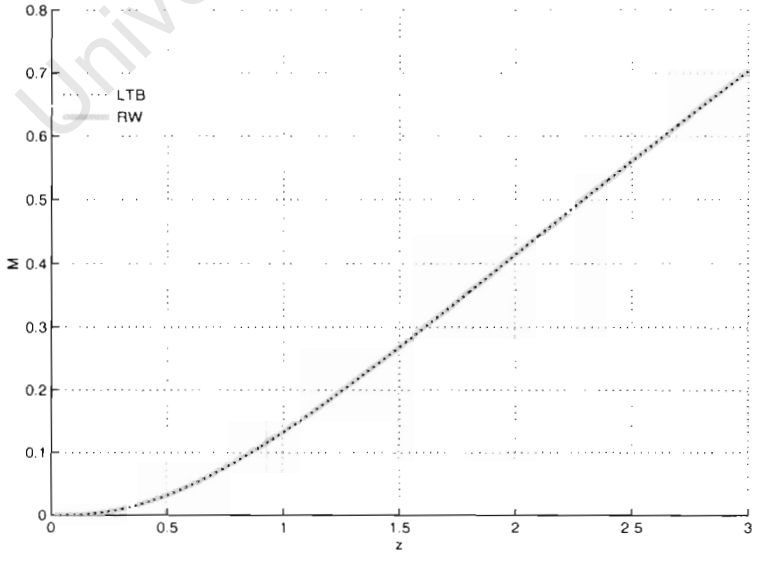

Figure 4.25: Results of W vs. z with $H_0 \approx 0.71999$, $q_0 \approx 0.450003$ and $\delta z = 0.001$, after matching M value at the first connection point and W value at the second connection point. The solid curve is the correct RW expression and the dotted curve is our numerical output using Runge-Kutta as the integration method.

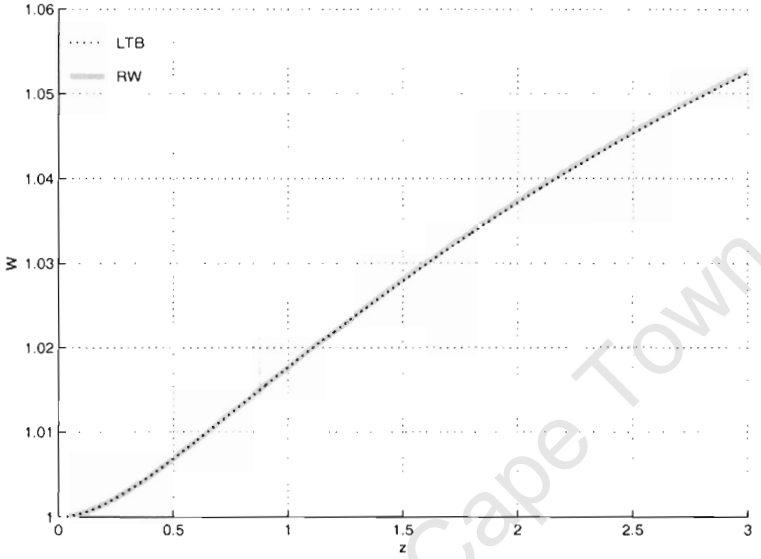

Figure 4.26: Results of τ vs. z with $H_0 \approx 0.71999$, $q_0 \approx 0.450003$ and $\delta z = 0.001$. The grey curve is the correct RW expression and the dotted black one is our numerical output using Runge-Kutta as the integration method.

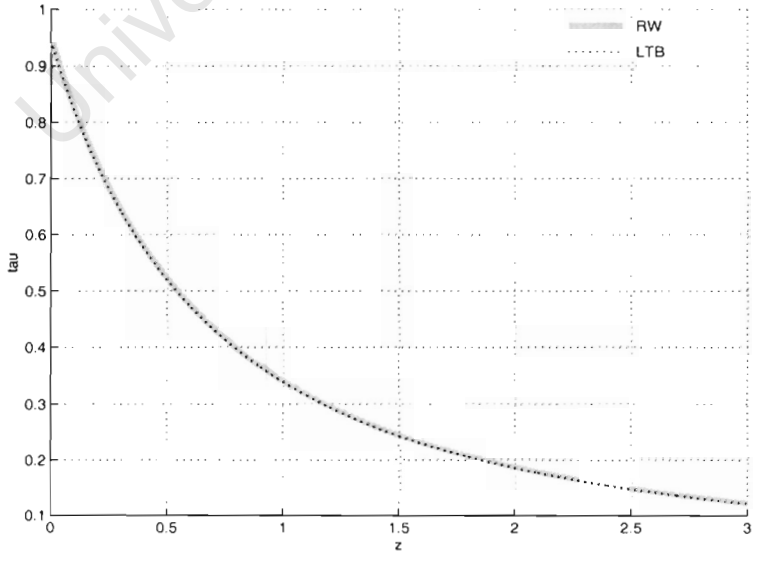

Figure 4.27: Results of t_B vs. z with $H_0 \approx 0.71999$, $q_0 \approx 0.450003$ and $\delta z = 0.001$. The solid grey curve is the correct RW expression and the dotted curve is our numerical output using Runge-Kutta as the integration method. The solid black line on the top is the current age of the universe according to the model we choose.

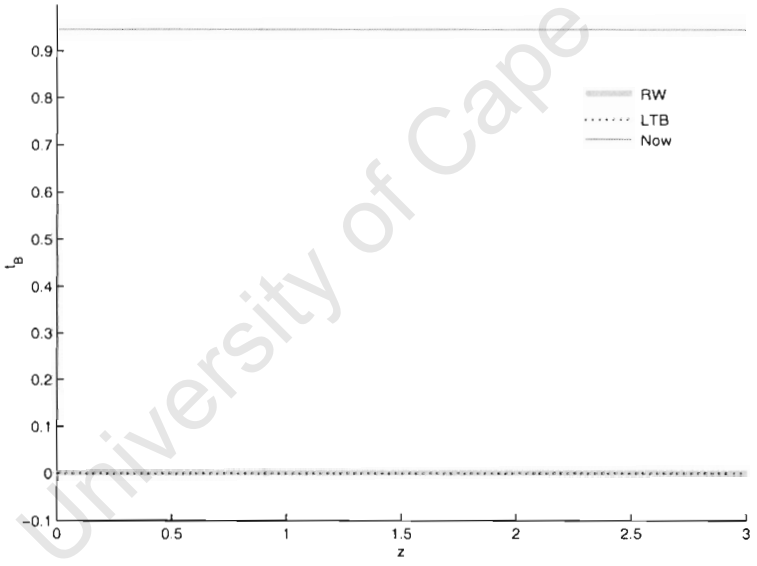

Chapter 5

Testing the numerics with homogeneous models

In the previous chapter, we used $q_{0d} = 0.45$ and $H_{0d} = 0.72$ to generate fake data for one RW case in order to develop our numerical method, test its accuracy and see how it turns out in practice. So far, it works quite well and its accuracy is satisfactory. Now we begin more serious testing, and we here use input data generated from a variety of RW models, to verify our programme is also able to handle data from any homogeneous model. After doing this, we will proceed to further testing with data from a number of inhomogeneous models in the next chapter.

Some of the homogeneous cases below are the "boundary" cases since the q_0 values we use are very close to $q_0 = 1/2$, i.e. the near-parabolic case. We are expecting to have slightly lower accuracy in our numerics when it is near $q_0 = 1/2$. Although we cannot test every single possible case here, if we can get our numerics with the boundary cases to be in good agreement with the correct RW ones, then we can be quite certain that our code will work for other untested cases also. We note that, with real data, there will be considerable observational uncertainties, especially in the number counts. Consequently, our numerical error only needs to be distinctly less than observational error. In this chapter, we consider 2 near-parabolic cases and 2 far from parabolic cases, covering one $k = +1$ and one $k = -1$ example in each pair.

5.1 Homogeneous model with $q_{0d} = 0.49$ and $H_{0d} = 0.72$

This is the case when we still have a negatively curved universe, but very close to the flat case. Since, as we saw, W is the variable which accumulates most numerical error, and r, ϕ and M all have good accuracy, it also shows most clearly the improvement when we change from a Euler to a Runga-Kutta method.

In Figures 5.1-5.3, the curves plotted from our numerical output using the Runge-Kutta method and the ones from the generated RW data are in very good agreement with each other. Note that we are only showing the results obtained from the Runge-Kutta method for r, ϕ and M graphs since with these three functions, we were able to obtain satisfactory accuracy when compared with the correct RW curves even with the Euler method. Figure 5.4 is the W graph for which the Euler method is used and Figure 5.5 is the one that uses the Runge-Kutta method. In Figure 5.4, the numerical error tends to get bigger as z gets bigger, there is about 0.2312 % difference between the two curves. However, there is only

0.02106 % difference between the curves in Figure 5.5. If one looks at the two graphs only, the improvement is clearly visible. As pointed out in the previous chapter, there is a jump in Figure 5.5 at z_a, although it is barely visible. And this justifies the earlier decisions to match first M and then W at the two connections between the integration parts and the series expansion part.

If one looks at the τ curves in Figure 5.6, the two curves coincide with each other, which is not surprising since we already obtained high accuracy when the Euler method was used. As for t_B in Figure 5.7, the two curves that coincide show our numerical output to the RW value; and this is where the big bang occurred. The third curve, which is above the other two, is the current age of the universe according to the particular homogeneous model we have chosen for generating the fake data.

Figure 5.1: Results of r vs. z with $H_0 \approx 0.71999$, $q_0 \approx 0.490004$ and $\delta z = 0.001$. The grey curve is the correct RW expression and the dotted black one is our numerical output using Runge-Kutta as the integration method.

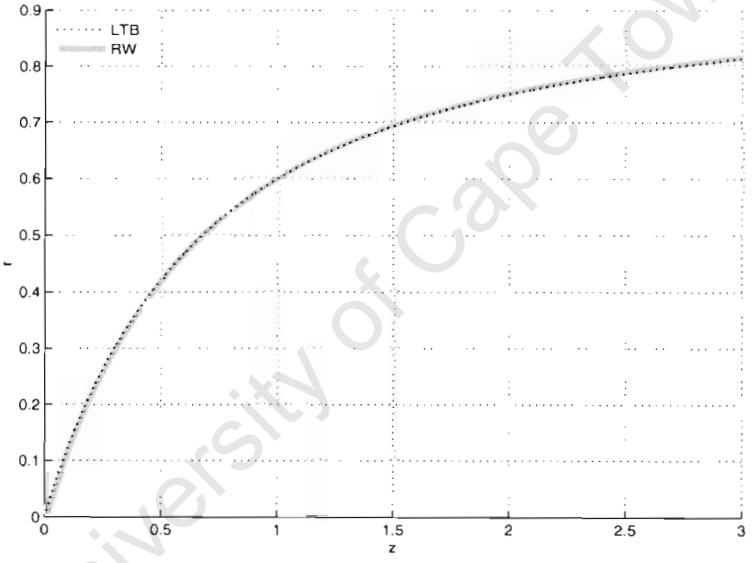

Figure 5.2: Results of ϕ vs. z with $H_0 \approx 0.71999$, $q_0 \approx 0.490004$ and $\delta z = 0.001$. The grey curve is the correct RW expression and the dotted black one is our numerical output using Runge-Kutta as the integration method.

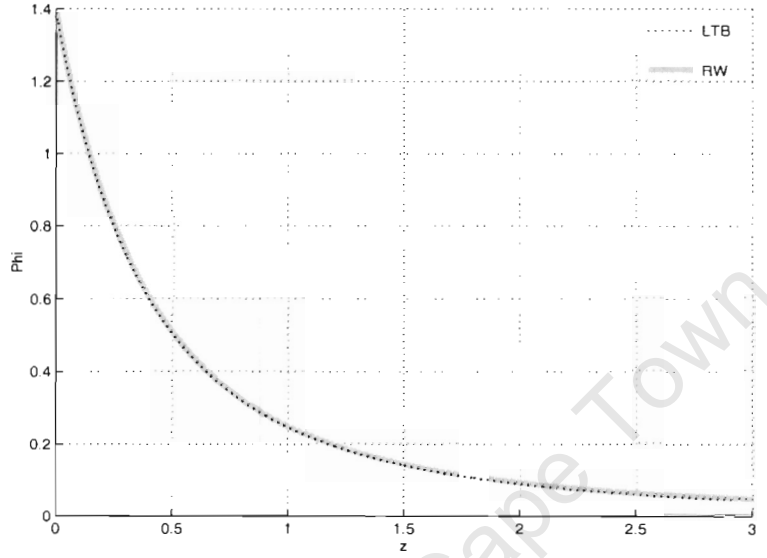

Figure 5.3: Results of M vs. z with $H_0 \approx 0.71999$, $q_0 \approx 0.490004$ and $\delta z = 0.001$. Matching the M values at the first connection point and the W values at the second connection point. The solid grey curve is the correct RW expression and the dotted black one is our numerical output using Runge-Kutta as the integration method.

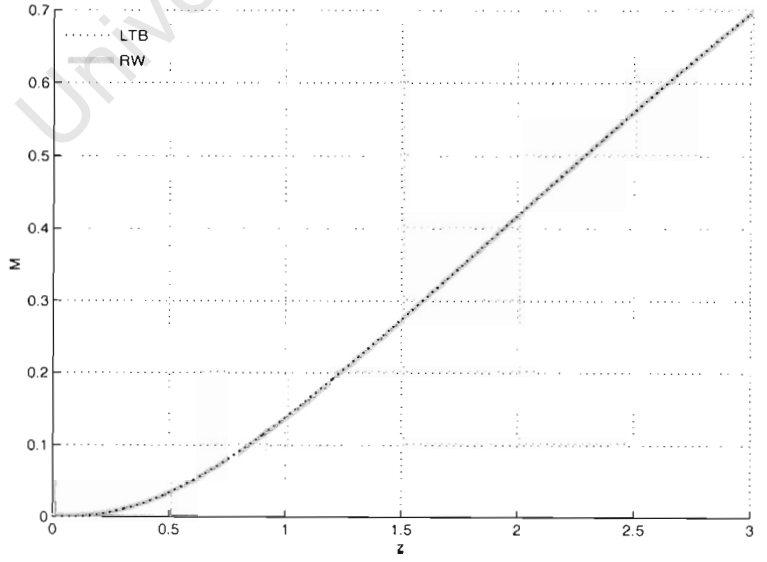

Figure 5.4: Results of W vs. z with $H_0 \approx 0.71999$, $q_0 \approx 0.490004$ and $\delta z = 0.001$. Matching the M values at the first connection point and the W values at the second connection point. The solid grey curve is the correct RW expression and the dotted one is our numerical output using Euler integration as the integration method.

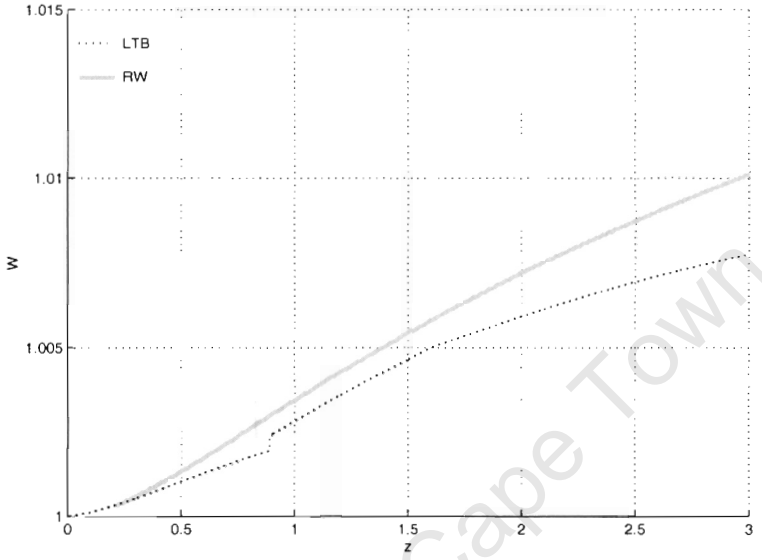

Figure 5.5: Results of W vs. z with $H_0 \approx 0.71999$, $q_0 \approx 0.490004$ and $\delta z = 0.001$. Matching the M values at the first connection point and the W values at the second connection point. The solid curve is the correct RW expression and the dotted one is our numerical output using Runge-Kutta as the integration method.

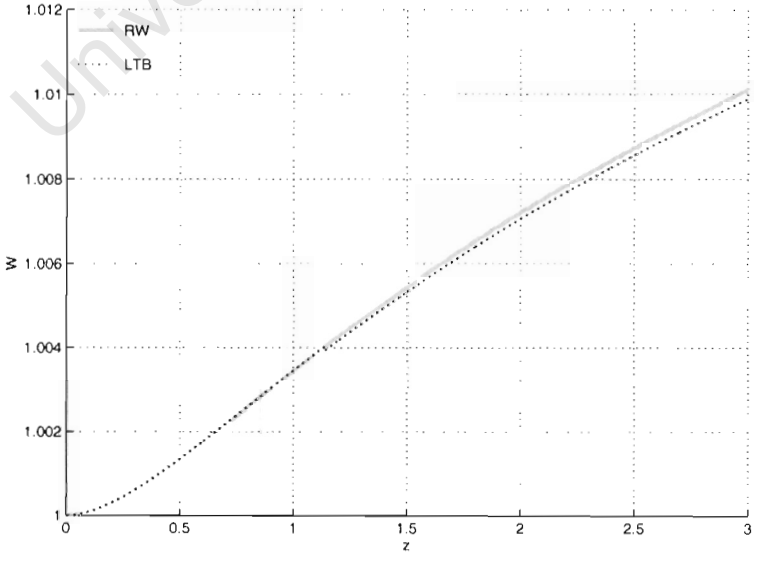

Figure 5.6: Results of τ vs. z with $H_0 \approx 0.71999$, $q_0 \approx 0.490004$ and $\delta z = 0.001$. The solid grey curve is the correct RW expression and the dotted black one is our numerical output using Runge-Kutta as the integration method.

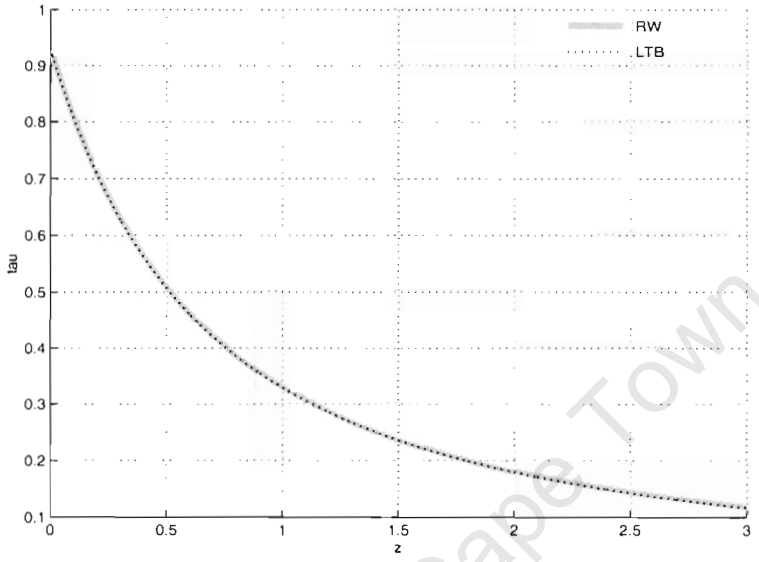

Figure 5.7: Results of t_B vs. z with with $H_0 \approx 0.71999$, $q_0 \approx 0.490004$ and $\delta z = 0.001$. The thick solid grey curve is the correct RW expression and the dotted black one is our numerical output using Runge-Kutta as the integration method. The solid black line on the top is the current age of the universe.

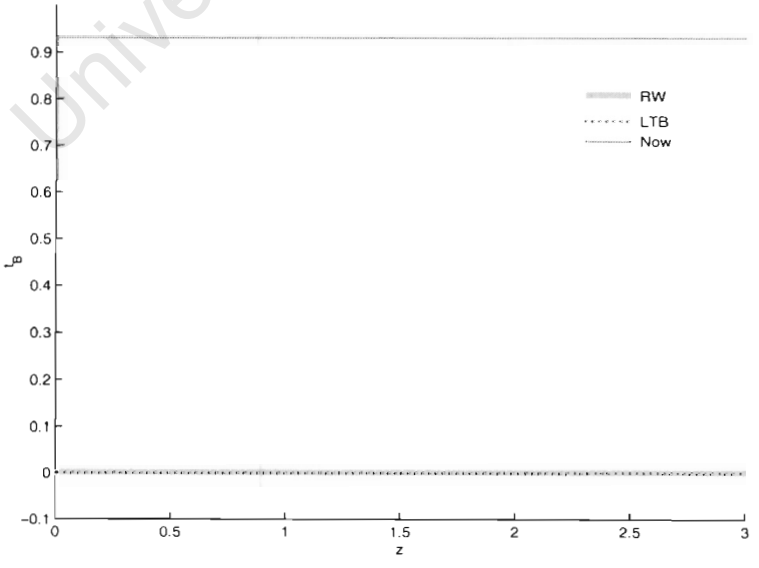

5.2 Homogeneous model with $q_{0d} = 0.51$ and $H_{0d} = 0.72$

This is the case when we have a positively curved universe, but close to being flat. There is nothing unexpected from the r, ϕ and M graphs (see Figures 5.8-5.10). If one looks at Figure 5.11, which uses the Euler integration method, as z gets bigger, the numerical W curve tends to move away from the correct RW curve, reaching about 0.2659 % difference at $z = 3$. However, there is only 0.02256 % difference using the second order Runge-Kutta method, as shown in Figure 5.12. Again, we demonstrate the need to change over to the Runge-Kutta method. Although the jump in the W graph still exists, as shown in Figure 5.12, it is less evident than the one shown in Figure 5.11.

If one looks at Figure 5.13, the two τ curves are again in good agreement with each other. As for Figure 5.14, the t_B and t_0 curves are as expected.

Figure 5.8: Results of r vs. z with $H_0 \approx 0.71999$, $q_0 \approx 0.510004$ and $\delta z = 0.001$. The grey curve is the correct RW expression and the dotted curve is our numerical output using Runge-Kutta as the integration method.

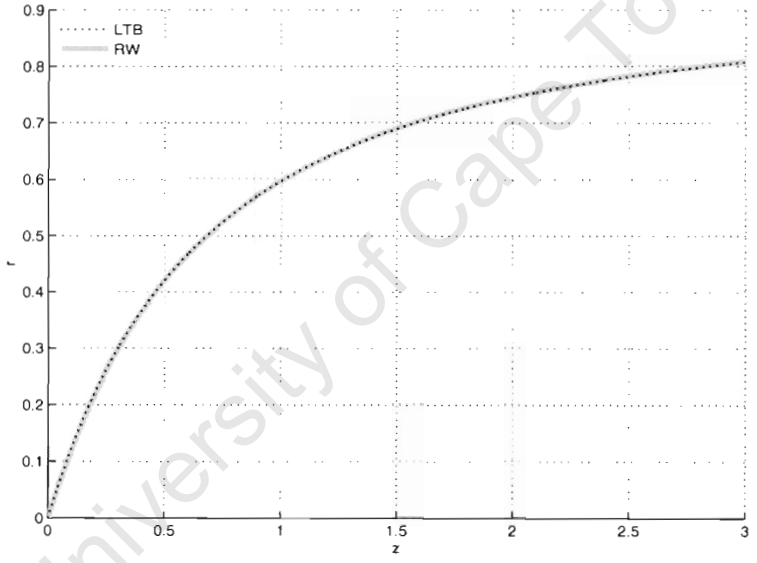

Figure 5.9: Results of ϕ vs. z with $H_0 \approx 0.71999$, $q_0 \approx 0.510004$ and $\delta z = 0.001$. The grey curve is the correct RW expression and the dotted curve is our numerical output using Runge-Kutta as the integration method.

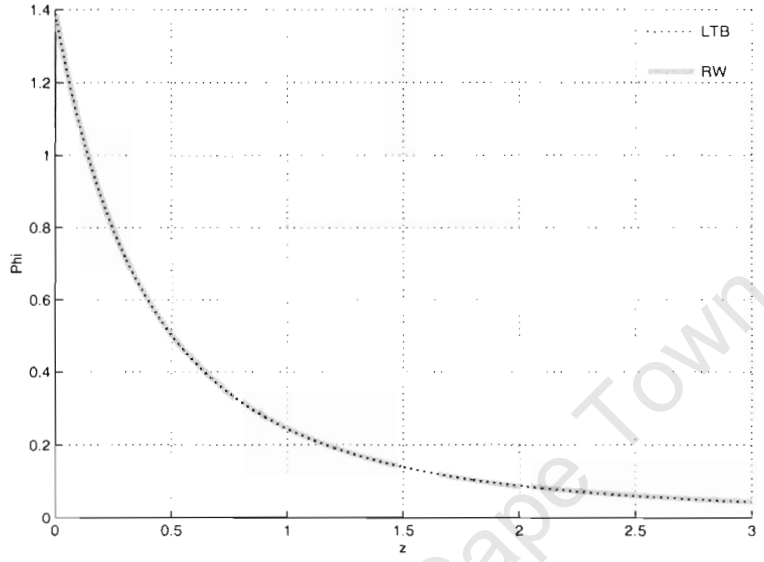

Figure 5.10: Results of M vs. z with $H_0 \approx 0.71999$, $q_0 \approx 0.510004$ and $\delta z = 0.001$. Matching the M values at the first connection point and the W values at the second connection point. The solid grey curve is the correct RW expression and the dotted curve is our numerical output using Runge-Kutta as the integration method.

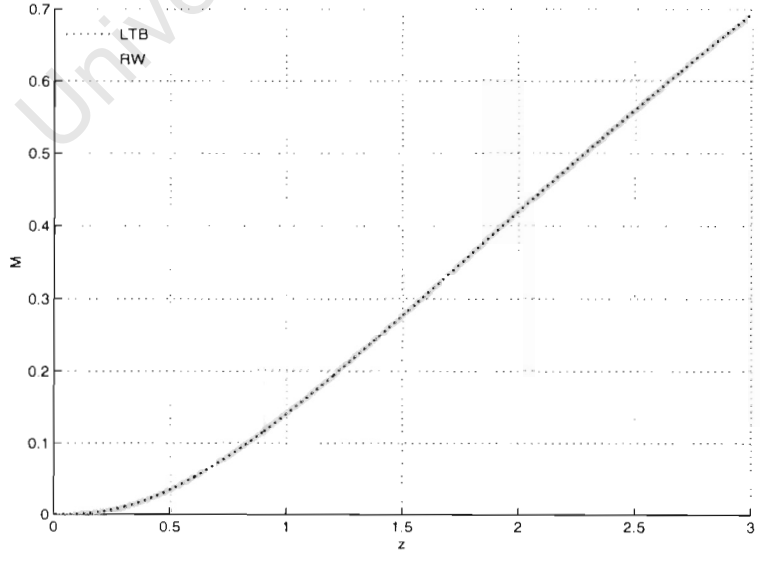

Figure 5.11: Results of W vs. z with $H_0 \approx 0.71999$, $q_0 \approx 0.510004$ and $\delta z = 0.001$. Matching the M values at the first connection point and the W values at the second connection point. The solid curve is the correct RW expression and the dotted curve is our numerical output using Euler integration as the integration method.

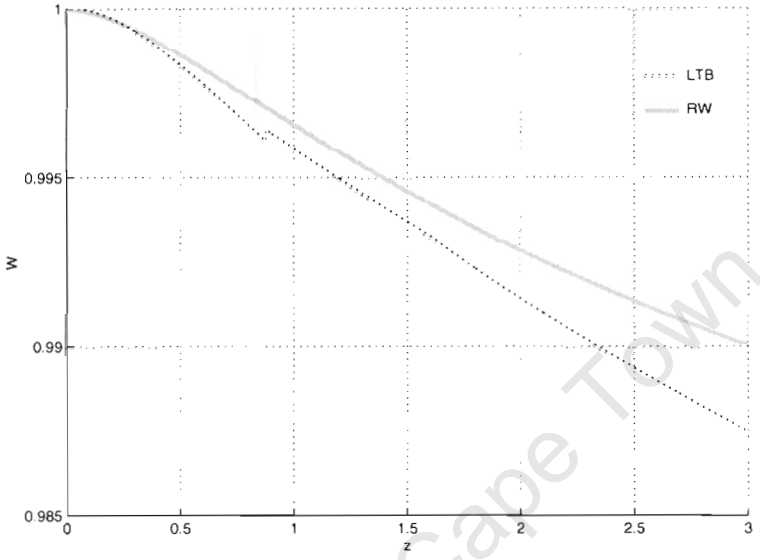

Figure 5.12: Results of W vs. z with $H_0 \approx 0.71999$, $q_0 \approx 0.510004$ and $\delta z = 0.001$. Matching the M values at the first connection point and the W values at the second connection point. The solid curve is the correct RW expression and the dotted one is our numerical output using Runge-Kutta as the integration method.

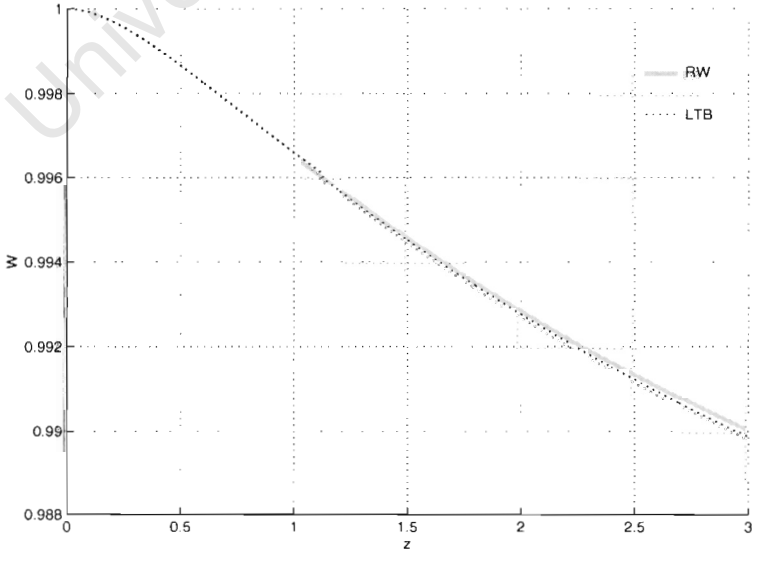

Figure 5.13: Results of τ vs. z with $H_0 \approx 0.71999$, $q_0 \approx 0.510004$ and $\delta z = 0.001$. The solid grey curve is the correct RW expression and the dotted black one is our numerical output using Runge-Kutta as the integration method.

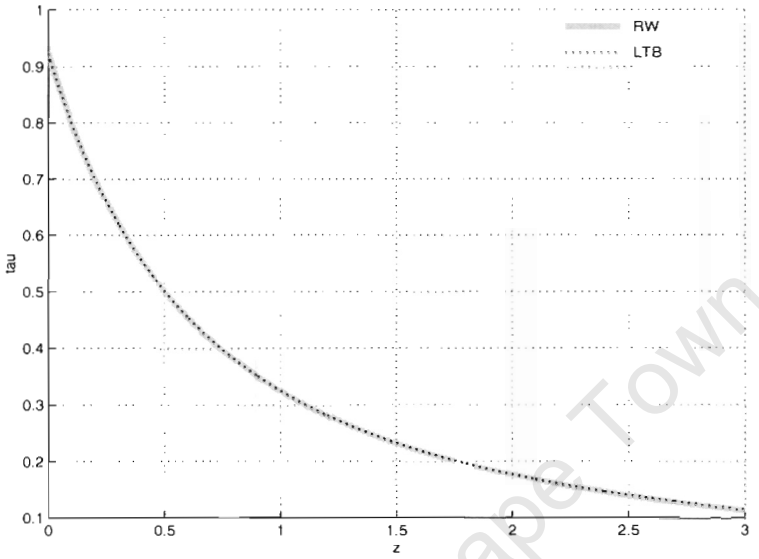

Figure 5.14: Results of t_B vs. z with $H_0 \approx 0.71999$, $q_0 \approx 0.510004$ and $\delta z = 0.001$. The thick solid grey curve is the correct RW expression and the dotted black curve is our numerical output using Runge-Kutta as the integration method. The solid black line on the top is the current age of the universe.

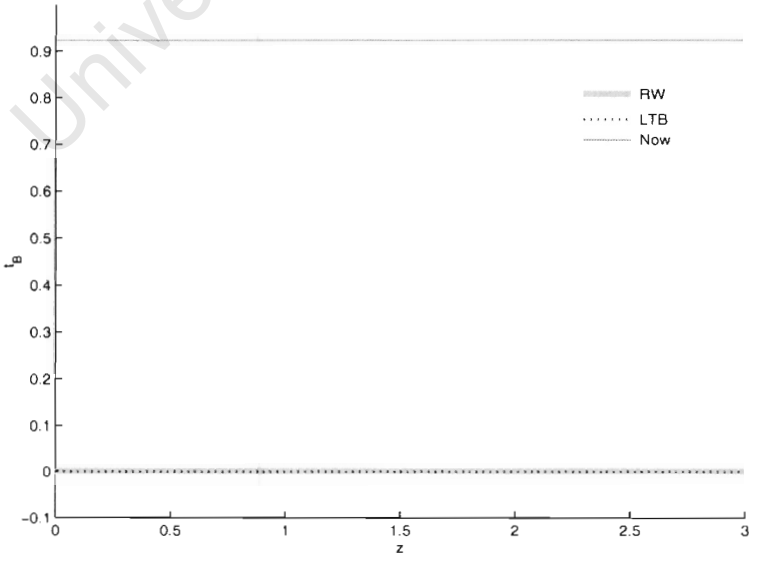

5.3 Homogeneous model with $q_{0d} = 0.1$ and $H_{0d} = 0.72$

From the cases we have shown so far, it is evident that changing over to the Runge-Kutta method from Euler method was necessary. Therefore, from here onward, we only show the results obtained using the Runge-Kutta method.

The case we choose here is again a negatively curved universe, but now with very low density, i.e. small q_{0d}. As one can see from Figures 5.15-5.17, the accuracy for our numerical output is about the same as the previous case. If one looks at Figures 5.18, the two W curves are in surprisingly good accord with each other, since there are no visible jumps at the connection points z_a and z_J.

Looking at Figure 5.19, the two τ curves coincide well as expected, and the t_B and t_0 results in Figure 5.20 are similarly satisfactory.

Figure 5.15: Results of r vs. z with $H_0 \approx 0.71999$, $q_0 \approx 0.1000004$ and $\delta z = 0.001$. The grey curve is the correct RW expression and the dotted black one is our numerical output using Runge-Kutta as the integration method.

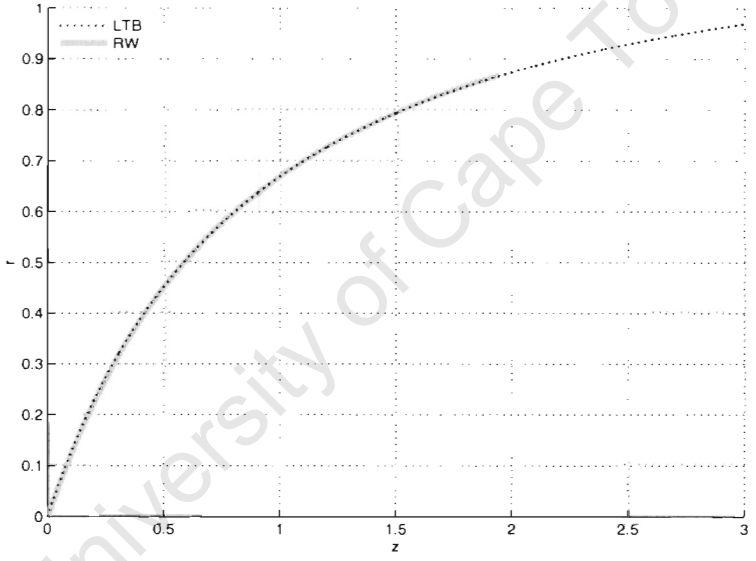

Figure 5.16: Results of ϕ vs. z with $H_0 \approx 0.71999$, $q_0 \approx 0.1000004$ and $\delta z = 0.001$. The grey curve is the correct RW expression and the dotted black one is our numerical output using Runge-Kutta as the integration method.

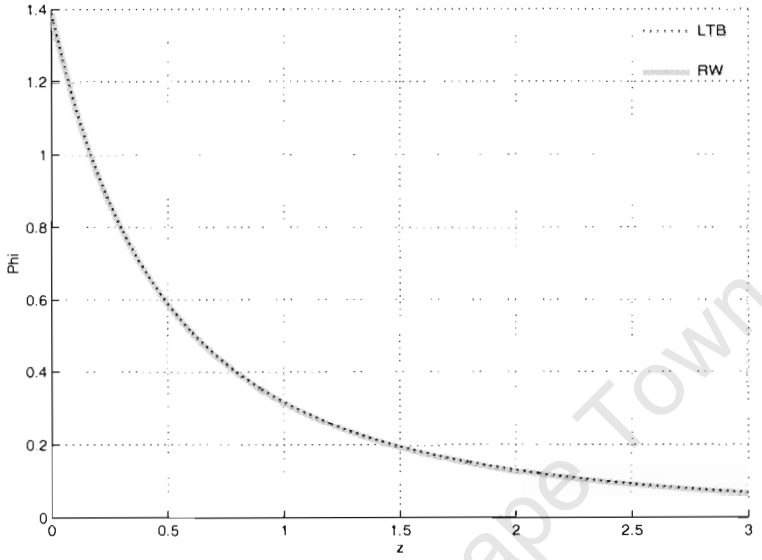

Figure 5.17: Results of M vs. z with $H_0 \approx 0.71999$, $q_0 \approx 0.1000004$ and $\delta z = 0.001$. Matching the M values at the first connection point and the W values at the second connection point. The grey curve is the correct RW expression and the dotted black one is our numerical output using Runge-Kutta as the integration method.

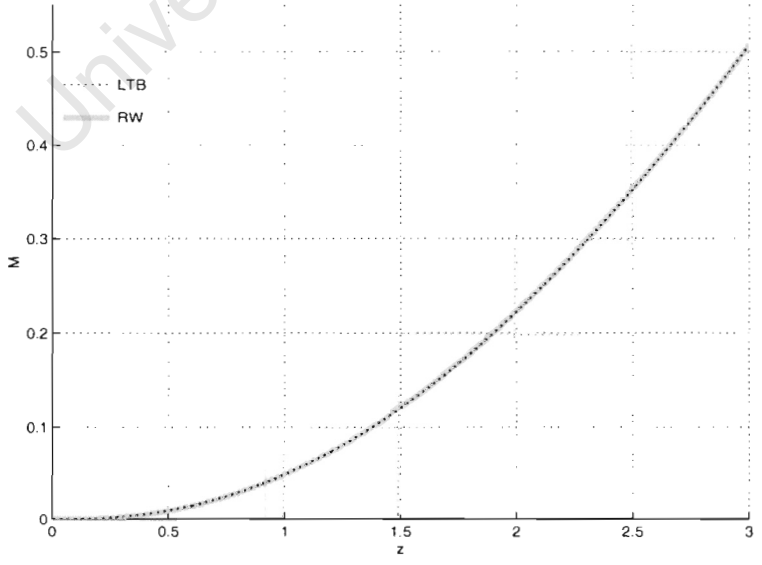

Figure 5.18: Results of W vs. z with $H_0 \approx 0.71999$, $q_0 \approx 0.1000004$ and $\delta z = 0.001$. Matching the M values at the first connection point and the W values at the second connection point. The grey curve is the correct RW expression and the dotted black one is our numerical output using Runge-Kutta as the integration method.

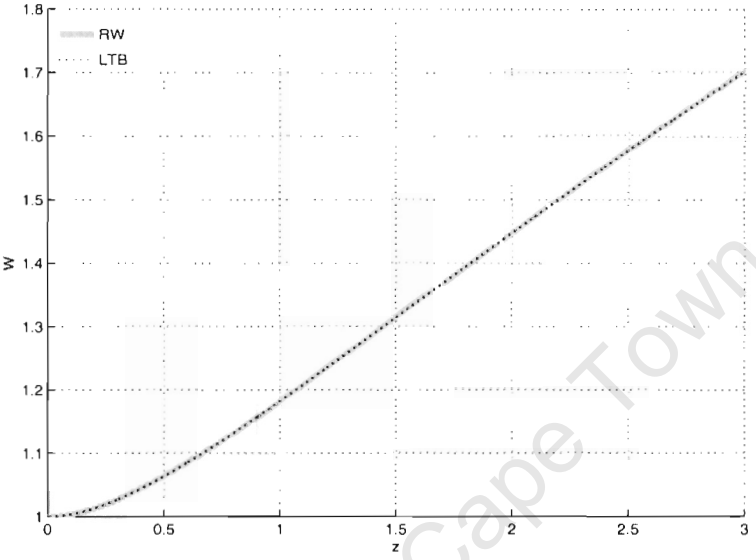

Figure 5.19: Results of τ vs. z with $H_0 \approx 0.71999$, $q_0 \approx 0.1000004$ and $\delta z = 0.001$. The grey curve is the correct RW expression and the dotted black one is our numerical output using Runge-Kutta as the integration method.

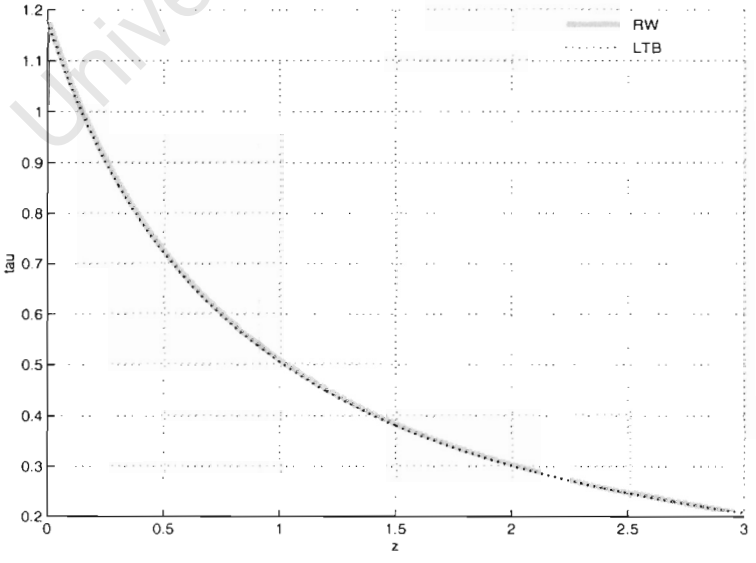

Figure 5.20: Results of t_B vs. z with $H_0 \approx 0.71999$, $q_0 \approx 0.1000004$ and $\delta z = 0.001$. The thick solid grey curve is the correct RW expression and the dotted black one is our numerical output using Runge-Kutta as the integration method. The solid black line on the top is the current age of the universe.

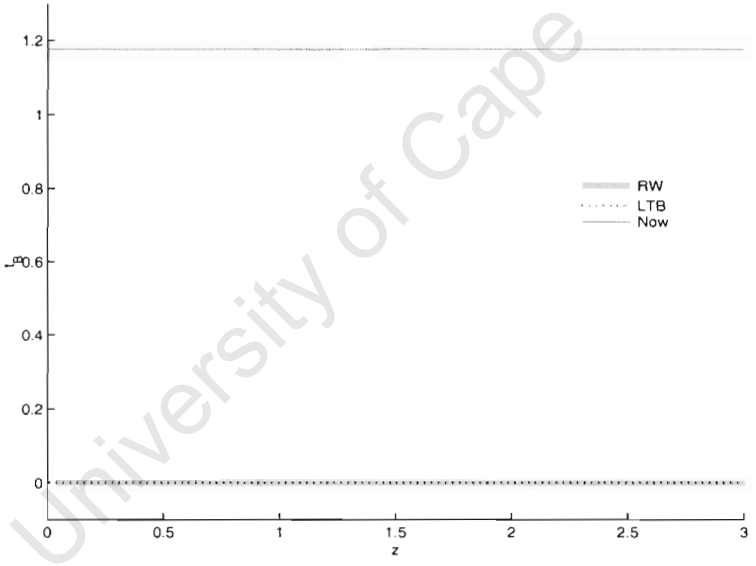

5.4 Homogeneous model with $q_{0d} = 0.8$ and $H_{0d} = 0.72$

This final case is a high density, positively curved universe. With the r, ϕ and M graphs, we have the same kind of accuracy as before (see Figures 5.21-5.23). As in the previous case, the two W curves shown in Figure 5.24 are in good agreement with each other and there is no visible jump on the curve plotted from our numerics. So too the τ and t_B plots in Figures 5.25 and 5.26 demonstrate a consistently good agreement.

Figure 5.21: Results of r vs. z with $H_0 \approx 0.71999$, $q_0 \approx 0.80001$ and $\delta z = 0.001$. The grey curve is the correct RW expression and the dotted black one is our numerical output using Runge-Kutta as the integration method.

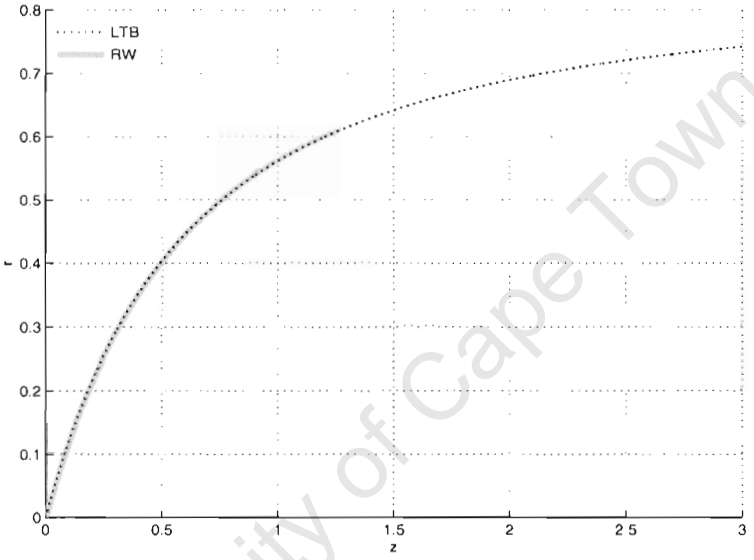

Figure 5.22: Results of ϕ vs. z with $H_0 \approx 0.71999$, $q_0 \approx 0.80001$ and $\delta z = 0.001$. The grey curve is the correct RW expression and the dotted black one is our numerical output using Runge-Kutta as the integration method.

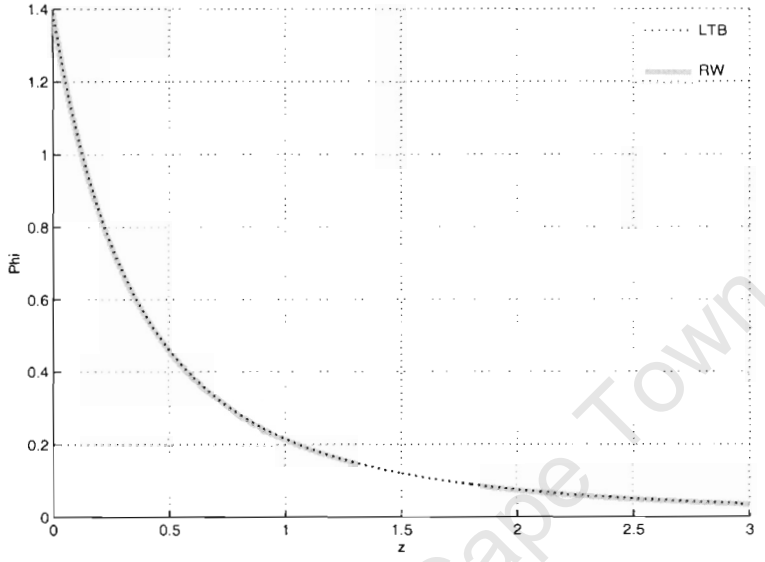

Figure 5.23: Results of M vs. z with $H_0 \approx 0.71999$, $q_0 \approx 0.80001$ and $\delta z = 0.001$. Matching the M values at the first connection point and the W values at the second connection point. The grey curve is the correct RW expression and the dotted black one is our numerical output using Runge-Kutta as the integration method.

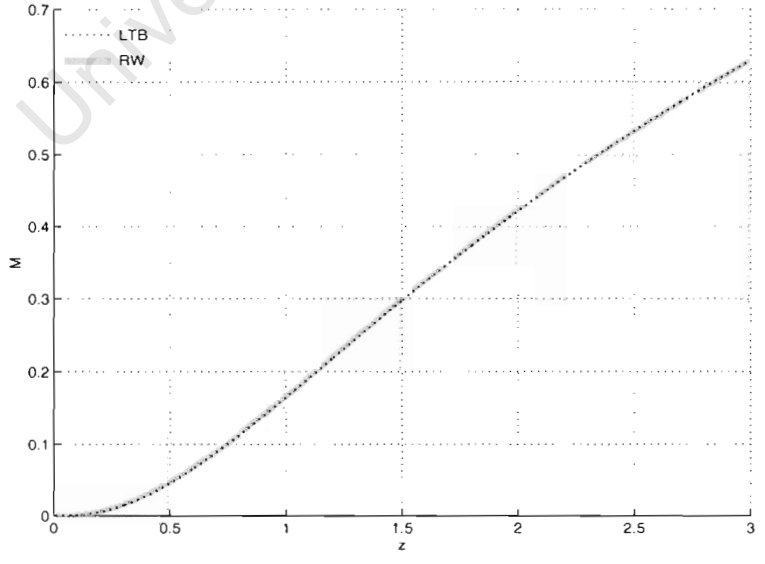

Figure 5.24: Results of W vs. z with $H_0 \approx 0.71999$, $q_0 \approx 0.80001$ and $\delta z = 0.001$. Matching the M values at the first connection point and the W values at the second connection point. The solid grey curve is the correct RW expression and the dotted one is our numerical output using Runge-Kutta as the integration method.

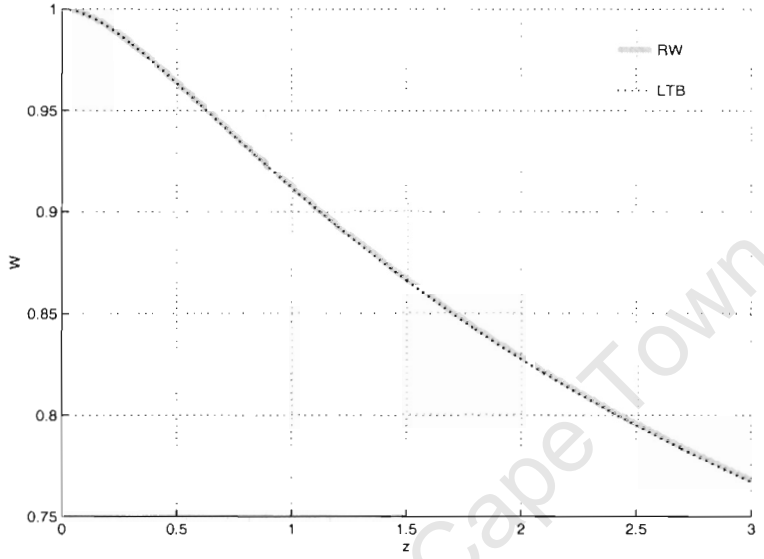

Figure 5.25: Results of τ vs. z with $H_0 \approx 0.71999$, $q_0 \approx 0.80001$ and $\delta z = 0.001$. The solid grey curve is the correct RW expression and the dotted black one is our numerical output using Runge-Kutta as the integration method.

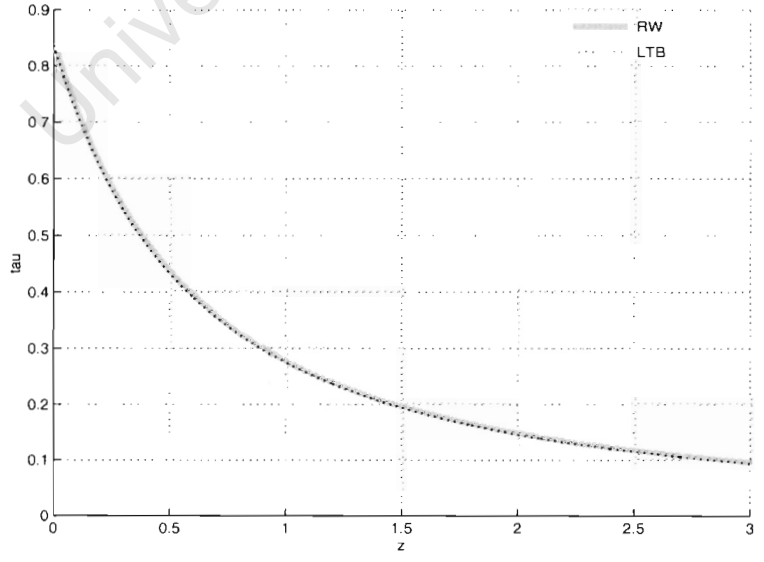

Figure 5.26: Results of t_B vs. z with $H_0 \approx 0.71999$, $q_0 \approx 0.80001$ and $\delta z = 0.001$. The thick solid grey curve is the correct RW expression and the dotted black one is our numerical output using Runge-Kutta as the integration method. The solid black line is the current age of the universe.

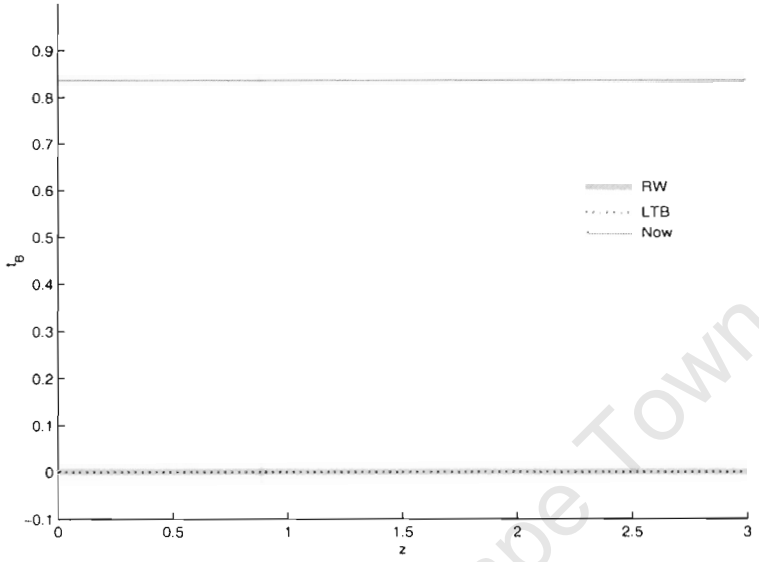

From the test done so far, the curves representing our numerical output are mostly in very good agreement with the ones generated from the RW expressions. Although the W result does accumulate noticeable numerical error while using Euler integration, the percentage errors are still acceptable. However, once we change over to the second order Runge-Kutta method the percentage errors are all below 0.05 % which is more than enough. Once again we emphasise that observational uncertainties will swamp numerical error from almost any numerical method.

After successfully passing these numerical validations, we can now say our numerical method should be able to handle any homogeneous data correctly without difficulties. What we need to do next is to test its ability to handle fake data from inhomogeneous models.

Chapter 6

Numerical comparisons of inhomogeneous models

In this chapter, we want to test the ability of our computer programme to arrive at the correct inhomogeneous cosmological model from the fake data. First, we describe the possible approaches to generating the fake data, since it is not so obvious due to the particular coordinate choice and the observer past null cone we have. However, since there are some inhomogeneous null cone data already generated by C.W. Hellaby for the purpose of another project, we use those data for testing our computer programme. A brief description of the approach for the data generation by Hellaby is followed by the results from testing our code with them for four different cases. The first one has varying bang time, the second one has varying geometry/energy, the third one with varying mass and the last one with strong inhomogeneity.

6.1 Methods of data generation

As mentioned before, the LTB model is the simplest inhomogeneous model, and the three arbitrary functions - M, E and t_B - fully determine the model. Therefore, as soon as we specify the three arbitrary functions one can locate the past null cone and generate fake observational data. There are two ways of generating the inhomogeneous data. The first approach is to choose the three arbitrary functions freely, however one has to be careful that no shell crossings occur. Also, one needs to locate the particular past null cone using the null cone path equation (3.21) before evaluating z, $\hat{R}$ and $4\pi\hat{m}n$. The complexity involved in this approach is great, however there is a second approach that may make it easier to generate the fake data. In this approach, we impose the condition $\widehat{R'}/\sqrt{1+2E} = 1$, as in equation (3.22), which means we immediately know the locus of the null cone. The price we pay for this is that we cannot specify all three arbitrary functions freely, one must be found from the other two. And in both approaches, the origin must be RW like.

6.1.1 Procedures for data generation – approach I

The programme developed by Hellaby for generating fake inhomogeneous data is close to the first method we mentioned before. It can produce values for the two data input function $\hat{R}(z)$ and $4\pi\hat{m}n(z)$ once given definitions for the three LTB arbitrary functions and the

values for H_{0d} and q_{0d} at the origin (observer). These two parameters define the time of observation and constrain some of the coefficients in the arbitrary functions.

In the first part of the programme, there is a model choosing routine that sets the three arbitrary functions E, M and t_B by specifying which of several functional forms to use, and setting the parameters used in each form. Then, at the origin, where we have the LTB model being RW like, it puts $2E \sim -kr^2$ and $M \sim M_3 r^3$. The two RW parameters H_{0d} and q_{0d} are then used in order to determine the value of M_3, and also to give values of $\widehat{R'}(t_0, 0)$, $d\hat{R}/dr$, $d\hat{t}/dr$, $\widehat{\dot{R}}$, and $d\ln(1+z)/dr$.

If one differentiates equation (3.2) with respect to r, and evaluates it on the null cone, one obtains

$$\widehat{\dot{R}} = \frac{\frac{2M'}{\hat{R}} - \frac{2M\widehat{R'}}{\hat{R}^2} + 2E'}{2\widehat{\dot{R}}} \ . \tag{6.1}$$

The main part of the programme integrates the equations (6.1), (3.21), (3.28), (3.44) and (3.7) down the past null cone, using a second order method. It calls a routine to evaluate the three arbitrary functions at each r, and another routine to evaluate $\hat{R}$ from the given τ, M, E and t_B values.

Finally, for the last part of the programme, there is a routine to interpolate the calculated data points, to find the output data on regularly spaced z values. The generated data is then dumped to a file for use by the programme that integrates null cone data to give metric functions.

6.1.2 Procedures for data generation – approach II

The second way of generating the fake data is to pick any two arbitrary functions, say $E(r)$ and $t_B(r)$. At r, assume that we already know values of $M(r)$, $E(r)$, $t_B(r)$, $\hat{t}$, $\hat{R}$ and $\hat{\eta}$. We wish to find their values at $r + dr$. We make a gauge choice which immediately fixes the null cone locus:

$$\frac{\widehat{R'}}{\sqrt{1+2E}} = 1 \ \Rightarrow \ \hat{t} = t_0 - r \ . \tag{6.2}$$

Since $t_B(r)$ and $E(r)$ are known, dt_B/dr and dE/dr are also known because they can be generated numerically from $t_B(r)$ and $E(r)$. Using equation (3.28)

$$\frac{d\hat{R}}{dr} = \sqrt{1+2E} - \sqrt{\frac{2M}{\hat{R}} + 2E} \ , \tag{6.3}$$

we can then generate the values of $\hat{R}$ since we have the values of E, M and r.

Recall equation (3.7) that gives a relationship between the three arbitrary functions, R, R' and $\dot{R}$. If evaluated on the null cone, we have

$$\widehat{R'} = \left(\frac{M'}{M} - \frac{E'}{E}\right)\hat{R} - \left\{t_B' - \left(\frac{3E'}{2E} - \frac{M'}{M}\right)(t - t_B)\right\}\widehat{\dot{R}} \ . \tag{6.4}$$

It then becomes unnecessary to use the evolution equations (3.4)-(3.6) where the extra parameter $\eta(t, r)$ is used. If we use the fact that $\widehat{R'} = \sqrt{1+2E}$, then we have an expression for dM/dr:

$$\frac{dM}{dr} = M\left\{\frac{\sqrt{1+2E} + t_B'\,\widehat{\dot{R}} + \frac{E'}{E}\left(\hat{R} - \frac{3}{2}(\hat{t} - t_B)\widehat{\dot{R}}\right)}{\hat{R} - (\hat{t} - t_B)\widehat{\dot{R}}}\right\} \ . \tag{6.5}$$

Using this equation, we can now generate values for the third arbitrary function M on the null cone. This way, the three arbitrary functions automatically satisfy the coordinate choice we made.

However, all the functions above are functions of coordinate r, therefore we need to transform them into functions of redshift z as we have done in the previous chapter. This can be easily achieved if one uses equations (3.39) and (3.41). If we differentiate both sides of equation (3.39) with respect to r and substitute equation (3.41) into it, then we have

$$\frac{dz}{dr} = (1+z)\,\frac{\left(\frac{M'}{\hat{R}\sqrt{1+2E}} + \frac{E'}{\sqrt{1+2E}} - \frac{M}{\hat{R}^2}\right)}{\sqrt{\frac{2M}{\hat{R}} + 2E}}\,. \tag{6.6}$$

We can now generate the z value corresponding to each r, even if we only know the values of M, E and $\hat{R}$.

An expression for our second data input function $4\pi\hat{m}n$ is now needed. In order to obtain this, we can use equation (3.55), but one requires the value of $\hat{\rho}$. By substituting equation (3.24) into (3.55), we get an expression for $4\pi\hat{m}n$ that depends on knowing M, E and dz/dr only, and we know these values from the previous step already. The expression for $4\pi\hat{m}n$ thus takes the form:

$$4\pi\hat{m}n = \frac{M'}{\frac{dz}{dr}\sqrt{1+2E}}\,. \tag{6.7}$$

Now we can use the two expressions (6.3) and (6.7) for our two observational data functions $\hat{R}$ and $4\pi\hat{m}n$ to generate fake inhomogeneous data. As for the values near the origin, we take the same approach as we have done in the homogeneous cases – using the series expansions of the RW expressions for generating the data near the origin. This data is needed as input to the main metric extraction programme. The numerical output for M, E and t_B can then be tested against the chosen M,E and t_B.

6.2 Testing with a varying bang time model

In this model we have the two arbitrary functions E and M taking a RW form, while we vary the third function t_B. The values of the two RW parameters used at the origin are $H_{0d} = 0.72$, $q_{0d} = 0.2$ which should give us a hyperbolic case. Since for the homogeneous models, we have already demonstrated the improvement obtained by switching from Euler to Runge-Kutta integration, therefore with inhomogeneous data no further such comparisons are needed. Given that in the process of generating the fake data, the coordinate condition (3.22) was not used to generate values for equations (6.1), (3.21), (3.28), (3.44) and (6.4) down the past null cone, and also that values of the coordinate r are meaningless when it comes to the real observational data; we consequently do not present the graphs for z vs. r and z vs. ϕ for any of the inhomogeneous cases.

The derived values are $H_0 \approx 0.719$ and $q_0 \approx 0.19982$ for the two RW parameters, which is well under 1% error. From Figure 6.1 one can see that the two M curves are in very good agreement with each other. However, Figure 6.2 does indicate a small difference between the two W curves when we approach $z = 3$. In fact, there is a 0.3836 % error for our numerics at $z = 3$. Although this percentage error is bigger than the ones we had for the homogeneous cases, this is to be expected since we are working with inhomogeneous data which was numerically generated.

From Figures 6.3 and 6.4 we can see that the curve plotted from the correct data and the curves plotted from our numerics are generally in good agreement with each other for both τ and t_B, except near the origin. However, this is due to the accuracy in the H_0 and q_0 values we deduce from the "observational" data at $z = 3/2\delta z$. If we now put $H_0 \approx 0.719$ and $q_0 \approx 0.199922$, the improvement can be seen in Figures 6.5 and 6.6. Although the jumps are still visible, they have been reduced by approximately 36%. Therefore, one thing that will have to be done in the future is to do a least squares fit near the origin in order to estimate H_0 and q_0 to better accuracy. It is, after all, unlikely that we can generate accurate values for the two RW parameters H_0 and q_0 using the data from just one z bin. Nevertheless, accurate values for τ and t_B depend on an accurate q_0 value, which is particularly difficult to get at the low z values near the origin.

Figure 6.1: Results of M vs. z with $H_0 \approx 0.719$, $q_0 \approx 0.19982$ and $\delta z = 0.001$. The grey curve is from the correct testing data and the dotted black curve is our numerical output using Runge-Kutta as the integration method.

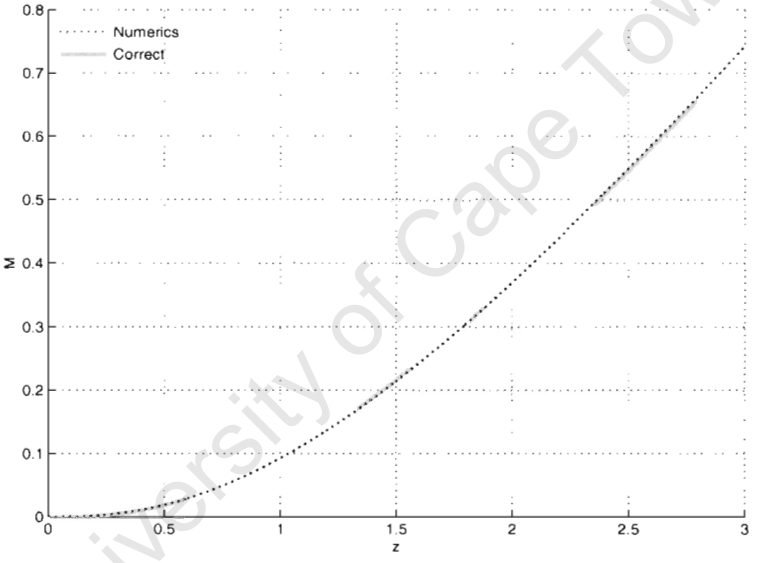

Figure 6.2: Results of W vs. z with $H_0 \approx 0.719$, $q_0 \approx 0.19982$ and $\delta z = 0.001$. The grey curve is from the correct testing data and the dotted black curve is our numerical output using Runge-Kutta as the integration method.

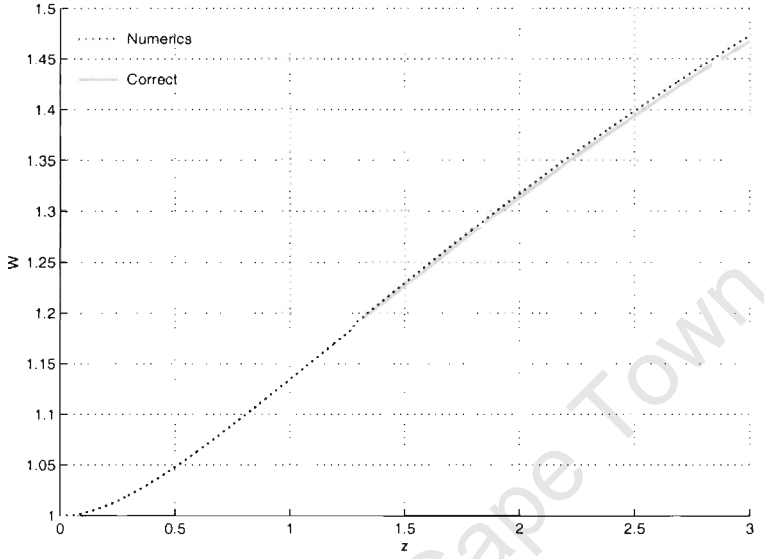

Figure 6.3: Results of τ vs. z with $H_0 \approx 0.719$, $q_0 \approx 0.19982$ and $\delta z = 0.001$. The grey curve is from the correct testing data and the dotted black curve is our numerical output using Runge-Kutta as the integration method.

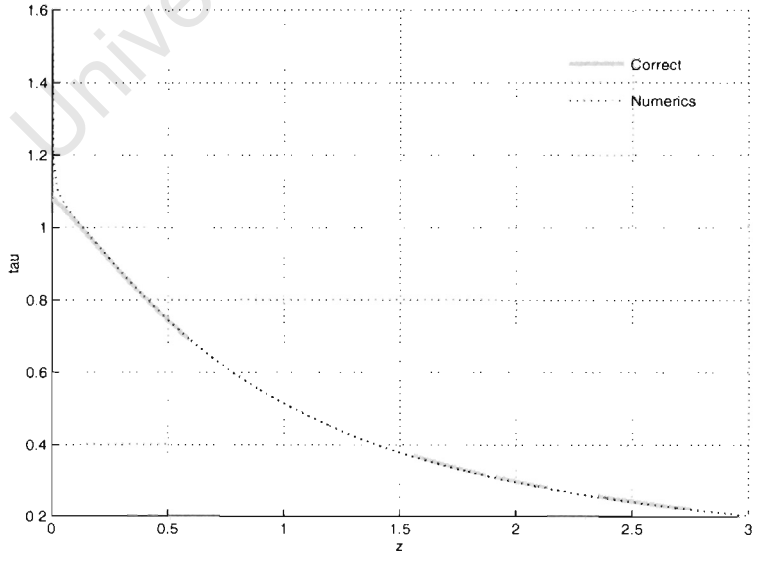

Figure 6.4: Results of t_B vs. z with $H_0 \approx 0.719$, $q_0 \approx 0.19982$ and $\delta z = 0.001$. The thick solid grey curve is from the correct correct testing data and the dotted black one is our numerical output using Runge-Kutta as the integration method. The solid black curve is the current time (origin)

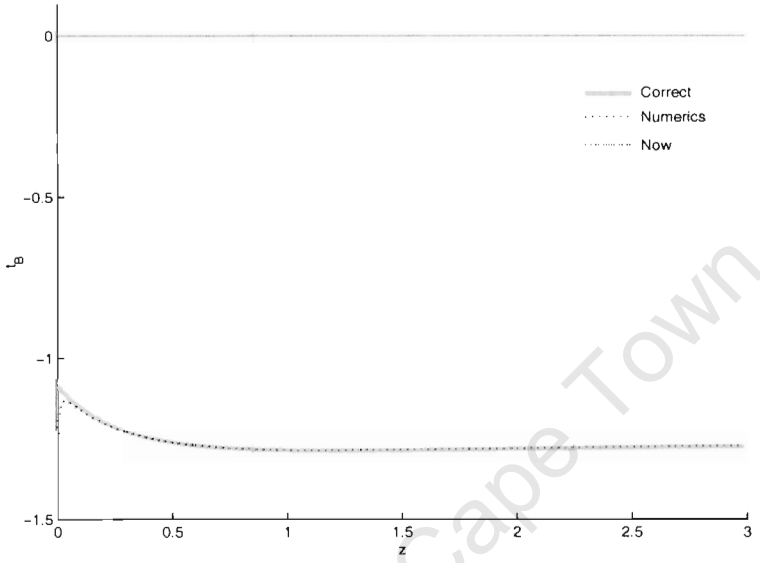

Figure 6.5: Results of τ vs. z with $H_0 \approx 0.719$, $q_0 \approx 0.199922$ and $\delta z = 0.001$. The grey curve is from the correct testing data and the dotted black curve is our numerical output using Runge-Kutta as the integration method with improved near origin values.

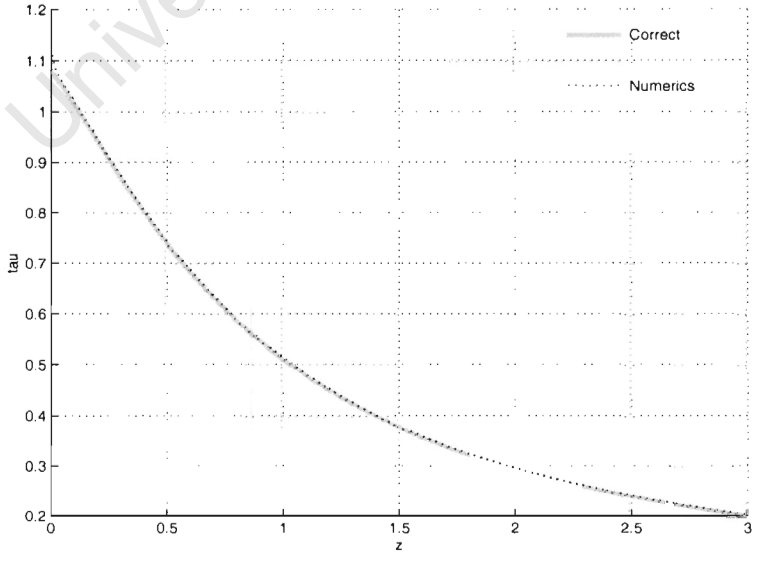

Figure 6.6: Results of t_B vs. z with $H_0 \approx 0.719$, $q_0 \approx 0.199922$ and $\delta z = 0.001$. The thick solid grey curve is from the correct correct testing data and the dotted black one is our numerical output using Runge-Kutta as the integration method with improved near origin values. The solid black line is the current time (origin).

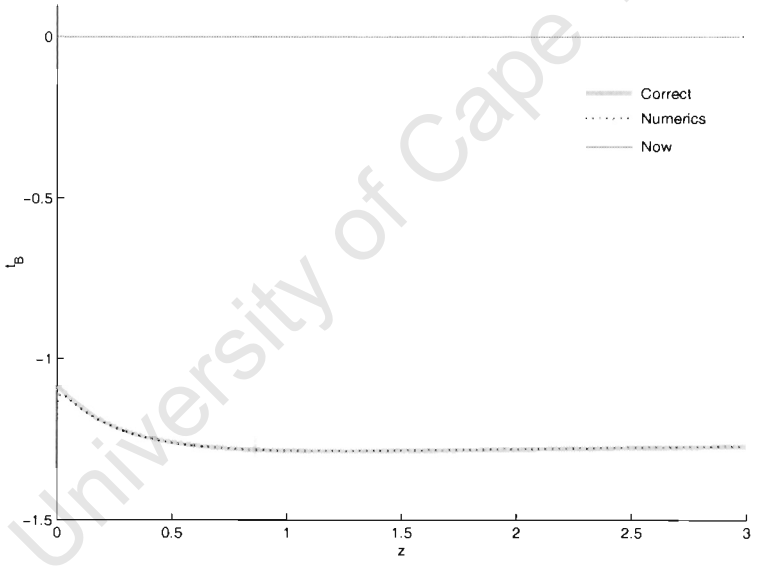

6.3 Testing with a varying mass model

This model has the two arbitrary functions E and t_B taking a RW form, while we vary the third function M. The values of the two RW parameters used are $H_{0d} = 0.72$, $q_{0d} = 0.22$ which is a hyperbolic case. The derived values are $H_0 \approx 0.719$ and $q_0 \approx 0.22098$ for the two central RW parameters.

From Figure 6.7 one can see that the two M curves are in very good agreement with each other. However, although Figure 6.8 does indicate a small difference between the two W curves; in fact, there is only 0.3167 % error once we reach $z = 3$.

From Figures 6.9 and 6.10 we see that the original and numerical τ and t_B curves are in good agreement with each other, except near the origin. However, this is due to the imperfect H_0 and q_0 values we extracted from the data at $z = 3/2\delta z$, as demonstrated in the previous case.

Figure 6.7: Results of M vs. z with $H_0 \approx 0.719$, $q_0 \approx 0.22098$ and $\delta z = 0.001$. The grey curve is from the correct testing data and the dotted black curve is our numerical output using Runge-Kutta as the integration method.

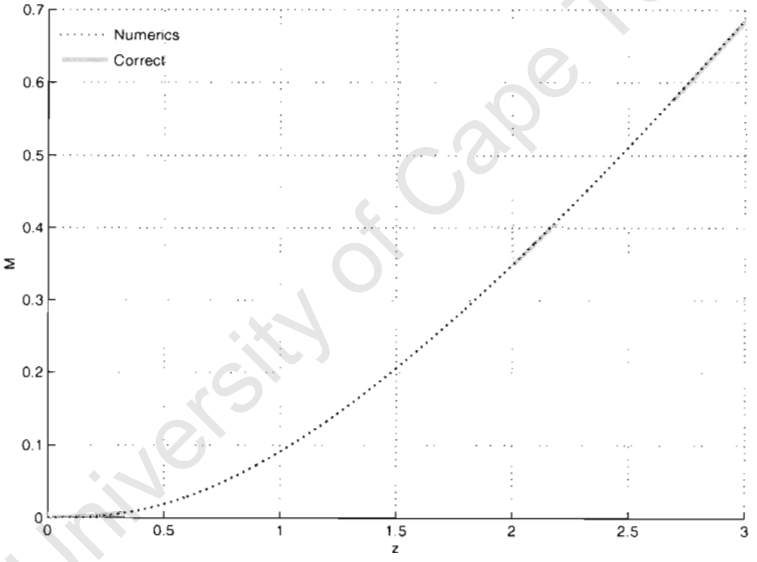

Figure 6.8: Results of W vs. z with $H_0 \approx 0.719$, $q_0 \approx 0.22098$ and $\delta z = 0.001$. The grey curve is from the correct testing data and the dotted black curve is our numerical output using Runge-Kutta as the integration method.

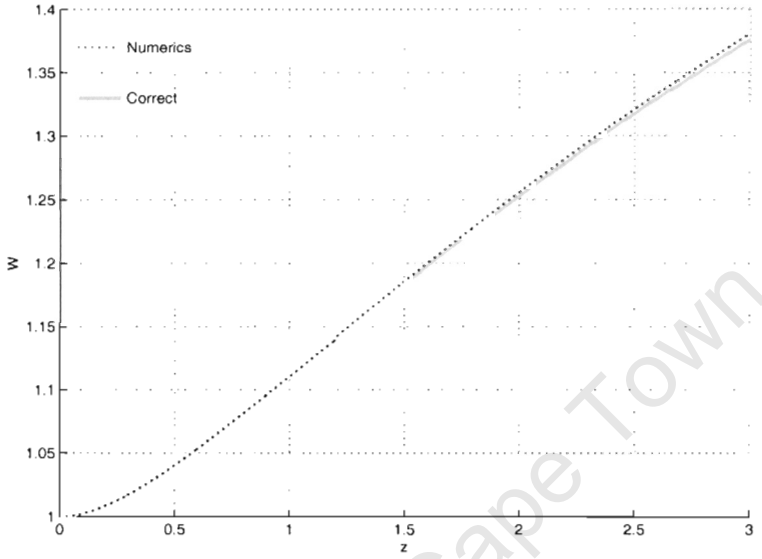

Figure 6.9: Results of τ vs. z with $H_0 \approx 0.719$, $q_0 \approx 0.22098$ and $\delta z = 0.001$. The grey curve is from the correct testing data and the dotted black curve is our numerical output using Runge-Kutta as the integration method.

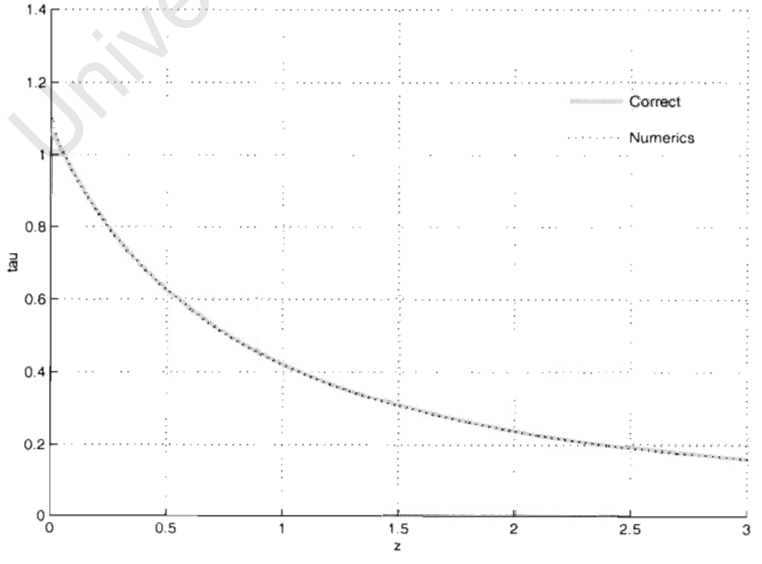

Figure 6.10: Results of t_B vs. z with $H_0 \approx 0.719$, $q_0 \approx 0.22098$ and $\delta z = 0.001$. The thick solid grey curve is from the correct correct testing data and the dotted black one is our numerical output using Runge-Kutta as the integration method. The solid black line is the current time (origin).

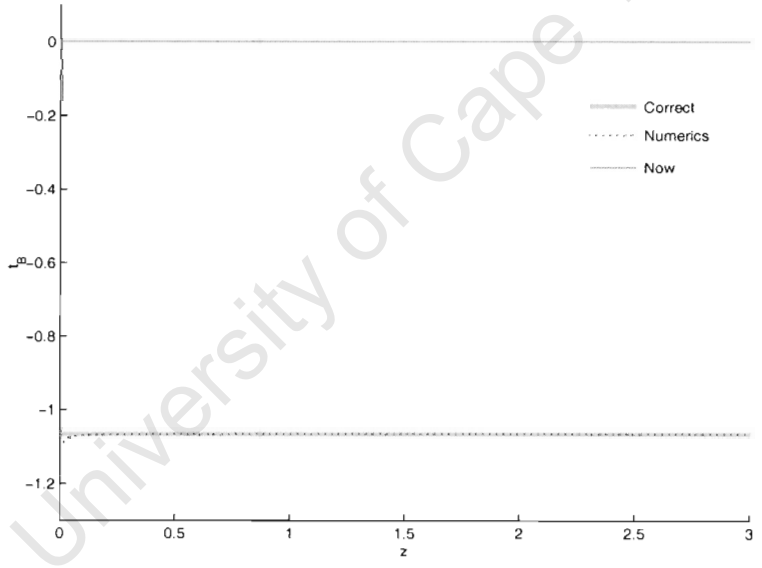

6.4 Testing with a varying geometry/energy model

This model is one in which the two arbitrary functions M and t_B take a RW form, while we vary the third function E. The two RW parameters are $H_{0d} = 0.72$, $q_{0d} = 0.52$, which gives us a near-parabolic case.

The extracted values are $H_0 \approx 0.71953$ and $q_0 \approx 0.52421$ for the two RW parameters. Figure 6.11 shows that the M curve plotted from our numerical output is slightly below the correct one; in fact there is about 2.17% error at $z = 3$. The percentage error is a bit larger for W, being about 26.6 percent as shown in Figure 6.12. Although the percentage error we obtain in W is quite big, this is mostly because W is quite small, and we note that the absolute errors in $E = (W^2 - 1)/2$ are about the same as before.

From Figures 6.13 and 6.14 for τ and t_B we can see that our numerics are in good agreement with the correct values except again near the origin.

Figure 6.11: Results of M vs. z with $H_0 \approx 0.71953$, $q_0 \approx 0.52421$ and $\delta z = 0.001$. The solid grey curve is from the correct testing data and the dotted black curve is our numerical output using Runge-Kutta as the integration method.

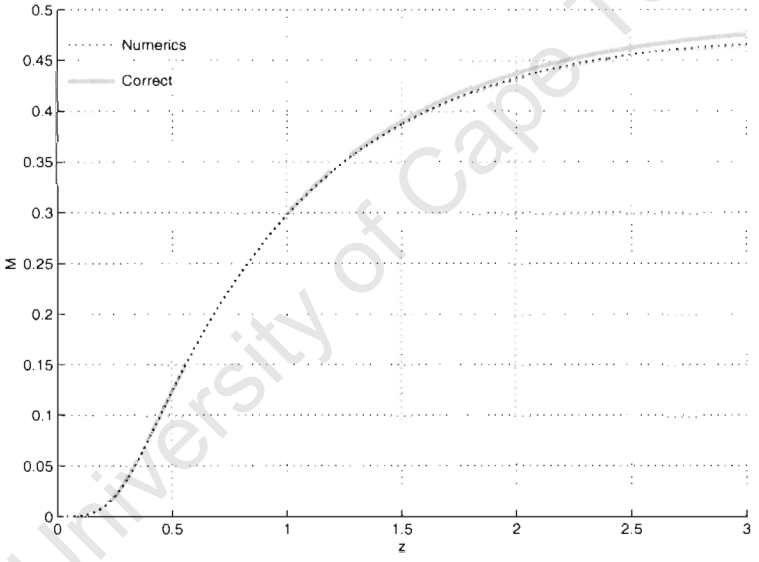

Figure 6.12: Results of W vs. z with $H_0 \approx 0.71953$, $q_0 \approx 0.52421$ and $\delta z = 0.001$. The solid grey curve is from the correct testing data and the dotted black curve is our numerical output using Runge-Kutta as the integration method.

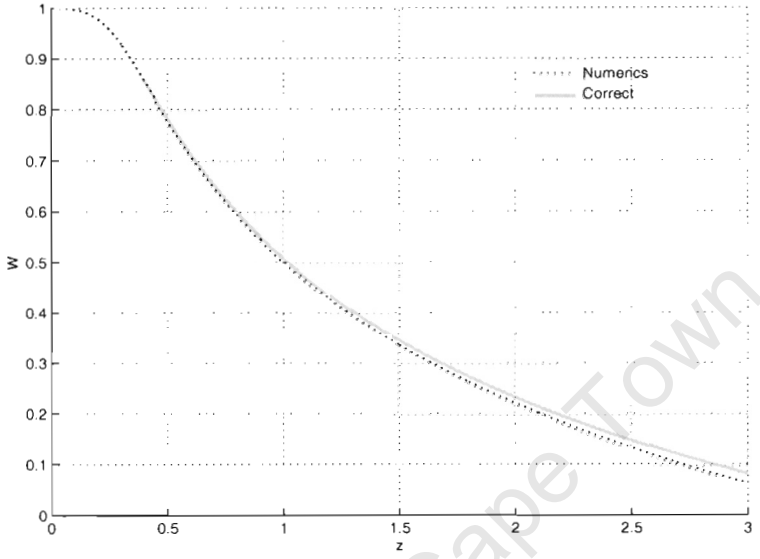

Figure 6.13: Results of τ vs. z with $H_0 \approx 0.71953$, $q_0 \approx 0.52421$ and $\delta z = 0.001$. The grey curve is from the correct testing data and the dotted black curve is our numerical output using Runge-Kutta as the integration method.

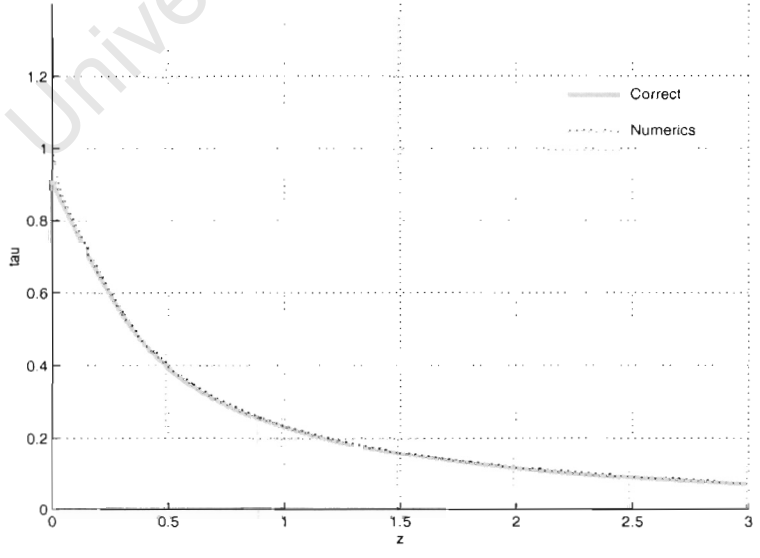

Figure 6.14: Results of t_B vs. z with $H_0 \approx 0.71953$, $q_0 \approx 0.52421$ and $\delta z = 0.001$. The thick solid grey curve is from the correct correct testing data and the dotted black one is our numerical output using Runge-Kutta as the integration method. The solid black line is the current time (origin).

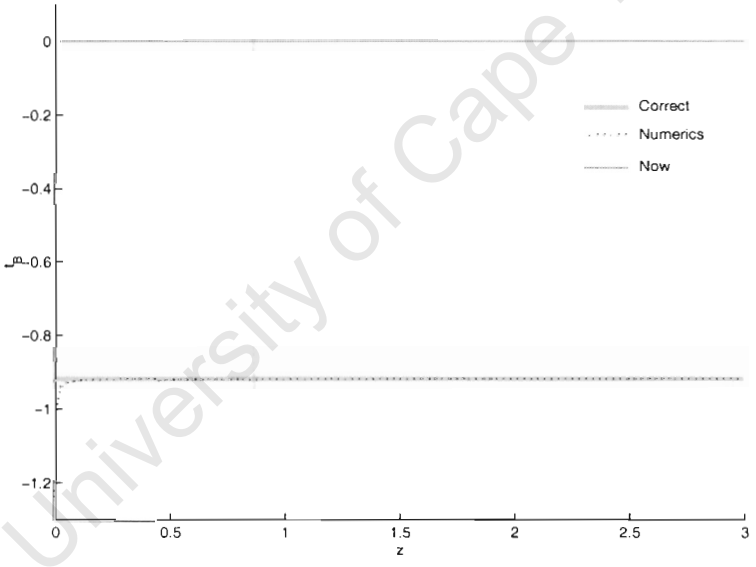

6.5 Testing with a strongly inhomogeneous model

This model has none of the three arbitrary functions taking RW form, thus giving us a much more inhomogeneous model than the previous ones. The values of the two RW parameters used at the origin are $H_{0d} = 0.72$, $q_{0d} = 0.6$. This should give us an elliptic case.

The extracted values are $H_0 \approx 0.72018$ and $q_0 \approx 0.59959$ for the two RW parameters. From Figure 6.15 one sees once again that the two M curves are in good agreement with each other. However, Figure 6.16 does show about 0.1898 % error between the two W curves near $z = 3$.

From Figures 6.13 and 6.14 we can see that our numerics τ and t_B curves are in generally good agreement with the correct ones, and the jumps near the origin are not visible in either of the τ and t_B figures.

Figure 6.15: Results of M vs. z with $H_0 \approx 0.72018$, $q_0 \approx 0.59959$ and $\delta z = 0.001$. The grey curve is from the correct testing data and the dotted black curve is our numerical output using Runge-Kutta as the integration method.

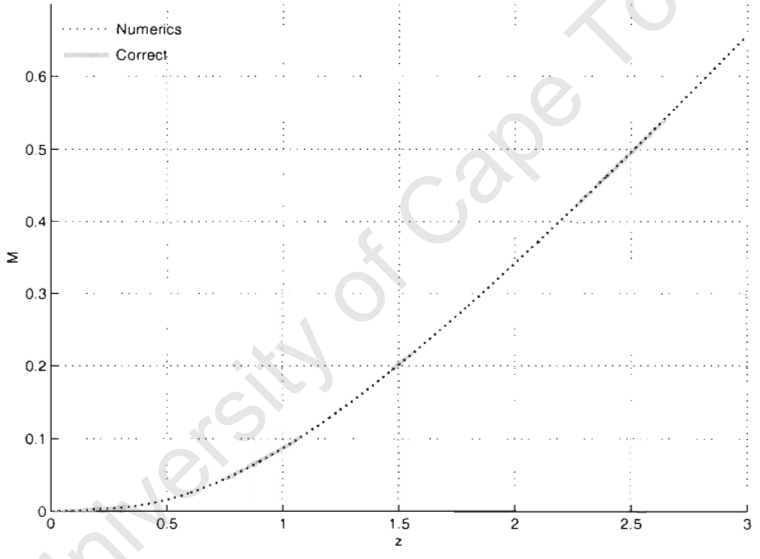

Figure 6.16: Results of W vs. z with $H_0 \approx 0.72018$, $q_0 \approx 0.59959$ and $\delta z = 0.001$. The grey curve is from the correct testing data and the dotted black curve is our numerical output using Runge-Kutta as the integration method.

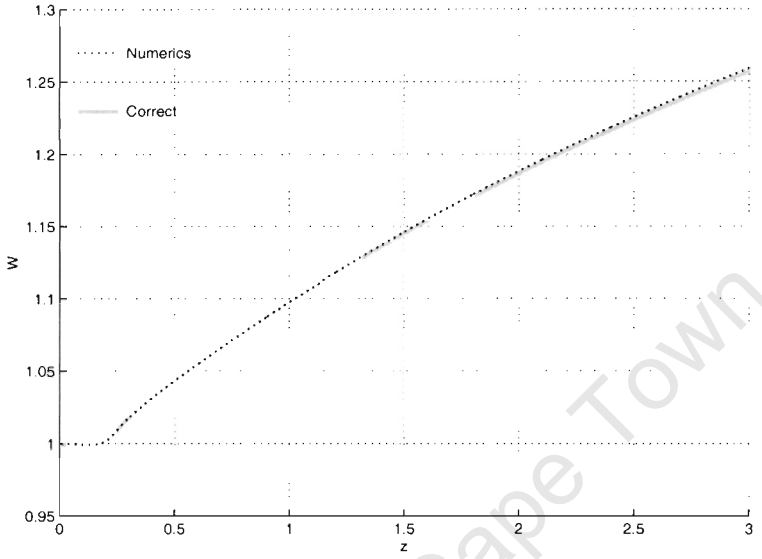

Figure 6.17: Results of τ vs. z with $H_0 \approx 0.72018$, $q_0 \approx 0.59959$ and $\delta z = 0.001$. The solid grey curve is from the correct testing data and the dotted black curve is our numerical output using Runge-Kutta as the integration method.

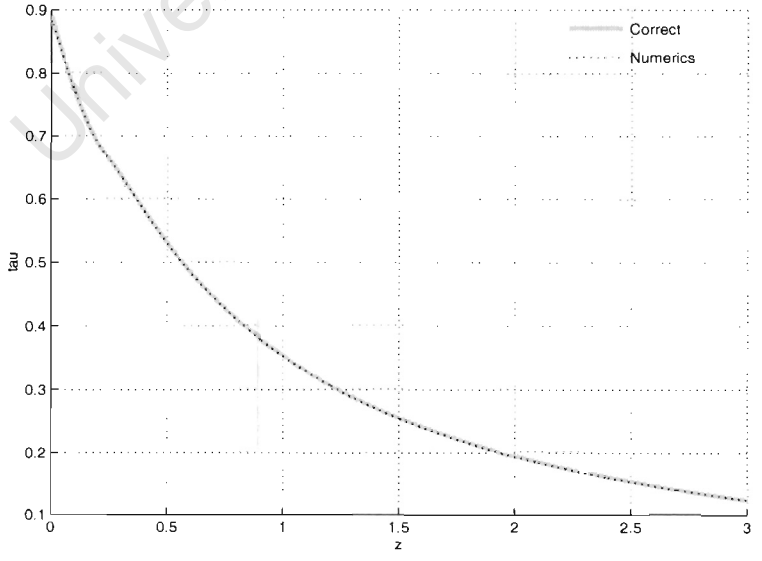

Figure 6.18: Results of t_B vs. z with $H_0 \approx 0.72018$, $q_0 \approx 0.59959$ and $\delta z = 0.001$. The thick solid grey curve is from the correct correct testing data and the dotted black one is our numerical output using Runge-Kutta as the integration method. The solid black line is the current time (origin).

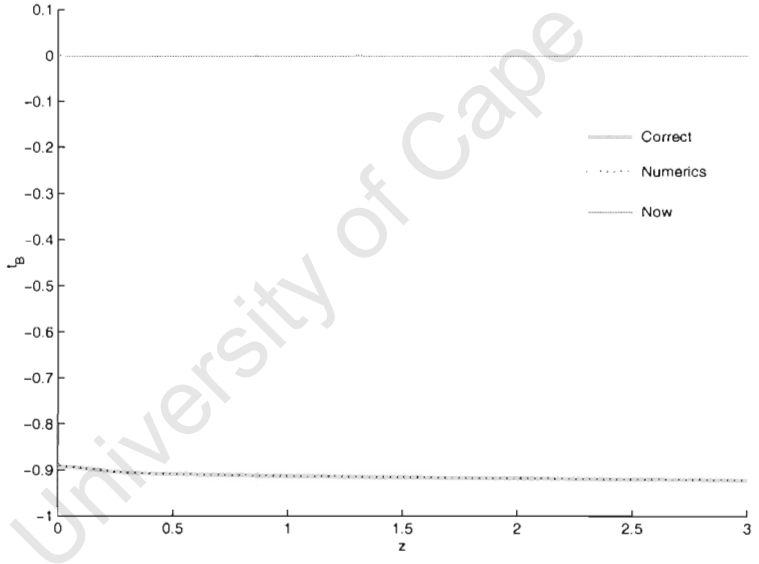

Chapter 7

Conclusions

We have developed a computer programme to implement the MHE algorithm. Given (spherically symmetric) data from standard observations for redshift, apparent diameter, apparent luminosity and galaxy number counts, as well as the associated evolution functions, true diameter, absolute luminosity and mass per source, it determines the metric of the (observed) universe. Its ability to reproduce the correct metric information has been tested via artificial data generated from both homogeneous and inhomogeneous models. We started with the simplest numerical integration method – Euler's method, which is only a linear approximation on each z interval. However, persistent discrepancies later convinced us a 2nd order Runge-Kutta method was necessary. The improvement we obtained in our numerical output going from a first to a second order integration method is clearly demonstrated in some of the figures in both chapters 4 and 5. The next stage in testing our code would be to do a test run with some real observational data, however this is not within the scope of this thesis.

We have started with a very simple case, in order to understand the key elements of a numerical extraction of metric information from observations. Obviously one does not wish to tackle the full complexity of the problem at the start. Thus, there are still many improvements which can be made in both the theory and the numerical method used. Many considerations and effects must be included, for example, source evolution theories, data set completeness, different populations of sources, and more. At some point, a non-zero Λ should be considered. Also, issues like a least squares fit for the data near the origin in order to obtain better accuracy for H_0 and q_0, and a shorter z range for the series expansion in order to carry our numerics through the point $\hat{R}_{max}$, also need to be dealt with for the future development. Of course, a higher order integration method may also be needed in the future in order to sustain the accuracy we have so far in our numerical output out to larger z values. However, any method we use must be able to handle both known data and unknown functions at a discrete set of positions, which texts on numerical methods for DE solving never consider.

One thing we need to point out is that the actual bin size we use will affect the accuracy of the bin averages, and require special attention when one works with the real data. If we have the same bin size for the whole redshift range, we are always going to have some bins flooded with data, for example the higher redshift regions; and some bins with too sparse data, for instance the low redshift regions nearby. If we use different bin sizes for different redshift intervals, in order that every redshift bin contains the same amount of data in it, then we may have some bins with a very narrow redshift range, and some with a very wide

range. In fact, it is not possible to have the data distributed uniformly and binning of the data actually gives us a sense of how the data are distributed. Therefore, it will also be worth looking into this issue in the future in order to obtain the optimum bin size.

The choice of the galaxy redshift survey from which we take the data for this project will also be important, given that it will affect the reliability of our output. For example, the 2dF data has large fluctuations in its number counts plot, since its thin slices were strongly affected by the individual clusters and voids encountered. This scattering in the data may cause the numerical method to break down. Because, as mentioned before, we take first and second differences from our $\hat{R}(z)$ data for generating the values of its first and second derivatives, there is a risk in taking this approach. Small fluctuations in $\hat{R}$ will generate much exaggerated fluctuations in $d\hat{R}/dz$ and $d^2\hat{R}/dz^2$. With the generated fake testing data, we can reduce this problem significantly by minimising the numerical error while generating the testing data, however, we do not hold the same kind of control over the real data. Although higher order Runge-Kutta methods will have a natural smoothing effect, we cannot be sure till we try them how effective they will be in controlling such exaggerated fluctuations in $d\hat{R}/dz$ and $d^2\hat{R}/dz^2$. In result a lower accuracy may be obtained in our numerical output. Therefore, some other form of smoothing of the data may be needed before we run our programme with it, when one takes this problem into account, in the future.

Despite all the difficulties the above mentioned issues may cause, our initial attempt at the problem has successfully demonstrated the viability of the basic concept. Knowing the metric nearby will assist in analysing more distant observations in more than just a statistical sense, since the spacetime that the light rays we observe have travelled through, changes the size, brightness, frequency, position and shape of the images we measure. Therefore, as we probe deeper into space, the knowledge of the geometry of the universe around us will certainly play a crucial role in the data reduction of any survey in the future. With more reliable observational data, one may hope to achieve one of the long term objectives of the current project – being able to *prove* the homogeneity of the observable region of the universe rather than just assuming it in principle.

Appendix A

Choice of units

Throughout this thesis, we use geometric units where the gravitational constant G, and the speed of light c, are set to be one. If we choose a unit of time T_G seconds to be 1 geometric time unit, then the geometric length, mass and density units are, 1 $glu = L_G = cT_G\ meters$, 1 $gmu = M_G = \left(c^3/G\right) T_G\ kg$, and 1 $gmu\ glu^{-3} = \rho_G = (1/G)\, T_G^{-2}\ kg\ m^{-3}$ respectively. Since the purpose of this work is to be able to analyse the real observational data with the numerical method which is developed here, we need units suitable to cosmological scales. Therefore, we choose $100 kms^{-1}/Mpc$ to be one cosmological time unit. See the table below for the correspondence between Cosmological, SI and Astronomical Units.

Table A.1: Correspondence between Cosmological, SI and Astronomical Units

	Time	Length	Mass	Density
Cosmological	1 gtu	1 glu	1 gmu	1 $gmu\ glu^{-3}$
SI	$3.085 \times 10^{17}\ s$	$9.251 \times 10^{25}\ m$	$1.2457 \times 10^{53}\ kg$	$1.573 \times 10^{-25}\ kg/m^3$
Astronomical	9.77799 Gyr	2.998 Gpc	$6.2631 \times 10^{22}\ M_\odot$	$1.573 \times 10^{-28}\ g/cm^3$

In order to generate fake data for the FLRW models, we need values for q_0 and H_0. q_0 is dimensionless, and we choose H_0 to be $H_0 = 72 kms^{-1}/Mpc$, which is 0.72 in geometrical (cosmological) units. And with the generated functions, redshift z is dimensionless, both r and ϕ are coordinates of the LTB models and E is dimensionless since it is the energy per unit mass of the dust particles. However, M and t_B are not dimensionless, but can easily be converted back to SI or astronomical units using the table above.

Appendix B

Robertson-Walker observational relations

We here prove that if the observational data for $\hat{R}(z)$ and $4\pi\hat{m}n(z)$ has the standard RW form, the resulting LTB arbitrary functions M, E and t_B necessarily acquire RW forms.

As pointed out in [20, 54, 43], the RW forms of the expressions for the observer area distance and mass density of sources are

$$\hat{R}(z) = \frac{q_0 z + (1-q_0)\left(1-\sqrt{2q_0 z+1}\right)}{H_0 {q_0}^2 (1+z)^2} \ , \tag{B.1}$$

and

$$4\pi\hat{m}n(z) = \frac{3}{H_0 {q_0}^3} \frac{\left[q_0 z + (1-q_0)\left(1-\sqrt{2q_0 z+1}\right)\right]^2 (2q_0 z+1)^{-1/2}}{(1+z)^3} \tag{B.2}$$

respectively and equation (B.1) is also know as Mattig's formula. We can integrate equation (3.56) once and obtain

$$\frac{dz}{dr} = H_0 (1+z)^2 \sqrt{2q_0 z+1} \ . \tag{B.3}$$

If we integrate equation (B.3) once more, we then obtain an expression for $r(z)$. However, the $r(z)$ expression is different for three cases of q_0: $q_0 > 1/2$, $q_0 = 1/2$ and $0 < q_0 < 1/2$. Case I: $q_0 > \frac{1}{2}$ $(k = +1)$ – this model corresponds to a closed universe of finite volume.

$$r(z) = \frac{\sqrt{2q_0 z+1}}{(1+z)H_0(2q_0-1)} - \frac{1}{H_0(2q_0-1)} + \frac{2q_0\left[\tan^{-1}\left(\frac{\sqrt{2q_0 z+1}}{\sqrt{2q_0-1}}\right) - \tan^{-1}\left(\frac{1}{\sqrt{2q_0-1}}\right)\right]}{H_0(2q_0-1)^{3/2}} \tag{B.4}$$

Case II: $q_0 = \frac{1}{2}$ $(k = 0)$ – this is known as the *Einstein-deSitter* model.

$$r(z) = \frac{2}{3H_0}\left(1 - \frac{1}{(1+z)^{3/2}}\right) \tag{B.5}$$

Case III: $0 \leq q_0 < \frac{1}{2}$ $(k = -1)$ – this model corresponds to an open universe.

$$r(z) = \frac{1}{H_0(1-2q_0)}\left[1 - \frac{\sqrt{2q_0 z+1}}{1+z} + \frac{q_0}{\sqrt{1-2q_0}} \ln\left(\frac{\sqrt{2q_0 z+1}+\sqrt{1-2q_0}}{\sqrt{2q_0 z+1}-\sqrt{1-2q_0}}\right)\right.$$

$$+\frac{q_0}{\sqrt{1-2q_0}}\ln\left(\frac{1-\sqrt{1-2q_0}}{1+\sqrt{1+2q_0}}\right)\Bigg] \ . \tag{B.6}$$

Solving the first order linear differential equation (3.30) for $M(z)$, the result can be written as

$$\frac{d}{dz}\left[\frac{M(z)}{(1+z)\ d\hat{R}/dr}\right] = \frac{2\pi\hat{m}n}{(1+z)} + \frac{2\pi\hat{m}n}{(1+z)(d\hat{R}/dr)^2} \ . \tag{B.7}$$

Using equations (B.1) and (B.2) we find that

$$M(z) = {H_0}^2 q_0 \hat{R}^3 \,(1+z)^3 \ , \tag{B.8}$$

and therefore from (3.29) it follows that

$$2E(z) = (1-2q_0)\,{H_0}^2 \hat{R}^2\,(1+z)^2 \ . \tag{B.9}$$

From the two relations (B.8) and (B.9) one can see that the RW requirement $M \propto (2E)^{3/2}$ is satisfied. We need (B.4), (B.5) and (B.6) in addition to (3.35) and (3.32) in order to obtain an expression for τ in each case:

Case I:

$$\tau = \frac{q_0 \cos^{-1}\left(\frac{1-q_0+q_0 z}{q_0(1+z)}\right)}{H_0(2q_0-1)^{3/2}} - \frac{\sqrt{2q_0 z+1}}{H_0(1+z)(2q_0-1)} \ ; \tag{B.10}$$

Case II:

$$\tau = \frac{2}{3H_0}\ \frac{\sqrt{1+z}(z+4)-(3z+4)}{\left(z+1-\sqrt{1+z}\right)^3} \ ; \tag{B.11}$$

Case III:

$$\tau = \frac{1}{H_0(1-2q_0)}\left[\frac{\sqrt{2q_0 z+1}}{1+z} - \frac{q_0}{\sqrt{1-2q_0}}\ln\left(\frac{\sqrt{2q_0 z+1}+\sqrt{1-2q_0}}{\sqrt{2q_0 z+1}-\sqrt{1-2q_0}}\right)\right] \ . \tag{B.12}$$

Finally, we get t_B from $t_B = t_0 - r(z) - \tau$ for each case. Here t_0 is the age of the universe, and the expressions for t_0 in the closed, flat and open cases can be found in many books and papers, see for example [49, 59]:

Case I:

$$t_0 = \frac{1}{H_0}\left\{\frac{1}{1-2q_0} + \frac{q_0}{(2q_0-1)^{3/2}}\left[\frac{\pi}{2} + \sin^{-1}\left(\frac{q_0-1}{q_0}\right)\right]\right\} \tag{B.13}$$

or equivalently

$$t_0 = \frac{q_0}{H_0(2q_0-1)^{3/2}}\left[\cos^{-1}\left(\frac{1}{q_0}-1\right) - \frac{1}{q_0}\sqrt{2q_0-1}\right] \ ; \tag{B.14}$$

Case II:

$$t_0 = \frac{2}{3H_0} \ ; \tag{B.15}$$

Case III:

$$t_0 = \frac{1}{H_0}\left[\frac{1}{1-2q_0} - \frac{q_0}{(1-2q_0)^{3/2}}\ln\left(\frac{1-q_0}{q_0} + \frac{\sqrt{1-2q_0}}{q_0}\right)\right] \tag{B.16}$$

or equivalently

$$t_0 = \frac{1}{H_0}\left[\frac{1}{1-2q_0} - \frac{q_0}{(1-2q_0)^{3/2}}\cosh^{-1}\left(\frac{1}{q_0}-1\right)\right] \ . \tag{B.17}$$

Bibliography

[1] Adelman-McCarthy, J.K., et al., (SDSS team), *arXiv:* astro-ph/0507711.

[2] Andreon, S., Willis, J., Quintana, H., Valtchanov, I., Pierre, M., and Pacaud, F., *Mon. Not. Roy. Astr. Soc.* **353**, 353 (2004).

[3] Araújo, M.E., and Stoeger, W.R., *Phys. Rev.* **D 60**, 104020 (1999) [+ erratum: *Phys. Rev.* **D 64**, 049902 (2001)].

[4] Araújo, M.E., Arcuri, R.C., Bedran, M.L., de Freitas, L.R., and Stoeger, W.R., *Astrophys. J.* **549**, 716 (2001).

[5] Araújo, M.E., Roveda, S.R.M.M., and Stoeger, W.R., *Astrophys. J.* **560**, 7 (2001).

[6] Bondi, H., 1960, *Cosmology* (Cambridge University Press, Cambridge).

[7] Bondi, H., *Mon. Not. Roy. Astr. Soc.* **107**, 410 (1947); reprinted in *Gen. Rel. Grav.* **11**, 1783 (1999).

[8] Bonnor, W.B., *Mon. Not. Roy. Astr. Soc.* **167**, 55 (1974).

[9] Carlberg, R.G., Yee, H.K.C., Morris, S.L., Lin, H., Hall, P.B., Patton, D.R., Sawicki, M., and Shepherd, C.W., *Astrophys. J.* **563**, 736 (2001).

[10] Christlein, D., and Zabludoff, A.I., *Astrophys. J.* **621**, 201 (2005).

[11] Colless, M., *arXiv:* astro-ph/0305051.

[12] Colless, M., et al., (2dF team),*arXiv:* astro-ph/0306581.

[13] Croom, S.M., Smith, R.J., Boyle, B.J., Shanks, T., Miller, L., Outram, P.J., and Loaring, N.S., *Mon. Not. Roy. Astr. Soc.* **349**, 1397 (2004).

[14] Datt, B., *Zeitshrift fur Physik* **108**, 314 (1938); reprinted in *Gen. Rel. Grav.* **31**, 1619 (1999).

[15] Ehlers, WJ., Geren, P., and Sachs, R.K. *J. Math. Phys.* **9**, 1344 (1968).

[16] Ellis, G.F.R., In General Relativity and Cosmology, ed. Sachs, R.K., *Proc. Int. School Phys. "Enrico Fermi" XLVII.* (Academic press, New York), 104, 1971.

[17] Ellis, G.F.R., *Quart. J. R. Astron. Soc.* **16**, 245 (1975).

[18] Ellis, G.F.R., Nel, S.D., Maartens, R., Stoeger, W.R., and Whitman, A.P., *Phys. Reports* **124**, 315 (1985).

[19] Ellis, G.F.R., Perry, J.J., and Sievers, A.W., *Astrophys. J.* **89**, 1124 (1984).

[20] Ellis, G.F.R., and Stoeger, W.R., *Class. Quantum Grav.* **4**, 1697 (1987).

[21] Etherington, I.M.H., *Phil. Mag.* **15**, 761 (1933).

[22] Fasano, G., Poggianti, B.M., Couch, W.J., Bettoni, D., Kjærgaard, P., and Moles, M., *Astrophys. J.* **542**, 673 (2000).

[23] Goodman, J., *Phys. Rev.* **D 52**, 1821 (1995).

[24] Hellaby, C.W., *Class. Quantum Grav.* **4**, 635 (1987).

[25] Hellaby, C.W., *Phys. Rev.* **D 49**, 6484 (1994).

[26] Hellaby, C.W., *Astron. Astrophys.* **372**, 357 (2001).

[27] Hellaby, C.W., and Krasiński, A., *Phys. Rev.* **D 73**, 023518 (2006).

[28] Hellaby, C.W., and Lake, K., *Astrophys. J.* **282**, 1 (1984) [+ erratum: *Astrophys. J.* **294**, 702 (1985)].

[29] Hellaby, C.W., and Lake, K., *Astrophys. J.* **290**, 381 (1985) [+ erratum: *Astrophys. J.* **300**, 461 (1986)].

[30] Hopkins, A.M., *Astrophys. J.* **615**, 209 (2004).

[31] Jones, D.H., et al., (6dF team) *Mon. Not. Roy. Astr. Soc.* **355**, 747 (2004).

[32] Jones, D.H., Saunders, W., Read, M., and Colless, M., *Astron. Soc. of Australia* **22**, 277 (2005).

[33] Kantowski, R., and Sachs, R.K., *J. Math. Phys.* **7**, 443 (1966).

[34] Kolb, A., and Turner, M.S., 1990, *The Early Universe* (Addison-Wesley, New York).

[35] Krasiński, A., 1997, *Inhomogeneous Cosmological Models* (Cambridge University Press, Cambridge).

[36] Krasiński, A., and Hellaby, C.W., *Phys. Rev.* **D 69**, 043502 (2004).

[37] Kristian, J., and Sachs, R.K., *Astrophys. J.* **143**, 379 (1966).

[38] Lake, K., *Phys. Rev.* **D 29**, 771 (1984).

[39] Lemaître, G., *Ann. Soc. Sci. Bruxelles* **A53**, 51 (1933); reprinted in *Gen. Rel. Grav.* **29**, 641 (1997).

[40] Maarteens, R., Ellis, G.F.R., and Stoeger, W.R., *Quart. J. R. Astron. Soc.* **36**, 29 (1995).

[41] Maartens, R., and Martravers, D.R., *Class. Quantum Grav.* **11**, 2693 (1994).

[42] Maartens, R., Humphreys, N.P., Martravers, D.R., and Stoeger, W.R., *Class. Quantum Grav.* **13**, 253 (1996) [+ erratum: *Class. Quantum Grav.* **13**, 1689 (1996)].

[43] Mustapha, N., Hellaby, C.W., and Ellis, G.F.R., *Mon. Not. Roy. Astr. Soc.* **292**, 817 (1997): MHE.

[44] Mustapha, N., Bassett, B.A.C.C., Hellaby, C.W., and Ellis, G.F.R., *Class. Quantum Grav.* **15**, 2363 (1998).

[45] Omer, G.C., *Proc. Nat. Acad. Sci. U.S.A.* **53**, 1 (1965).

[46] Peacock, J.A., *arXiv:* astro-ph/0301042.

[47] Ribeiro, M.B., *Observatory* **122**, 201 (2002).

[48] Ribeiro, M.B., and Stoeger, W.R. *Astrophys. J.* **592**, 1 (2003).

[49] Sandage, A., *Astrophys. J.* **133**, 355 (1961).

[50] Sandage, A., *Ann. Rev. Astr. Astrophys.* **26**, 561 (1988).

[51] Shepherd, C.W., Carlberg, R.G., Yee, H.K.C., Morris, S.L., Lin, H., Sawicki, M., Hall, D.R., and P.B., Patton, *Astrophys. J.* **560**, 72 (2001).

[52] Stoeger, W.R., Maarteens, R., and Ellis, G.F.R., *Astrophys. J.* **443**, 1 (1995).

[53] Stoeger, W.R., Nel, S.D., Maarteens, R., and Ellis, G.F.R., *Class. Quantum Grav.* **9**, 493 (1992).

[54] Stoeger, W.R., Ellis, G.F.R., and Nel, S.D., *Class. Quantum Grav.* **9**, 509 (1992a).

[55] Stoeger, Nel, S.D., W.R., and Ellis, G.F.R., *Class. Quantum Grav.* **9**, 1711 (1992b).

[56] Stoeger, Nel, S.D., W.R., and Ellis, G.F.R., *Class. Quantum Grav.* **9**, 1725 (1992c).

[57] Tolman, R.C., *Proc. Nat. Acad. Sci. U.S.A.* **20**, 169 (1934); reprinted in *Gen. Rel. Grav.* **29**, 935 (1997).

[58] Totani, T., and Yoshii, Y. *Astrophys. J.* **540**, 81 (2000).

[59] Weinberg, S., 1972, *Gravitation and Cosmology* (Wiley, New York).

[60] "Canadian network for observational cosmology field galaxy survey", http://www.astro.utoronto.ca/ cnoc/cnoc2 .

[61] "Deep extragalactic evolutionary probe phase 2 redshift survey", http://deep.berkeley.edu/ marc/deep/ .

[62] "The European southern observatory very large telescope (ESO-VLT) [Visible imaging multi-object spectrograph VIRMOS] project", http://www.oamp.fr/virmos/ .

[63] "Two degree field", http://www.aao.gov.au/2df .

[64] "Sloan Digital Sky Survey", http://www.sdss.org .

[65] "Six degree field", http://www.aao.gov.au/local/www/6df/ .

[66] "Two Micron All Sky Survey", http://www.ipac.caltech.edu/2mass/ .